

Picowatt Resolution Calorimetry
for
Micro and Nanoscale Energy Transport Studies

by

Seid H. Sadat

A dissertation submitted in partial fulfillment
of the requirements for the degree of
Doctor of Philosophy
(Mechanical Engineering)
in the University of Michigan
2014

Doctoral Committee:

Associate Professor Pramod Sangi Reddy, Co-Chair
Professor Edgar Meyhofer, Co-Chair
Professor Massoud Kaviany
Professor Katsuo Kurabayashi
Professor Ctirad Uher

Dedication

To

Those who lost their lives in Iran's post-election protests in 2009 (1388)

&

Mohammad Nourizad who did not forget & taught me to keep my hopes up.

Acknowledgement

I spent some of the best years of my life in Ann Arbor. I had the opportunity to indulge myself into exploring, learning and thinking about different aspects of my life. I learnt a lot by immersing myself in the rich and attractive academic environment of the University; by being surrounded with smart and motivated people living in my research community; and by interacting with great people, in this small yet diverse town.

I would like to thank my advisor, Professor Pramod Reddy for providing me with scientific advice, academic freedom and career mentorship. I found him a deep thinker, a creative designer and a great experimentalist who can define important questions of the field. It was he who taught me to think about important questions of the field and not to be afraid of moving in directions that are orthogonal to the current research trends.

I would like to thank my co-adviser, Professor Edgar Meyhofer, for his availability to engage in enlightening discussions and teaching me how to systematically approach and solve complicated problems. He taught me to be patient and follow the journey of defining the problem and finding the solution step by step. He challenged me on my visit day by questioning my motives for pursuing a Ph.D. and years later I can see how he has had a significant role in transforming me to *acquire a taste* for science.

I would like to thank Lurie Nano-Fabrication (LNF) staffs who have worked hard to bring about such an exquisite working environment. Their responsible conduct of support and ever-improving management system enabled me to shorten the design to fabrication time and survive through long hours of working in clean room. Specifically, I would like to thank

Pilar, Sandrine, Ed, Lesile, Greg and Tom who were involved in my training and getting me up to speed.

I learned a lot by working and interacting with my colleagues in the lab. I would like to thank Aaron for our discussions on molecular charge transport; Terrence for his help in characterizing bimaterial cantilever devices; Won-Ho for collaborating on developing first generation of heater embedded electromigration devices; Bai and Yashar and Anthony for development of our novel platform and studying near-field heat transfer; and Dakotah for his helps with fabricating devices and characterizing devices.

I also would like to thank other faculty members of Department of Mechanical Engineering such as Professor Shorya Awtar and Professor Kevin Pipe, who I had the chance to interact with and learn from, during my time in Michigan.

I would like to thank my parents for their unconditional support and being the sole source of energy for all my endeavors; My Dad for his selflessness and humbleness; My Mom for her optimism and pride in me. I cannot express my happiness by words, to see my siblings, Behnam and Behnaz, being around and happy, building their future and I am proud to be part of it.

Finally, I am grateful of friendship with and support from my friends who I made in Ann Arbor, Mostfa, Niloufar, Behnam, Mohammad and Nasibeh as well as my friends from my hometown Ehsan, Faraz, Payam, Behzad and Mehrab for calling me once in a while and taking me out of the lab.

Table of Contents

DEDICATION...	ii
ACKNOWLEDGEMENT	iii
LIST OF FIGURES	viii
LIST OF TABLES.....	xv
ABSTRACT.....	xvi
CHAPTER 1: HIGH-RESOLUTION HEAT FLOW CALORIMETRY FOR CHARACTERIZING MICRO AND NANOSCALE TRANSPORT.....	1
1-1- Introduction	1
1-2- Calorimetry at micro and nanoscales	2
1-3- Principles of high-resolution calorimetry	6
1-4- Structure of this thesis	7
CHAPTER 2: ROOM TEMPERATURE PICOWATT-RESOLUTION CALORIMETRY	9
2-1- Abstract	9
2-2- Design of micro-calorimeter	9
2-3- Device fabrication process	11
2-4- Estimation of the device thermal conductance and thermal time constant	13
2-5- Estimation of temperature resolution of bimaterial cantilever thermometer	15
2-6- Characterizing the thermal conductance of the device	18
2-7- Experimental characterization of bimaterial thermometer performance	21
2-8- Characterizing optimum frequency of calorimetry measurement	23
2-9- Experimental determination of the resolution of the heat flow calorimeter	24
2-10- Conclusion	28

CHAPTER 3: HIGH RESOLUTION RESISTIVE THERMOMETRY FOR MICRO AND NANOSCALE MEASUREMENTS	29
3-1- Abstract	29
3-2- Introduction	30
3-3- Noise sources in resistance thermometry	31
3-4- Schemes to measure sinusoidally modulated and unmodulated temperature changes	36
3-5- Approach for experimental characterization of the noise equivalent temperature (NET) of temperature measurement schemes	44
3-6- Power spectral density of noise	51
3-7- Experimental verification of the NET for Schemes 3 and 4	59
3-8- Conclusion	63
 CHAPTER 4: RESISTANCE THERMOMETRY-BASED PICOWATT-RESOLUTION HEAT-FLOW CALORIMETER.....	 64
4-1- Abstract	64
4-2- Introduction	64
4-3- Design of micro-calorimeter	66
4-4- Device fabrication process	67
4-5- Estimation of the device thermal conductance and thermal time constant	67
4-6- Estimation of the heat current resolution	70
4-7- Experimental determination of the optimal heat current modulation frequency	70
4-8- Estimation of the noise of the thermometry scheme	74
4-9- Characterization of the optimum frequency of heat current modulation	76
4-10- Characterization of the thermal conductance of the device	77
4-11- Experimental determination of the resolution of the heat flow calorimeter	79

4-12- Comparison to bimaterial cantilever (BMC) based micro calorimeter	80
4-13- Conclusion	81
CHAPTER 5: HIGH RESOLUTION HEAT FLOW CALORIMETERS FOR STUDYING RADIATIVE ENERGY TRANSFER IN NEAR-FIELD REGIME.....	82
5-1- Abstract	82
5-2- Introduction	83
5-3- Fluctuational electrodynamics	86
5-4- Methodology	88
5-5- Experiments performed to understand the effect of film-thickness on NF- RHT	96
5-6- Theoretical modeling	98
5-7- Conclusion	105
CHAPTER 6: SUMMARY AND OUTLOOK	106
6-1- Summary	106
6-2- Possible future directions	107
APPENDIX.....	109
REFERENCES.....	111

LIST of Figures

- Figure 1-1- Calorimetry has a central role in gaining insight into a wide range of phenomena across various disciplines including physics, chemistry, biology as well as technological applications 2
- Figure 1-2- Examples of high-resolution calorimeters used for micro and nano scale studies: (a) suspended micro calorimeters in two-island configuration with nanowatts resolution for studying charge and phonon transport in nanostructures; (b) micro-optomechanical sensors for photothermal measurement with 40 picowatt resolution. 4
- Figure 1-3- Overall trend in studying energy transport at nanoscale. Researcher have tried to understand how energy transport at nanoscale is different from bulk by studying heat phonon transport in samples with dimensions smaller than the mean free path of energy carriers and with reduced dimensionalities. 5
- Figure 1-4- Working principle of devices for quantifying charge and heat currents. (a) The electrical current-to-be-measured is passed through a known electrical resistance and the developed potential difference is used to quantify the electrical current using Ohm's law; (b) The heat current-to-be-measured is channelized through a known thermal conductance and the developed temperature difference is used to measure heat current using Fourier's law. 7
- Figure 2-1- Schematic diagram of picowatt calorimeter. The thermal deflection response of the bimaterial cantilever is calibrated via a 4-probe heater/thermometer, which is integrated into the suspended region of the device. (b) Scanning electron micrograph of the microfabricated calorimeter. Active area of the device is a $40 \times 40 \mu\text{m}^2$ region suspended by thin ($2 \mu\text{m}$) and long ($40 \mu\text{m}$) beams. The suspended region is 500 nm thick SiN_x into which a $200 \mu\text{m}$ long and $0.5 \mu\text{m}$ thick bimaterial temperature sensor with a 125 nm thick Au layer is integrated. The 4-probe heater/thermometer integrated into the suspended region is $0.6 \mu\text{m}$ wide and 30 nm thick and is used for heating as well as the calibration of the bimaterial thermometer. 10
- Figure 2-2- (a) The schematic of the device used for the FEM simulation. All boundaries except the top surface were held at 300K , whereas an insulating boundary condition is used for the top surface (b) FEM results verify that the thermal gradients within the suspended region of the device are negligible. 13
- Figure 2-3- (a) 1st mode of cantilever deflection with a resonant frequency of about 6.2 KHz . (b) 2nd mode of cantilever deflection at a resonant frequency of $\sim 44 \text{ KHz}$. 16

- Figure 2-4- (a) Measured power spectral density displays peaks at 4.78 KHz and ~ 36.1 KHz corresponding to the first and second modes of the device (b) A point load of ~ 1 nN is applied to the end of the beam resulting in a tip displacement of about 50 nm, corresponding to spring constant of around 0.02 N/m. 17
- Figure 2-5- Results for the experimental measurement of TCR 18
- Figure 2-6- The thermal response of the microdevice as a function of the frequency ($2f$) of the input sinusoidal heat current. 19
- Figure 2-7- The measured amplitude of temperature oscillations of the suspended region (x -axis) for known inputs of heat currents (y -axis) at 2 Hz is shown, the slope of the curve gives the thermal conductance (~ 615 nW/K). 20
- Figure 2-8- Schematic of optical detection scheme: A laser is focused by a lens and is reflected off the bimaterial cantilever, and finally detected by a position-sensitive photodiode. 21
- Figure 2-9- Circuit diagram outlining how voltage signal is produced from two anti-phase photocurrent signals arising from the oscillating cantilever deflection. 22
- Figure 2-10- The response of the bimaterial cantilever thermometer is calibrated by inputting heat currents of known amplitudes at 2 Hz ($2f$) while simultaneously recording the bimaterial cantilever oscillations ($(\Delta V_{Def}, 2f)$) and the temperature oscillations of the suspended region 23
- Figure 2-11- (a) The power spectral density (PSD) of the noise in the bimaterial cantilever deflections (b) Signal to Noise Ratio at Different Frequencies. The optimum signal to noise ratio was found to occur around 2 Hz; this frequency was used for all the further measurements. For more details, see the main manuscript. 24
- Figure 2-12- The measured temperature oscillations ($\Delta T_{BMC}, 2f$ determined using the bimaterial cantilever) for various inputs of sinusoidal heat currents (0–44 pW, increased in steps of 2 pW) at 2 Hz. The noise floor of the device (~ 6.4 μ K) corresponds to <4 pW heat inputs. In the inset the response of the device to heat inputs of up to 100 nW is shown, demonstrating a dynamic range exceeding three orders of magnitude. 25
- Figure 2-13- (a) Depicts a microdevice that is simultaneously excited by a sinusoidal force (FS) and a random force (FR). (b) A simplified model that captures the effect of the two forces on the bimaterial cantilever. 27
- Figure 3-1- Principle of heat flow calorimetry. The sensing stage is isolated from the thermal reservoir by a finite thermal conductance (G_{th}). The magnitude of the heat output/heat current is quantified by measuring the temperature difference ΔT . 30
- Figure 3-2- Principle of resistive thermometry. (a) The electrical resistance is monitored by passing a known current and measuring the voltage drop across the resistor. The temperature of the object of interest is obtained by calibrating the relationship between resistance and temperature. (b) Differential measurement scheme for

isolating the signal of interest by rejecting the common mode voltage and the common mode noise arising from the noise in the electrical current ($I_{s,NI}$). The effect of drift in the environmental temperature is also attenuated by the differential scheme. 32

Figure 3-3- Microdevice used in this work. (a) Schematic diagram of the test device (not drawn to scale). A micro-heater line (Au heater) patterned on a glass substrate is used to generate temperature modulations. The top PRT is patterned on top of a micro-heater line and separated by a thin Al_2O_3 layer (see cross section) to electrically isolate it from the heater while maintaining it in excellent thermal contact with the heater. Note that the Al_2O_3 layer is not shown in the schematic in order to facilitate a clear view of the heater line. (b) Optical image of the microfabricated test device. 44

Figure 3-4- Characterization of the temperature dependence of resistance. a) The measured resistance vs. temperature for the PRT and heater lines: red arrow points to the resistance of the PRT whereas the blue arrow points to the resistance of the heater. (b) The obtained TCR values for the 35 nm thick PRT (Pt film) and 100 nm thick heater (Au film) line. 46

Figure 3-5- Characterization of the relationship between the RMS value of temperature oscillations and the amplitude of the heating current. (a) Schematic diagram of the measurement configuration used to measure the RMS values of temperature oscillations of the heater line. A potentiometer is placed in series to implement a differential scheme that enables the isolation of the $3f_H$ component of the voltage signal. (b) Measured RMS values of the temperature oscillation of the bottom heater line as a function of the amplitude of the heating electrical current. The frequency of the heating current is chosen to be 20 Hz. Inset shows the same data plotted as a function of square of the amplitude of the heating current, the relationship is linear as expected (the R-square measure of goodness of fit is 0.999). 47

Figure 3-6- Schematic diagram of the instrumentation setup used to measure the amplitude of temperature oscillations of the PRT. A differential measurement scheme is used to reject the noise arising from the non-ideality of the current source and to eliminate the effects of thermal drift. Inset: schematic diagram of the custom-built current source. 48

Figure 3-7- Characterization of the thermal contact between the heater line and the PRT. The measured RMS values of the temperature oscillations of the heater and the PRT, due to a sinusoidal thermal excitation of the heater line. The RMS values increase linearly with the magnitude of the square of the amplitude of the heating current. Further, the bottom and top line temperatures are identical. This provides strong support for the conclusion that the heater and PRT are in excellent thermal contact. The measurements were performed over a range of heating frequencies ($2f_H = 0.5$ Hz, 2 Hz, and 20 Hz). 49

Figure 3-8- Schematic diagram of the measurement setup to obtain the power spectral densities $PSD_{amp, total, RTI}$ and $PSD_{\Delta T, drift}$. These PSDs are required to estimate the NET of the each of the four schemes described in this study. 51

Figure 3-9- Experimental determination of $PSD_{Amp\ total, RTI}$ and $PSD_{\Delta T, Drift}$. Panel (a) shows the measured power spectral densities (at 280 K) of $PSD_{with I_s=I_{DC}}$ and $PSD_{with I_s=0 Amp}$ relative to the inputs (i.e. measured power spectral density divided by $G_1^2 G_2^2$). The larger power spectral density of $PSD_{with I_s=I_{DC}}$, at high-frequencies, is attributed to shot noise as discussed in the text. The shot noise contribution is seen to be relatively independent of the frequency (b) $PSD_{\Delta T, Drift}$ for a range of frequencies (1 – 20 Hz), at two different temperatures (80 K, 280 K) was obtained by first measuring $PSD_{with I_s=I_{DC}}$ and $PSD_{with I_s=0 Amp}$ in the frequency range of interest and using Eq. 25 described in the text. (c) Measured $PSD_{Amp\ total, RTI}$ of thermometer at 80 K and 280 K in a range of frequencies (1-20 Hz), and (d) Measured $PSD_{Amp\ total, RTI}$ of thermometer at 80 K and 280 K in a larger range of frequencies (1 Hz - 3 kHz). The data presented in the figure was obtained by first averaging the measured PSD in 200 individual experiments (Fig. 9a, d) and 20 individual experiments (Fig. 9b, c) and subsequently performing further averaging using a 20 point median averaging scheme. 54

Figure 3-10- Measurement of amplifier noise and temperature drift at low frequencies. We determined the $PSD_{Amp\ total, RTI}$ (b) and $PSD_{\Delta T, Drift}$ (c) in the narrow frequency range of 0 to 1 Hz from the $PSD_{with I_s=I_{DC}}(f)$ and $PSD_{with I_s=0 Amp}(f)$ shown in (a) by averaging five individual curves and by curve fitting the averaged data. The data shown in panels (b) and (c) were obtained by using the data presented in panel (a). As a representative example, the inset of Fig. 10a shows the measured PSD at 0.5 Hz along with the curve fits and the corresponding 95% confidence intervals. 56

Figure 3-11- Experimental demonstration of the resolution of scheme 3. In this scheme modulated temperature changes are detected using an unmodulated sensing current. Part (a) shows the measured RMS values of the temperature oscillations of the PRT, at an ambient temperature of 280 K, when the heater line is excited using sinusoidal heating currents (0.5, 2.0, and 20 Hz). The dashed lines in the figure, represent the expected RMS temperature values based on data shown in Fig. 7. The error bars above reflect the standard deviation in the RMS value reported by the lock-in amplifier. The solid lines show the estimated noise floor for NET measurements performed at each of the frequencies, while the bands represent the uncertainty of the NET estimates. The inset presents the same data in a log-log plot. Figure (b) shows data otherwise identical to those in (a) for measurements performed at 80 K. 61

Figure 3-12- Experimental demonstration of the resolution of scheme 4 at low modulation frequencies (0.5 Hz). Modulated temperature changes were measured using a modulated sensing current at 500 Hz. All measurements were performed at 280K. The dashed line represents the expected temperature RMS values based on the data shown in Fig. 7. The dotted lines show curve fits to the measured data. The error bars above reflect the standard deviation in the RMS value reported by the lock-in amplifier. The solid lines and bands show the estimated NETs and the uncertainty in the estimated NETs respectively. 62

Figure 4-1- scanning electron microscope (SEM) images of the fabricated devices. (a) SEM image of microfabricated device which consists of the suspended device and a matching resistor. The central area of the device is suspended by eight $2\ \mu\text{m}$ wide, $500\ \text{nm}$ thick and $400\ \mu\text{m}$ long beams. (b) Magnified image of the suspended region. Two platinum (Pt) 4-probe thermometers are integrated into the suspended region. The first sensor consists of a long serpentine line (shown in green), which has a resistance of $\sim 9\ \text{k}\Omega$ between the voltage measuring probes (false-colored in blue) and serves as a Pt resistance thermometer (PRT). The second 4-probe (shown in red) has a resistance of $\sim 1.5\ \text{k}\Omega$ between the voltage measuring probes that are false-colored in blue and is used as a micro-heater to input known amounts of heat via Joule heating. The Pt lines of both the 4-probes are $\sim 800\ \text{nm}$ wide and $\sim 30\ \text{nm}$ thick. 66

Figure 4-2- Results of FEM analysis predicting temperature distribution on device. (a) All boundaries except the top surface were held at $300\ \text{K}$, whereas an insulating boundary condition is used for the top surface. Inset shows overall view of the simulated device. (b) Meshed model overlaid on computed temperature distribution from FEM analysis. The thermal gradients within the suspended region of the device are seen to be negligible. 69

Figure 4-3- Schematic of the suspended device. Out of the eight suspending beams, heat is generated only in four beams in which an electrical current is supplied. 72

Figure 4-4- Temperature response as a function of frequency of heat currents ($500\ \text{nW}$) of constant amplitude. The inset shows the power spectral density of the noise associated with temperature measurements. 73

Figure 4-5- Obtained power spectral densities of (a) temperature drift of the sensing PRT and (b) relative-to-input electrical noise. 76

Figure 4-6- Estimated signal to noise ratio computed from the data shown in Fig. 2a. The signal to noise ratio reaches a maximum when the heating current is modulated at $6.6\ \text{Hz}$. 77

Figure 4-7- The thermal conductance of the beams, G_{th} is determined from a linear regression between the effective power dissipation, P_{Eff} , at $2\ \text{Hz}$ and the resultant amplitude of the temperature oscillations. The coefficient of determination (R^2) for the linear regression model is found to be 0.9994 . 78

Figure 4-8- The measured amplitude of the temperature oscillations for heat currents of various amplitudes that are modulated at $f_{\text{h, Opt}} = 6.6\ \text{Hz}$. The experimentally measured noise floor ($20\ \mu\text{K}$) agrees well with calculated thermometry noise floor of $\sim 22\ \mu\text{K}$ (red dashed line). We note that the modulation frequency of $6.6\ \text{Hz}$ is beyond the thermal bandwidth of the device ($f_c \sim 4.3\ \text{Hz}$), therefore, the amplitude of temperature oscillations is attenuated (by a factor of 1.9 , see Fig. 2a). The dashed line (blue) accounts for this effect and predicts the amplitude of temperature oscillations from $\Delta T = (\text{amplitude of heat current}) / (1.9G_{\text{th}})$. The inset shows that the response of the device to heat inputs of up to $1\ \mu\text{W}$ is linear, demonstrating a dynamic range of more than $100\ \text{dB}$. 79

- Figure 5-1- Radiative energy transfer phenomena. (a) far-field energy transfer is dominated by propagating electromagnetic waves and independent of distance; (b) near-field energy transfer is dominated by evanescent waves and shows strong distance dependence. 83
- Figure 5-2- Three category of reported experimental studies on near-field radiative heat transfer, based on the geometry of the interacting surfaces. 85
- Figure 5-3- Gap-dependent heat transfer coefficient between different emitter-receiver material pairs in the plane-plane configuration, calculated using the fluctuational electrodynamics formalism. 87
- Figure 5-4- Experimental illustration of the experimental setup for studying NFRHT. The temperature of the silica sphere mounted on the heating calorimeter is modulated sinusoidally and the corresponding radiative power coupled to the high-resolution receiver calorimeter is measured by recording the resultant temperature fluctuations of the receiver. The surface of the receiver is coated with different thicknesses of thin film SiO₂. The whole setup is mounted on a 6 DOF nano-positioner inside vacuum chamber. 89
- Figure 5-5- Nano-positioning stage with 6 degrees of freedom with required mechanical and thermal stability for parallelizing, placing in sub-wavelength distances and maintaining the surfaces throughout the entire length of experiment. 92
- Figure 5-6- Two novel calorimeter devices developed for studying NFRHT in sphere-plane and plane-plane configurations. (a) Calorimeter device with rib structure on the active area and suspension beams; (b) Calorimeter devices based on Silicon On Insulator chips with ultimate stiffness required for studying various material structures. 93
- Figure 5-7- Fabrication process flow for calorimeter devices with rib structure. (a) starting with 500 μm silicon wafer 0.8 μm trenches with 10 μm depth are etched using RIE tool; (b) trench width is further reduced by thermal oxidizing of Si to grow 0.5 μm Oxide; (c) trenches are capped by depositing 0.6 μm low-stress nitride using LP-CVD furnace; (d) target active layer deposition-2 μm of low temperature oxide; (e) thermal evaporations of 100 nm Au film as the cap layer; (f) Au cap layer and oxide etch using plasma etch to form active area; (g) heater/thermometer and electrical connection patterns using lift-off process; (h) front and backside patterning of nitride film to form device contour; (i) wet release of the device using KOH etch; (j) removal of support oxide using BHF etch. 94
- Figure 5-8- Fabrication process flow for calorimeter devices based on Silicon On Insulator (SOI) devices. (a) starting with 500 μm thick SOI wafer with 1 μm thick Buried Oxide (BOX) layer and 10 μm device layer; (b) 500 nm thick insulating nitride layer deposition as using LP-CVD tool; (c) target active layer deposition-2 μm of low temperature oxide; (d) thermal evaporations of 100 nm Au film as the cap layer; (e) Au cap layer and oxide etch using plasma etch to form active area; (f) heater/thermometer and electrical connection patterns using lift-off process; (g) front and backside patterning of nitride film to form device contour; (h) through-

wafer etch using RIE tool and stopping on BOX layer; (i) removal of BOX using BHF etch; (j) removing cap layer using Au etchant. 95

Figure 5-9- Optical images of the heating calorimeter with a 53 μm micro-sphere mounted on it. (a) image focused on the device surface; (b) image focused on the micro-sphere. 96

Figure 5-10- Measured near-field contribution to the radiative thermal conductance. The effect of far-field radiation and change in view factor has been subtracted out from the measured data. It can be seen that the thickness of the films dramatically influence the gap-size at which NF-RHT effects become appreciable. 97

Figure 5-11- Results of the near-field heat transfer modeling within the framework of fluctuational electrodynamics and using scattering matrix formalism between SiO_2 sphere and Au surfaces coated with SiO_2 film with different thicknesses. (a) Heat transfer between semi-infinite SiO_2 surface and semi-infinite Au surface coated with SiO_2 film. (b) Transfer conductance between SiO_2 sphere and semi-infinite Au surface coated with SiO_2 film calculated using Derjagun approximation. 100

Figure 5-12- (a) Frequency dependent dielectric constant of SiO_2 film. (b) Computed spectral composition of the NF-RHT between bulk SiO_2 surface and bulk Au surface coated 2 μm and 100 nm SiO_2 films separated by 10 nm. 102

Figure 5-13- Magnitude of the transmission function (T_{\parallel}) as a function of the product of k_{\parallel} and d for absorbing films with two different thicknesses of 2 μm and 100 nm at different gap sizes computed at SPP frequency. 103

Figure 5-14- Magnitude square of electric field ($|E|^2$) at the excitation frequency of SPP for two different coating thicknesses and gap sizes of 10, 20, 50 and 100 nm. The Au layer is placed on the right side and results illustrate the gap-dependence of the penetration depth of SPPs. 104

List of Tables

- Table 2-1- Fabrication process of the picowatt resolution calorimeter based on bimaterial cantilever thermometer 12
- Table 3-1- Different schemes for resistance thermometry. The temperature is either modulated at a frequency (f_T) or is not modulated. Similarly, the electrical current for sensing resistance changes is either modulated at a frequency (f_s) or is not modulated. 36
- Table 3-2- The estimated resolution of the four different schemes of resistance thermometry. The resistance of the PRT is assumed to be 10 k Ω while the bandwidth of measurement is set to 16 mHz. 58
- Table 4-1- Fabrication process of the picowatt resolution calorimeter based on resistive thermometer 68
- Table 5-1- Performance specifications of calorimeter devices developed for studying NFRHT. 93

ABSTRACT

PICOWATT RESOLUTION CALORIMETRY FOR MICRO AND NANOSCALE ENERGY TRANSPORT STUDIES

by

Seid H. Sadat

Co-Chairs: Pramod Sangi Reddy
Edgar Meyhofer

Precise quantification of energy transport is key to obtaining insights into a wide range of phenomena across various disciplines including physics, chemistry, biology and engineering. This thesis describes technical advancements into heat-flow calorimetry which enable measurement of energy transport at micro and nanoscales with picowatt resolution. I have developed two types of microfabricated calorimeter devices and demonstrated single digit picowatt resolution at room temperature. Both devices incorporate two distinct features; an active area isolated by a thermal conductance (G_{Th}) of less than $1 \mu\text{W/K}$ and a high resolution thermometer with temperature resolution (ΔT_{res}) in the micro kelvin regime. These features enable measurements of heat currents (q) with picowatt resolution ($q = G_{Th} \times \Delta T_{res}$).

In the first device the active area is suspended via silicon nitride beams with excellent thermal isolation ($\sim 600 \text{ nW/K}$) and a bimaterial cantilever (BMC) thermometer with temperature resolution of $\sim 6 \mu\text{K}$. Taken together this design enabled calorimetric measurements with 4 pW resolution.

In the second device, the BMC thermometry technique is replaced by a high-resolution resistance thermometry scheme. A detailed noise analysis of resistance thermometers,

confirmed by experimental data, enabled me to correctly predict the resolution of different measurement schemes and propose techniques to achieve an order of magnitude improvement in the resolution of resistive thermometers. By incorporating resistance thermometers with temperature resolution of $\sim 30 \mu\text{K}$, combined with a thermal isolation of $\sim 150 \text{ nW/K}$, I demonstrated an all-electrical calorimeter device with a resolution of $\sim 5 \text{ pW}$.

Finally, I used these calorimeters to study Near-Field Radiative Heat Transfer (NF-RHT). Using these devices, we studied—for the first time—the effect of film thickness on the NF-RHT between two dielectric surfaces. We showed that even a very thin film ($\sim 50 \text{ nm}$) of silicon dioxide deposited on a gold surface dramatically enhances NF-RHT between the coated surface and a second silica surface. Specifically, we find that the resulting heat fluxes are very similar to those between two bulk silicon dioxide surfaces when the gap size is reduced to be comparable to that of the film thickness. This interesting effect is understood on the basis of detailed computational analysis, which shows that the NF-RHT in gaps comparable to film thickness is completely dominated by the contributions from surface phonon-polaritons whose effective skin depth is comparable to the film thickness. These results are expected to hold true for various dielectric surfaces where heat transport is dominated by surface phonon-polaritons and have important implications for near-field based thermo photovoltaic devices and for near-field based thermal management.

CHAPTER 1

High-Resolution Heat Flow Calorimetry for Characterizing Micro and Nanoscale Transport

1-1- Introduction

Calorimetry is a broad term referring to techniques for quantifying heat outputs and heat currents. Historically, quantification of heat generation and energy transport has been critical for obtaining insights into a wide range of phenomena across various disciplines including engineering, biology, physics and chemistry (Figure 1-1). Calorimetry has a central role in gaining insight into the specific heat capacity and thermal conductivity of matter and their temperature dependence. In chemistry, calorimeters are widely used to study the heat of reactions and phase transitions. Biologists have used calorimeters to study biochemical reactions to understand factors affecting enzymatic activities or to measure heat generation of biological samples such as living animals or large ensembles of cellular systems [1]. In fact one of the first applications of calorimeters goes back to 1780 when Lavoisier and Laplace studied heat generation of a living guinea pig using an ice calorimeter [2]. Furthermore, calorimeters have found applications in technological devices such as in IR and millimeter wave detectors [3] used in deep space explorations [4] and have significant potential for use in night vision cameras [5].

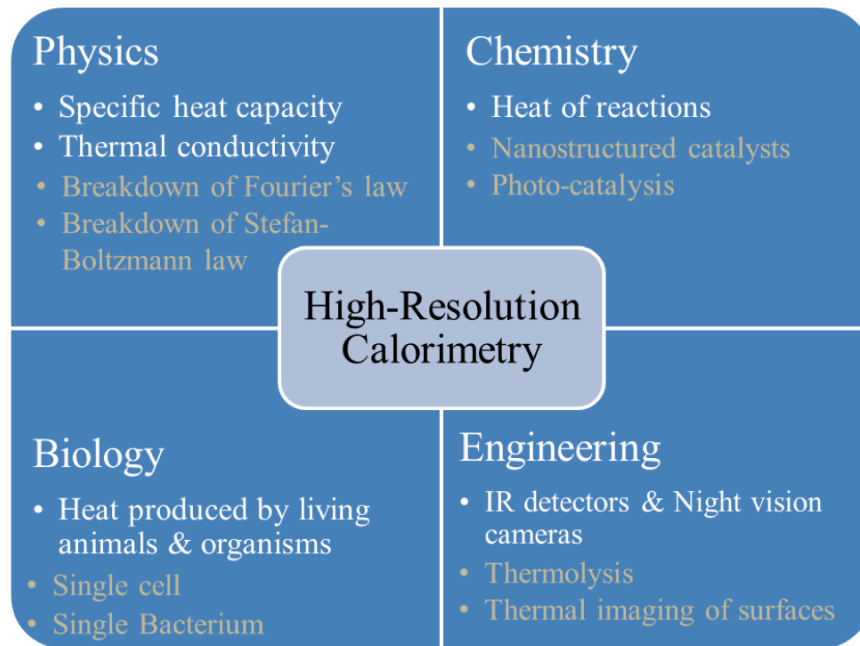


Figure 1-1- Calorimetry has a central role in gaining insight into a wide range of phenomena across various disciplines including physics, chemistry, biology as well as technological applications

1-2- Calorimetry at micro and nanoscales

The advent of nanotechnology has heralded exciting opportunities and great potential for developing novel technologies for renewable sources of energy. However, realization of this potential requires precise and predictable manipulation of matter as well as accurate quantification of energy transfer at micro, nano and atomic scales. It is clear that one of the principal hurdles to achieve these ground-breaking scientific goals and revolutionary applications is the lack of necessary instruments and measurement techniques. For example, probing energy transport at nanoscale distances or samples with reduced dimensionalities requires heat flow calorimeter devices with unprecedented resolutions. Therefore, development of high-resolution calorimetry techniques that are suitable for studying energy transport at micro and nanoscale is an essential step toward fully realizing the potential of nanotechnology [6].

Development of calorimeter devices suitable to studying energy transport at nanoscale is challenging due to the fact that the small physical sizes and the miniscule signals that need to be recorded from micro/nanoscale systems require unprecedented precision and resolution. A number of recent studies have aimed to develop calorimeters for studying heat of reactions on sample volumes of nano-liters with nanowatt resolution [7]. Further, these high-resolution calorimeters can be used to systematically study performance of nanostructured catalysts and photocatalysts [8]. In biology, there are a variety of interesting and important problems that can be addressed if one can study the metabolic activity of single cells or single bacterium, which are predicted to be in the range of 5 to 50 pW [1, 9, 10]. Further, in terms of technological goals there is significant interest in novel thermo-plasmonic nanostructures as nano-scale sources of heat, which if carefully studied and optimized, could be used for targeted destruction of tumors and cancerous tissues [11, 12].

Further, studying energy transport at the nanometer scale where Fourier's law of heat conduction or Stefan-Boltzmann law of radiative heat transfer are inadequate to describe thermal transport, requires calorimeter devices with unprecedented resolution. For instance, high-resolution calorimetric measurements have been successfully used to experimentally demonstrate quantization of thermal conductance at cryogenic temperatures [13]. High-resolution calorimeter devices were also employed to study thermal conductivity of polymeric nanofibers where it has been shown that by just changing the drawing ratio of polymeric nanofibers, it is possible to enhance thermal conductivity of the material by three orders of magnitude [14]. Such polymeric fibers have significant potential for developing low thermal resistance interface materials.

If we look more closely into the field of nanoscale energy transport which has experienced rapid growth in the past two decades, there are a number of important questions that the scientific community is seeking to answer such as: How heat and energy transport at

nanoscale is different with respect to its bulk counterpart? How the phenomena of heat transport in low-dimensional materials, where at least one of the characteristic length scales of the system is comparable to or smaller than the mean free path of the energy carriers (phonons/electrons) should be analyzed [14-16]? Understanding these phenomena paves the way for developing novel thermal management and energy conversion devices.

To address the need for metrology tools that are required for quantitative study of energy transport at the nanoscale, different groups have worked to develop high-resolution heat flow calorimeter devices such as suspended microdevice structures that have enabled heat flow measurements with ~ 1 nanowatt (nW) power resolution at room temperature [15] (Fig. 1-2a) or bimaterial cantilever-based calorimeter devices with a predicted resolution of ~ 40 picowatt (Fig. 1-2b) [17]. These devices have been used recently to gain insights into the analysis of nanoscale photon [14] and phonon [18] transport mechanisms [19, 20].

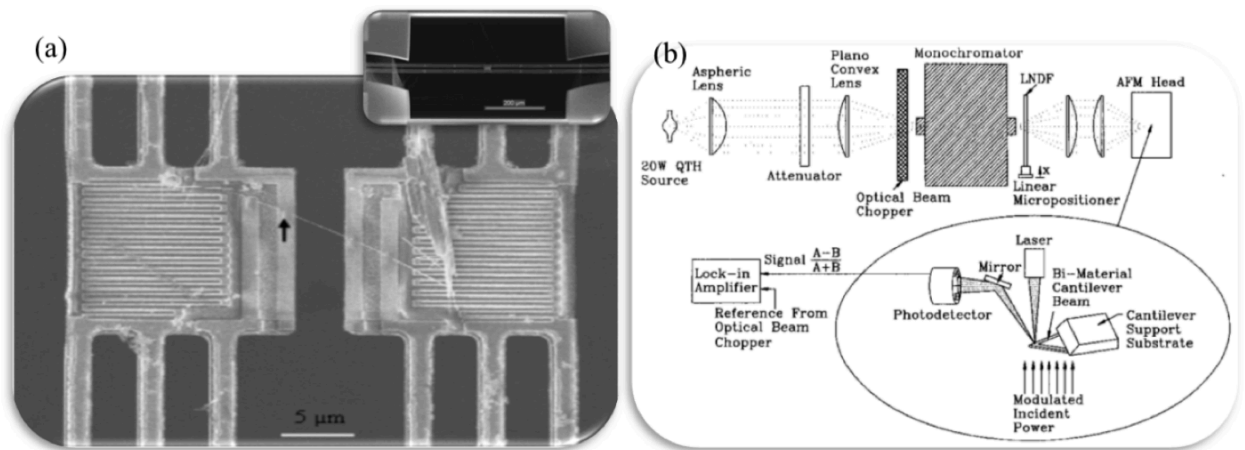


Figure 1-2- Examples of high-resolution calorimeters used for micro and nano scale studies: (a) suspended micro calorimeters in two-island configuration with nanowatts resolution for studying charge and phonon transport in nanostructures; (b) micro-optomechanical sensors for photothermal measurement with 40 picowatt resolution.

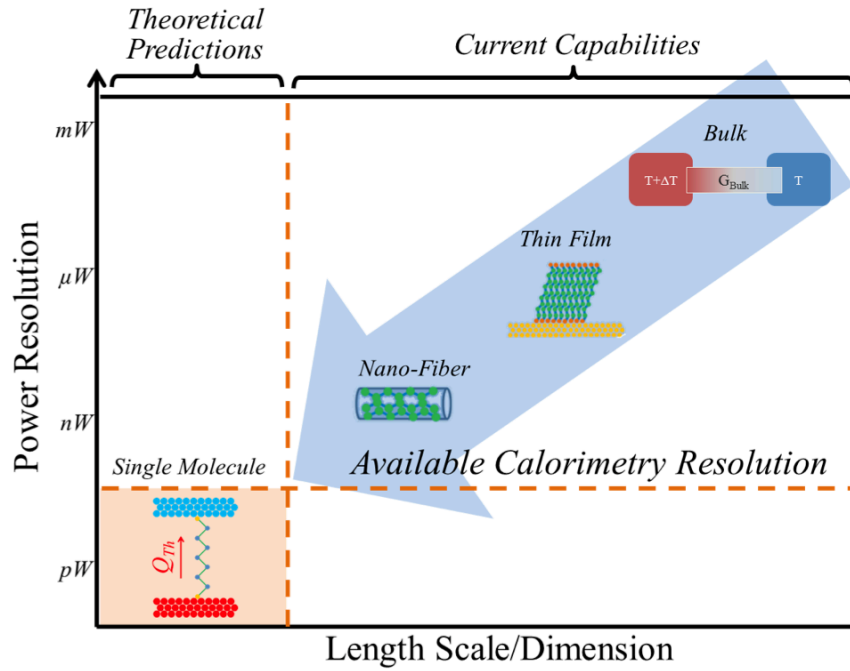


Figure 1-3- Overall trend in studying energy transport at nanoscale. Researcher have tried to understand how energy transport at nanoscale is different from bulk by studying heat phonon transport in samples with dimensions smaller than the mean free path of energy carriers and with reduced dimensionalities.

In spite of these important steps, several nanoscale thermal transport phenomena have not been addressed yet. These include questions such as the effect of surface chemistry/structure on the near field radiative transport properties, heat transport properties of atomic scale point contacts and molecular junctions, mechanisms of energy transport in organic monolayers/interfaces and its relations to the structure and interaction of molecules. On the other hand, from a scientific point of view, there are some very interesting predictions such as breakdown of Fourier's law and length dependence of thermal conductivity in one or two-dimensional material systems [21], such as grapheme and single polymer chains, which have not been studied yet. Based on these theoretical studies, novel thermal and phononic devices are proposed in literature [22]. However, due to a lack of calorimetric tools that are capable of resolving energy flows in picowatt range, none of these theoretical predictions have been experimentally studied so far.

Elucidation of many of these nanoscale heat transport phenomena requires measurement techniques with single-digit picowatt-resolution. In this thesis, I will describe the steps that I took to develop high-resolution calorimeter devices with picowatt resolution, in order to both study novel transport phenomena at nanoscale as well as leverage calorimetric techniques in other applications at micro and nano scales.

1-3- Principles of high-resolution calorimetry

A calorimeter device, which measures heat flows, is analogous to an ammeter device, which measures electrical currents (Fig. 1-4). The general strategy for measuring an electric current is to pass the current to-be-measured through a known electric resistance (G_e), measure the potential difference developed across the resistor (ΔV) and calculate the current using Ohm's law ($I_e = G_e \times \Delta V$). It is clear that in order to increase the resolution of current measurement process one needs to choose a large resistance and employ a high-resolution voltmeter. Similarly, to quantify an unknown heat current, we channel it through a material with a known thermal resistance (G_{Th}), measure the temperature difference developed across it (ΔT) and use Fourier's law ($Q_{Th} = G_{Th} \times \Delta T$) to calculate the magnitude of the heat current (Fig. 1-4b). In order to quantify smaller heat currents, we need to employ a large thermal resistance and a high-resolution thermometer for measuring small temperature changes. This analysis shows that one way of achieving picowatt resolution heat flow calorimetry is to design a system with a conductance of $\sim 1 \mu\text{W/K}$ and employ a thermometer which is capable of resolving temperature changes as small as $1 \mu\text{K}$.

The realization of such calorimeter designs is conceptually simple and features two important components: A suspended region that is connected to a thermal reservoir via an excellent thermal isolation scheme and a high-resolution thermometer.

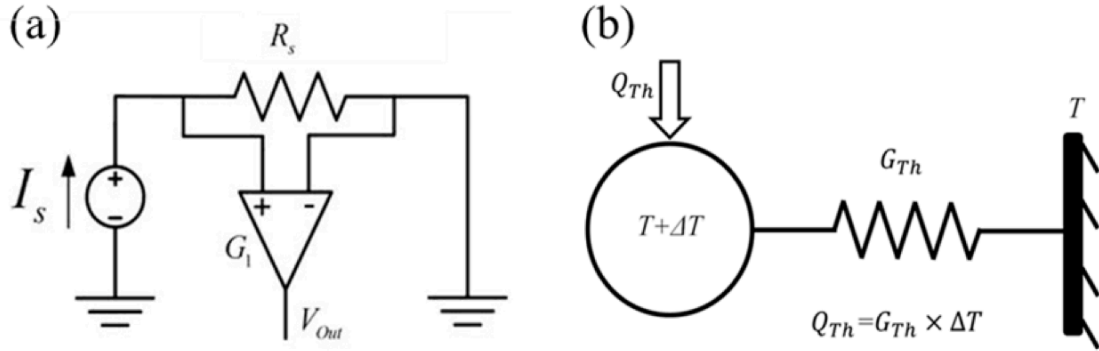


Figure 1-4- Working principle of devices for quantifying charge and heat currents. (a)The electrical current-to-be-measured is passed through a known electrical resistance and the developed potential difference is used to quantify the electrical current using Ohm’s law; (b) The heat current-to-be-measured is channelized through a known thermal conductance and the developed temperature difference is used to measure heat current using Fourier’s law.

The isolation scheme is usually realized through suspending the active area of the device by low thermal conductance suspension beams and operating the device in a vacuum environment to suppress the heat conduction through air molecules. The heat flow (Q_{Th}) through the suspended region is obtained from prior calibration of the thermal conductance (G_{Th}) between the suspended region and the surrounding substrate, and by measuring the temperature rise (ΔT) of the suspended region: $Q_{Th} = G_{Th} \times \Delta T$.

1-4- Structure of this thesis

In this thesis, I describe two types of calorimeters that I have developed, which allow single digit picowatt calorimetry at room temperature for the first time. This represents at least an order of magnitude improvement over what was previously reported. Chapter two, describes my efforts to develop high-resolution heat flow calorimeters based on bimaterial cantilever thermometers and technical requirements for performing picowatt resolution calorimetric measurements. Chapter three describes a detailed noise analysis for different resistive thermometry schemes alongside with my experimental study of noise components of a resistive thermometer. This study enabled me to correctly predict the resolution of different

resistive thermometry schemes and propose techniques to achieve an order of magnitude improvement in the resolution of resistance thermometers. Chapter four describes an all-electrical heat flow calorimeter device based on resistance thermometry, which requires significantly simpler instrumentation and is capable of resolving heat flows in the picowatt range. Finally, chapter five describes how I leveraged these technical advancements to study near-field radiative heat transport and gained technologically relevant insights into this phenomenon. In chapter six, I discuss potential future research directions that could lead to important technological and scientific advancements.

CHAPTER 2

Room Temperature Picowatt-Resolution Calorimetry

2-1- Abstract

Picowatt-resolution calorimetry is necessary for fundamental studies of nanoscale energy transport. In this chapter, I describe a microfabricated calorimeter device capable of performing calorimetric measurements with a resolution of <4 pW—an order of magnitude improvement over the state-of-the-art room temperature calorimeters [17]. This is achieved by the incorporation of two important features. First, the active area of the device is thermally isolated by thin and long beams with a total thermal conductance (G_{Th}) of ~ 600 nW/K. Further, a bimaterial cantilever thermometer capable of a temperature resolution (ΔT_{res}) of ~ 4 μ K is integrated into the microdevice. The small thermal conductance and excellent temperature resolution enable measurements of heat currents ($q = G_{Th} \times \Delta T_{res}$) with a resolution of <4 pW.

2-2- Design of micro-calorimeter

The basic strategy employed in this work for achieving picowatt-resolution calorimetry is to microfabricate a thermally isolated device from which very precise temperature measurements can be made.

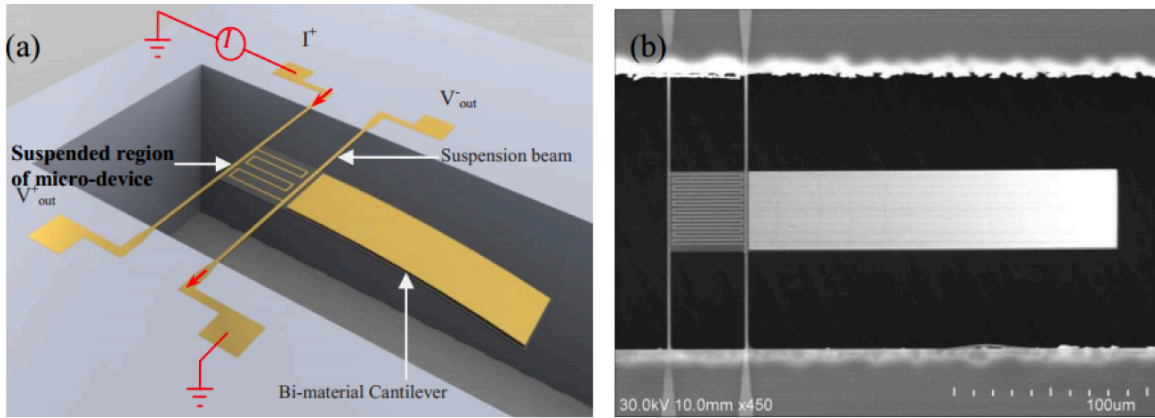


Figure 2-1- Schematic diagram of picowatt calorimeter. The thermal deflection response of the bimaterial cantilever is calibrated via a 4-probe heater/thermometer, which is integrated into the suspended region of the device. (b) Scanning electron micrograph of the microfabricated calorimeter. Active area of the device is a $40 \times 40 \mu\text{m}^2$ region suspended by thin ($2 \mu\text{m}$) and long ($40 \mu\text{m}$) beams. The suspended region is 500 nm thick SiN_x into which a $200 \mu\text{m}$ long and $0.5 \mu\text{m}$ thick bimaterial temperature sensor with a 125 nm thick Au layer is integrated. The 4-probe heater/thermometer integrated into the suspended region is $0.6 \mu\text{m}$ wide and 30 nm thick and is used for heating as well as the calibration of the bimaterial thermometer.

The calorimeter (Figure 2-1) consists of a thin low stress silicon nitride (SiN_x) membrane that is suspended by thin and long SiN_x beams which have a combined thermal conductance (G_{Th}) of $\sim 600 \text{ nW/K}$ and serve to thermally isolate the suspended membrane. Further, a bimaterial cantilever (BMC) that can detect periodic temperature changes with a resolution (ΔT_{res}) of $\sim 4 \mu\text{K}$ and a noise floor of $\sim 6.4 \text{ K}$ is integrated into the suspended membrane. When this suspended device is operated in a high vacuum environment ($< 10^{-6}$ Torr), thermal conduction via the gas molecules and heat transport by radiation are negligible, ensuring that the total thermal conductance between the suspended region and the environment is $\sim 600 \text{ nW/K}$. The low thermal conductance of the beams and the excellent temperature resolution of the bimaterial cantilever enable single-digit picowatt resolution. A schematic of the picowatt calorimeter along with a scanning electron micrograph of a fabricated device is shown in Figure 2-1.





The active region of the device is a SiN_x membrane with a thickness of ~0.5 μm. The membrane is suspended by four SiN_x beams, each of which is 50 μm long, 2 μm wide and 0.5 μm thick. A serpentine gold (Au) line, which is 600 nm wide and 30 nm thick, is integrated into the membrane and serves as both a heater and a thermometer. Further, a bimaterial cantilever made from SiN_x and Au having a length of ~200 μm and a width of ~40 μm is also incorporated into the suspended region. Following previous studies, where bimaterial cantilever sensor sensitivity was optimized [23], we chose the thickness of Au and SiN_x layers to be ~125 and ~500 nm, respectively.

2-3- Device fabrication process

The device fabrication process starts with successive wet thermal oxidation and low pressure chemical vapor deposition (LP-CVD) of SiN_x to deposit ~1 μm and ~500 nm thick films of silicon dioxide and silicon nitride on both sides of a p-type silicon wafer (step 1, Table 2-1). The 0.6 μm-wide 4-probe heater/thermometer line, the smallest feature of the device, is made by a combination of high precision lithography and evaporation of Cr/Au (3/30 nm) on a 1.5 μm-thick patterned photoresist (SPR-220-3) in a lift-off technique (step 2, Table 2-1). Next, the metal layer for the bimaterial cantilever sensor and contact pads (Cr/Au: 3/125 nm) is created using lift-off on the front side of the wafer (step 3, Table 2-1). Subsequently, the low-stress nitride layer is lithographically patterned by plasma etch using a 3 μm thick photoresist (SPR-220-3) as the soft mask to create the device contour (step 4, Table 2-1). Next, the backside pattern is transferred by plasma etching of nitride and oxide on the backside using a 10 μm thick photoresist (AZ-9260) as the soft mask (step 5, Table 2-1). The back-side opening is made via a through wafer etch using deep reactive ion etching (DRIE) (step 6, Table 2-1). Finally, the suspended devices are released by HF etching of the sacrificial oxide layer (step 7, Table 2-1).

Table 2-1- Fabrication process of the picowatt resolution calorimeter based on bimaterial cantilever thermometer

	Process	Detail	Schematic
1	LP-CVD oxide followed by Low-stress silicon nitride deposition on both sides.	Oxide: 1 μ m Nitride: 500nm	
2	Heater line pattern transfer	Cr/Au: 3/30 nm, lift-off	
3	Bi-material metal pattern transfer	Cr/Au: 3/125 nm, lift-off	
4	Suspended active area pattern transfer on nitride layer	Plasma etch	
5	Back-side opening pattern transfer on nitride and oxide	Plasma etch	
6	Through wafer etch and stopping on front-side oxide.	DRIE	
7	LTO wet etching and device release	HF etch	

Low-stress Silicon nitride: , LP-CVD silicon oxide , Heater line Au: , Bi-material Au: 

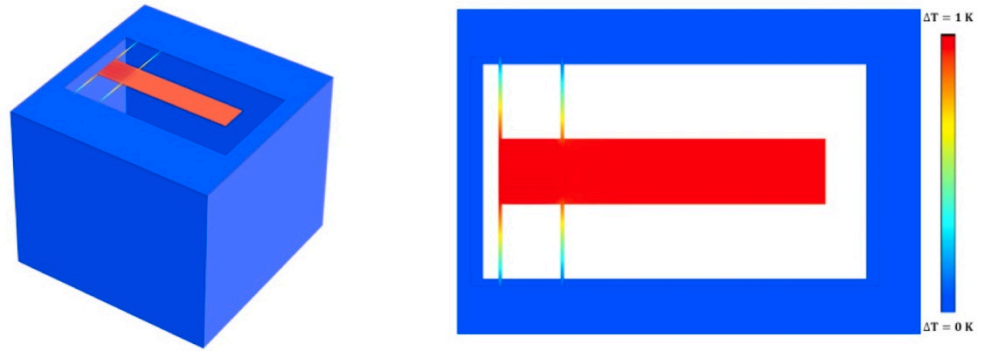


Figure 2-2- (a) The schematic of the device used for the FEM simulation. All boundaries except the top surface were held at 300K, whereas an insulating boundary condition is used for the top surface (b) FEM results verify that the thermal gradients within the suspended region of the device are negligible.

2-4- Estimation of the device thermal conductance and thermal time constant

The microdevice has a central region that is suspended by thin and long beams. Given this geometry it is reasonable to expect that the resistance to heat flow within the island is very small compared to the resistance to heat flow in the SiN_x beams. In order to validate this hypothesis, which was found to be true in similar suspended devices [24], we performed finite element method (FEM) simulations. In these simulations, heat was input into the suspended region of the device by simulating an electric current in the serpentine heater, which results in joule heating.

The boundary conditions used in the simulations along with the results obtained are shown in Figure 2-2a. The amount of current supplied was adjusted to produce a maximum temperature increase of ~ 1 K in the suspended micro-device. The resultant temperature distribution, displayed in Figure 2-2b, clearly shows that most of the temperature drop occurs in the suspending beams. Further, the suspended region of the device has very small

thermal gradients that are negligible. These simulations clearly confirm the validity of the above stated hypothesis.

Since the temperature differentials inside the island are very small, it is legitimate to use the lumped capacitance approach in which the temperature gradients inside the suspended region are neglected and all the resistance to heat flow is assumed to be in the beams. Under these assumptions, it is possible to model the thermal response $T(t)$ of the microdevice to sinusoidal heating by the following first order differential equation:

$$C \frac{dT(t)}{dt} + G_{Th} (T(t) - T_{ambient}) = q \sin(2\pi f_h t) \quad (2-1)$$

where C is the total heat capacity of the island, G_{Th} is the total thermal conductance of the SiN_x beams, $T_{ambient}$ is the temperature of the ambient, and $q \sin(2\pi f_h t)$ is the sinusoidal heat input with an amplitude q and frequency f_h . The solution to Equation (3-1) is:

$$T(t) = (T_0 - T_{ambient}) e^{-\frac{G_{Th} t}{C}} + \frac{q/C}{\sqrt{(G_{Th}/C)^2 + (2\pi f_h)^2}} \cos\left(\omega t + \tan^{-1}\left(\frac{C \times 2\pi f_h}{G_{Th}}\right)\right) + T_{ambient} \quad (2-2)$$

Upon reaching steady state, the amplitude of the temperature oscillation is $\frac{q/C}{\sqrt{(G_{Th}/C)^2 + (2\pi f_h)^2}}$, which decreases rapidly in magnitude when $2\pi f_h$ increases beyond G_{Th}/C . Therefore, the cut-off frequency for the device is, by definition, $G_{Th}/2\pi C$.

Using the linear model to evaluate the performance of the picowatt calorimeter described here, the thermal conductance of the beams, the thermal time constant of the device, and the expected temperature resolution of the bimaterial cantilever thermometer could be estimated. The thermal conductance (G_{Th}) of the beams, including the Au coating on them, is estimated to be $\sim 0.5 \mu\text{W/K}$ ($G_{Th} = 4 \times (k_{SiN_x} A_{SiN_x} + k_{Au} A_{Au}) / L_b$), where k_{SiN_x} ($\sim 2 \text{ W/m}\cdot\text{K}$) and k_{Au} ($< 100 \text{ W/m}\cdot\text{K}$) are the thermal conductivities of thin film SiN_x [25] and thin film

Au [26], respectively, A_{SiN_x} and A_{Au} are the areas of cross section of silicon nitride and gold in the beams, and L_b is the length of the beams.

Another parameter of interest is the thermal time constant (τ_{Th}) of the device, which limits the temporal response of the device. Presented lumped capacitance approach suggests that τ_{Th} is related to the thermal conductance of the beams (G_{Th}) and the total heat capacity of the suspended region by $\tau_{Th} = (\text{heat capacity of suspended region})/G_{Th}$. Given the device dimensions, this implies that the time constant is ~ 30 ms. This estimate suggests that sinusoidal heat currents at a frequency much smaller than the cutoff frequency f_0 ($1/2\pi\tau = 5.3\text{Hz}$) result in a full thermal response, whereas heat inputs at frequencies much larger than the cut-off frequency result in an attenuated thermal response.

2-5- Estimation of temperature resolution of bimaterial cantilever thermometer

Bimaterial cantilevers are well suited for detecting extremely small temperature changes [10]. A temperature change, ΔT , of a bimaterial cantilever results in deflections due to the differential expansion of SiN_x and Au. The deflection sensitivity of the cantilever can be obtained from:

$$\frac{\Delta z}{\Delta T} = \frac{-3(\gamma_1 - \gamma_2)(t_1 + t_2)l^2}{Kt_2^2} \quad (2-3)$$

where:

$$K = 4 + 6\left(\frac{t_1}{t_2}\right) + 4\left(\frac{t_1}{t_2}\right)^2 + \left(\frac{E_1 t_1}{E_2 t_2}\right)^3 + \left(\frac{E_2 t_2}{E_1 t_1}\right) \quad (2-4)$$

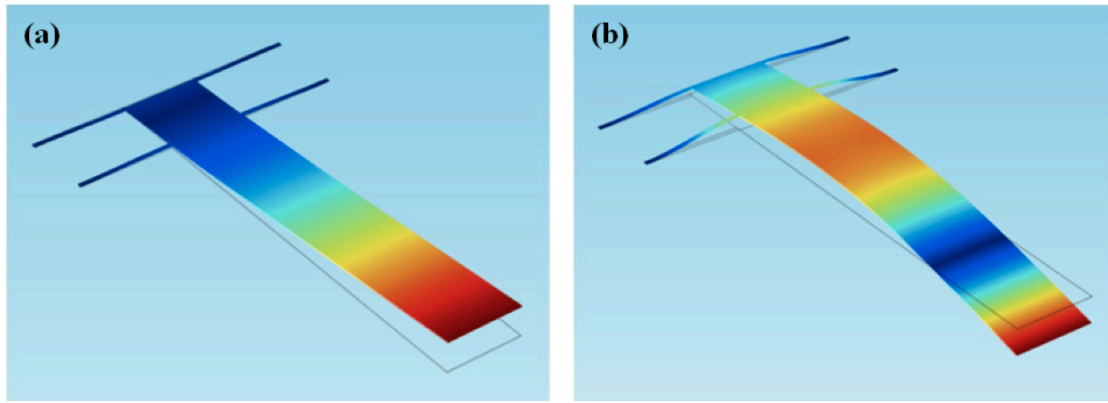


Figure 2-3- (a) 1st mode of cantilever deflection with a resonant frequency of about 6.2 KHz. (b) 2nd mode of cantilever deflection at a resonant frequency of ~44 KHz.

Here, Δz is the deflection of the tip of the cantilever and subscripts 1 and 2 refer to Au and SiN_x, respectively. The symbols $\gamma_{1,2}$ are the coefficients of thermal expansion, $E_{1,2}$ are the Young's moduli, t_1 and t_2 are the thicknesses, and l is the length of the cantilever. From the above equation the deflection sensitivity of the bimaterial cantilever used in this work is estimated to be ~257 nm/K. Therefore, if tip deflections are detected with a resolution of 0.01–0.001 nm, temperature changes of $\sim 4 \times 10^{-5}$ K to 4×10^{-6} K can be measured. Measurement of such small deflections can be accomplished by optical means and is implemented in this work.

We used the finite element method (FEM) to estimate the eigenfrequencies and eigenmodes of the microdevice. The primary goal of this analysis was to identify the shape and frequency corresponding to the first normal mode as this information is necessary to estimate the spring constant of this mode. We also computed the eigenfrequency corresponding to the second mode of the device so as to compare with experimental results. The computed results for the first two modes are shown in Figure (2-3)a and b. The first mode has a resonant frequency of ~6.2 KHz and a mode shape as shown in Figure (2-3)a. The 2nd mode has an eigen frequency of ~44 KHz and a mode shape as shown in Figure (2-3)b.

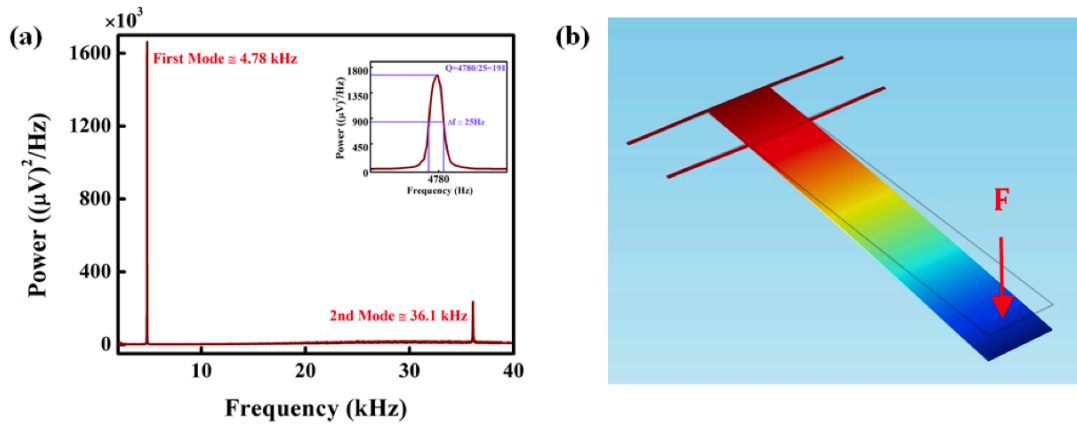


Figure 2-4- (a) Measured power spectral density displays peaks at 4.78 KHz and ~ 36.1 KHz corresponding to the first and second modes of the device (b) A point load of ~ 1 nN is applied to the end of the beam resulting in a tip displacement of about 50 nm, corresponding to spring constant of around 0.02 N/m.

In order to verify these results we obtained the power spectral density corresponding to the oscillations of the bimaterial cantilever when it is not excited by any electrical currents. The power spectral density is shown in Figure 2-4a and shows peaks at ~ 4.78 KHz and ~ 36.1 KHz. The 20 - 30% discrepancy between the computed and experimentally measured values probably arises from the inaccuracies in the values of the Young's modulus used in the FEM modeling.

In order to estimate the spring constant corresponding to the first normal mode, FEM analysis was performed. In this analysis, a point load of 1 nN was applied to the end of the cantilever, while the 4 ends of the suspending beams were held fixed. This resulted in a tip displacement of ~ 50 nm (Figure 2-4b), which translates to a spring constant of ~ 0.02 N/m. The quality factor of the device is defined as $(f_o/\Delta f)$, where f_o is the resonant frequency and $1-\Delta f$ is the bandwidth at half the maximum value of the peak. In this case, the resonant frequency is at ~ 4.78 KHz and the bandwidth at half the peak value is approximately 25 Hz (inset Figure 2-4a). Therefore, the quality factor (Q) of the device is ~ 190 .

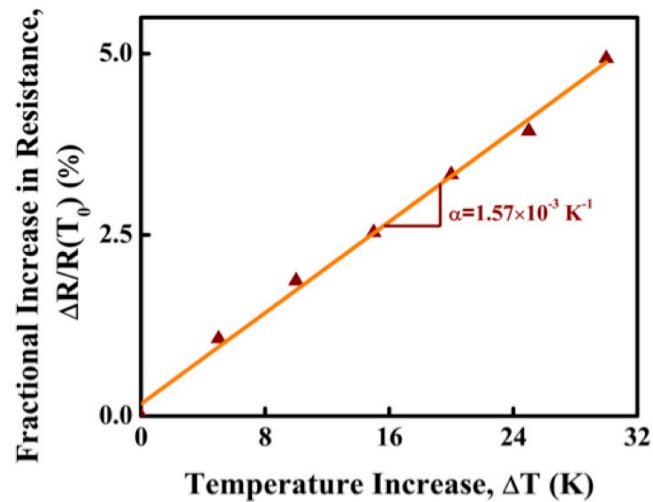


Figure 2-5- Results for the experimental measurement of TCR

2-6- Characterizing the thermal conductance of the device

In order to experimentally characterize the thermal conductance of the beams (G_{Th}) a sinusoidal current of known amplitude (I_0) and frequency (f) is supplied through the serpentine heater (Figure 2-1).

This current results in joule heating, $q = I_0^2 R / 2 \times [1 - \cos(2\pi \times 2f \times t)]$, where R is the resistance of the portion of the heater line embedded between the voltage measuring probes of the serpentine heater line (Figure 2-1). This heat input q has a second harmonic ($2f$) component, which results in temperature oscillations with amplitude ΔT_{2f} at a frequency $2f$. We note that when a sinusoidal current at a sufficiently low frequency is passed through the serpentine heater line, the thermal gradients within the suspended region are negligible. This is because the internal resistance to heat flow within the suspended region is much smaller than the thermal resistance within the beams that suspend the central region.

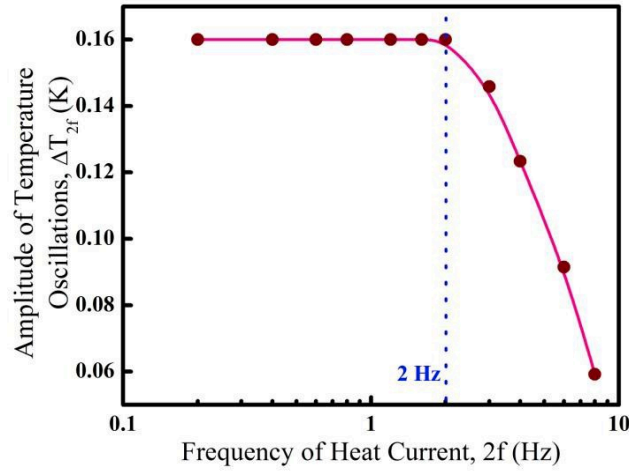


Figure 2-6- The thermal response of the microdevice as a function of the frequency ($2f$) of the input sinusoidal heat current.

Under these conditions, the amplitude of the temperature oscillations (ΔT_{2f}) of the island can be related to the amplitude of the voltage oscillations at $3f$ (V_{3f}) across the four-probe serpentine resistor integrated into the microdevice by $\Delta T_{2f} = 2V_{3f}/(I_0 R \alpha)$, where α is the temperature coefficient of resistance (TCR) for the Au line.

The Temperature Coefficient of Resistance (TCR), α , of the serpentine heater line was determined by measuring the line's electrical resistance ($R(T)$) at different temperatures (T).

The temperature dependence of the heater line resistance is given by:

$$R(T) = R(T_0) \times (1 + \alpha \Delta T) \quad (2-5)$$

where T_0 is the ambient temperature and ΔT is the difference between T and T_0 .

Therefore:

$$\frac{R(T) - R(T_0)}{R(T_0)} = \frac{\Delta R(\Delta T)}{R(T_0)} = \alpha \Delta T \quad (2-6)$$

Implying that α can be determined experimentally by calculating the slope of the curve relating $\frac{\Delta R(\Delta T)}{R(T_0)}$ to ΔT (Figure 2-5).

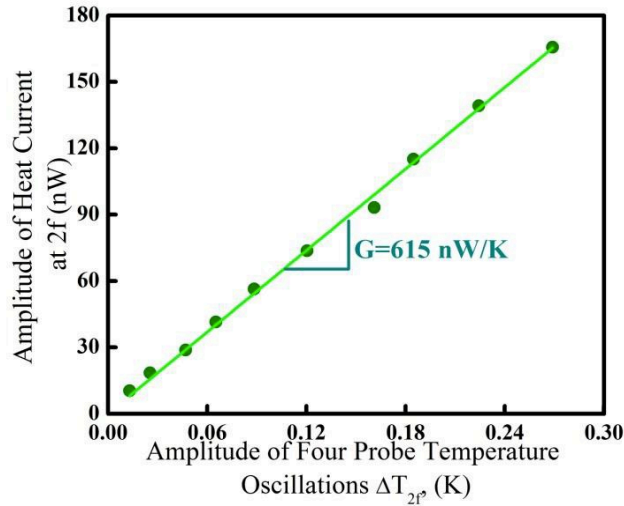


Figure 2-7- The measured amplitude of temperature oscillations of the suspended region (x-axis) for known inputs of heat currents (y-axis) at 2 Hz is shown, the slope of the curve gives the thermal conductance (~ 615 nW/K).

The measured amplitude of temperature oscillations for heat currents of fixed amplitude (~ 100 nW) at various frequencies are shown in Figure 2-6. The amplitude of temperature oscillations of the suspended region are invariant for frequencies less than or equal to 2 Hz (cut-off frequency ~ 5 Hz). However, for frequencies larger than the cut-off frequency the temperature response is attenuated as expected for a first order system. The thermal conductance of the beams is experimentally determined from the measured amplitude of temperature oscillations for known sinusoidal heat inputs using $G_{Th} = q(2f = 2Hz)/\Delta T_{2f}$, where $q(2f = 2Hz)$ is the amplitude of the sinusoidal heat input at 2 Hz and is well approximated by $I_0^2 R/2$.

The obtained temperature oscillations for various known heat inputs at 2 Hz are shown in Figure 2-7, the slope of which shows that the thermal conductance of the beams is $(0.615 \pm 0.04) \mu\text{W/K}$. The uncertainty ($\sim 7\%$) arises primarily from the joule heating in the beams.

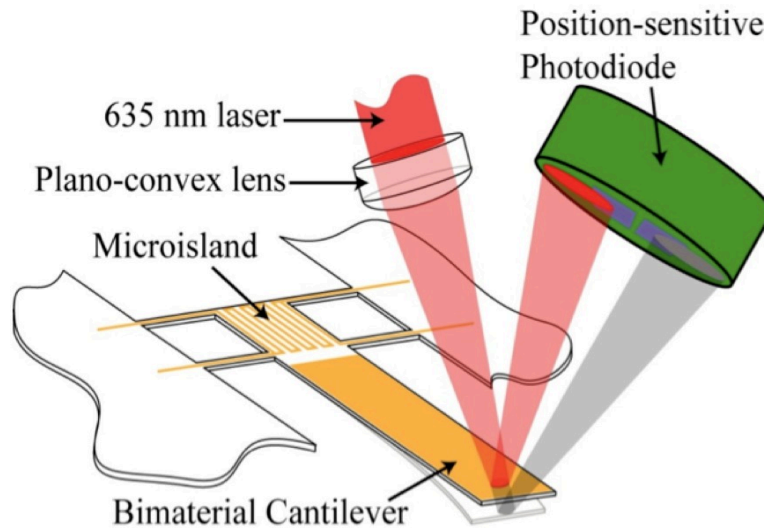


Figure 2-8- Schematic of optical detection scheme: A laser is focused by a lens and is reflected off the bimaterial cantilever, and finally detected by a position-sensitive photodiode.

2-7- Experimental characterization of bimaterial thermometer performance

Measuring heat currents with picowatt sensitivity requires excellent temperature resolution. To achieve this, a bimaterial cantilever sensor capable of $\sim 4 \mu\text{K}$ resolution [17] was integrated into the microdevice. The deflection of the bimaterial cantilever is proportional to the temperature change and is measured using an optical detection scheme that outputs a voltage signal (V_{Def}) proportional to the deflection (Figure 2-8). A 635-nm laser (Thorlabs S1FC635), focused by a plano-convex lens (Thorlabs LA1540), is focused onto the tip of the gold-coated bimaterial cantilever. The beam reflected from the cantilever is detected by a position-sensitive photodiode (PSD) (EG&G). In our experiments, sinusoidal electric currents were used to periodically heat the island and cantilever. This results in temperature oscillations, which in turn causes periodic bimaterial cantilever deflections. Consequently, the laser spot position on the PSD shifts periodically.

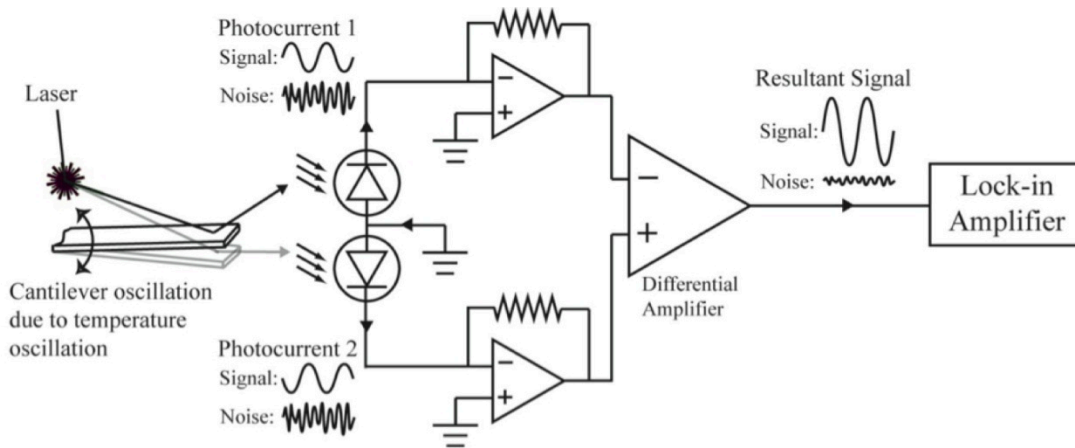


Figure 2-9- Circuit diagram outlining how voltage signal is produced from two anti-phase photocurrent signals arising from the oscillating cantilever deflection.

This periodic shift results in two sinusoidal photocurrent signals that are out of phase. The photocurrents are converted into a sinusoidal voltage signal, which has amplitude proportional to the deflection amplitude in the bimaterial cantilever (Figure 2-8).

The sinusoidal component of the resulting voltage signal is detected using a lock-in amplifier (Stanford Research Systems SR 830).

The temperature induced deflection response of the bimaterial cantilever was calibrated by using the four-probe thermometer (serpentine line) integrated into the device. Specifically, sinusoidal heat currents at 2 Hz ($2f$) (frequency chosen based on signal to noise ratio considerations described below) were input into the serpentine heater of the microdevice resulting in sinusoidal temperature oscillations.

The temperature oscillations were monitored by using the four-probe thermometer, while the amplitude of the oscillations of the bimaterial ($\Delta V_{Def,2f}$) at $2f$ was detected by the optical scheme and recorded using a lock-in amplifier (bandwidth of 1 mHz). The data obtained in these measurements (Figure 2-10) show that the deflection sensitivity is $\sim 8.4 \mu\text{V}/\mu\text{K}$.

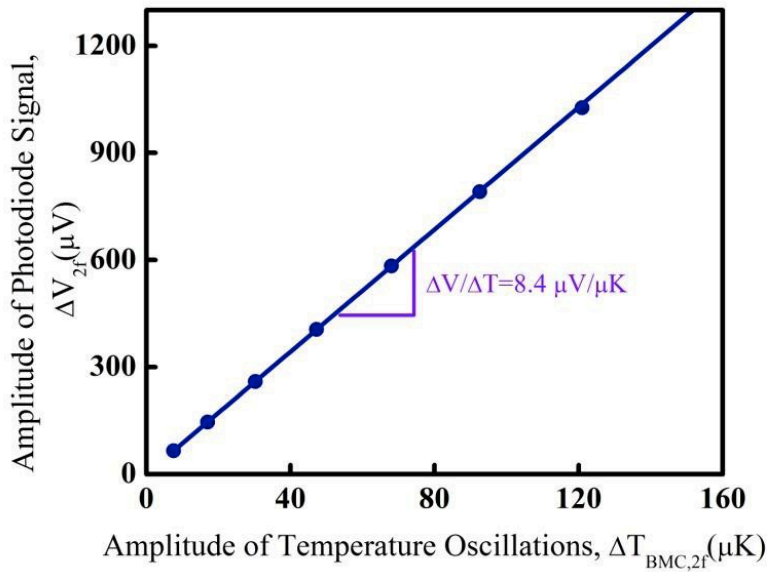


Figure 2-10- The response of the bimaterial cantilever thermometer is calibrated by inputting heat currents of known amplitudes at 2 Hz ($2f$) while simultaneously recording the bimaterial cantilever oscillations ($\Delta V_{Def,2f}$) and the temperature oscillations of the suspended region

2-8- Characterizing optimum frequency of calorimetry measurement

To determine the frequency corresponding to optimal performance of the device, the signal to noise ratio was characterized at various frequencies. The noise in the measured voltage ($\Delta V_{Def,2f}$) arises due to thermal fluctuations, random vibration sources that excite the cantilever, thermal drift, and electronic noise. To minimize the thermal drift and acoustic/seismic vibrations, all the studies were performed in a temperature controlled stage ($305 K \pm 1mK$), in a high vacuum chamber ($<10^{-6}$ Torr) located on an isolated optical table. The combined effect of all noise sources is quantified by the power spectral density (PSD) of V_{Def} in the absence of any heat input to the device. The measured PSD (Figure 2-11a) shows that noise is larger at lower frequencies. Such a behavior is expected due to the $1/f$ noise arising from thermal and electronic drift in the system. From the measured frequency dependence of the signal (Figure 2-11a) and the measured PSD, the signal to noise ratio is determined to have a maximum at ~ 2 Hz (Figure 2-11b).

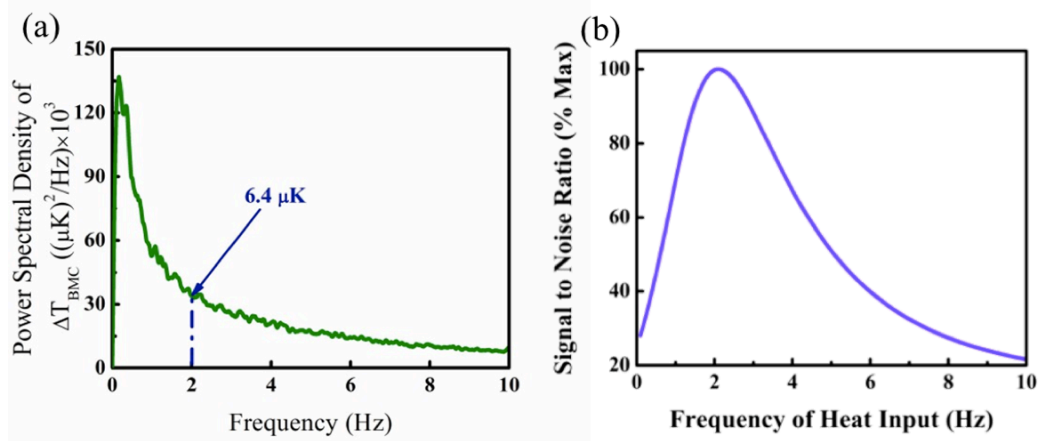


Figure 2-11- (a) The power spectral density (PSD) of the noise in the bimaterial cantilever deflections (b) Signal to Noise Ratio at Different Frequencies. The optimum signal to noise ratio was found to occur around 2 Hz; this frequency was used for all the further measurements. For more details, see the main manuscript.

2-9- Experimental determination of the resolution of the heat flow calorimeter

To experimentally determine the ultimate sensitivity of the device, picowatt-level sinusoidal thermal excitations were applied via the serpentine heater and temperature oscillations ($\Delta T_{BMC,2f}$) were detected from the bimaterial cantilever (Figure 2-12). Each data point in Figure 2-12 corresponds to the mean of 10 individual measurements, and the error bar represents the standard deviation. These data show that even when no power is input, the drift in the bimaterial cantilever corresponds to a temperature oscillation (ΔT_{noise} of ~ 6.4 μK). This shows that the noise equivalent power input ($q_{NEP} = G_{Th} \times \Delta T_{noise}$) of the device is ~ 4 pW. To determine the resolution of the device, the power input to the device was increased from 0 to 40 pW in steps of 2 pW. The measured mean values of $\Delta T_{BMC,2f}$ are found to increase directly proportionally with the thermal loading, demonstrating that changes in heat currents smaller than 4 pW can be resolved.

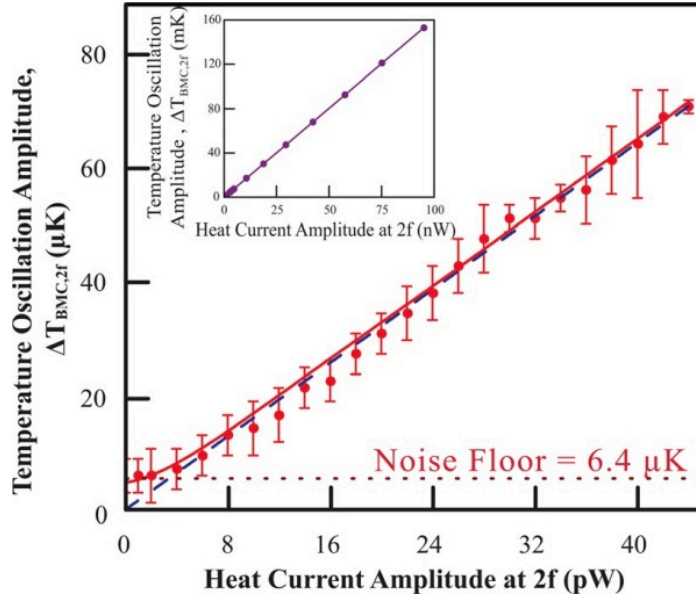


Figure 2-12- The measured temperature oscillations ($\Delta T_{BMC,2f}$ determined using the bimaterial cantilever) for various inputs of sinusoidal heat currents (0–44 pW, increased in steps of 2 pW) at 2 Hz. The noise floor of the device ($\sim 6.4 \mu K$) corresponds to <4 pW heat inputs. In the inset the response of the device to heat inputs of up to 100 nW is shown, demonstrating a dynamic range exceeding three orders of magnitude.

In order to determine the dynamic range of the device, the amplitude of sinusoidal heat input was varied from 10 pW to 100 nW, while the temperature oscillations were measured by monitoring the deflections of the bimaterial cantilever (Figure 2-12). Remarkably, the response of the device is linear over the entire range suggesting that the dynamic range of the device spans at least three orders of magnitude. Although the device response is linear for this large range, the response for low heat inputs (~ 0 –10 pW) is non-linear (Figure 2-12). This behavior can be understood by inspecting the governing equation of such a system as:

$$m\ddot{x}(t) + c\dot{x}(t) + kx(t) = f_s(t) + f_R(t) \quad (2-7)$$

here m is the mass, c is the damping coefficient, k is the spring constant, $x(t)$ is the deviation from the equilibrium position at any instant t , $f_s(t)$ is a sinusoidal signal of frequency ω_c and $f_R(t)$ is a random force whose time average is zero for sufficiently long times (Figure 2-13). Upon taking a Fourier transform Equation (2-7) can be transformed to:

$$-m\omega^2 X(\omega) + ic\omega X(\omega) + kX(\omega) = F_S(\omega) + F_R(\omega) \quad (2-8)$$

Here, $X(\omega)$, $F_S(\omega)$ and $F_R(\omega)$ are the Fourier transforms of $x(t)$, $f_S(t)$ and $f_R(t)$ respectively. Equation (2-8) be written in the following form:

$$X(\omega) = \frac{(F_S(\omega) + F_R(\omega))}{(k - m\omega^2) + (ic\omega)} \quad (2-9)$$

This suggests that:

$$|X(\omega)|^2 = \frac{[F_S(\omega) + F_R(\omega)] \times [F_S(\omega) + F_R(\omega)]^*}{(k - m\omega^2)^2 + (c\omega)^2} \quad (2-10)$$

When a measurement is made with a lock-in amplifier at a frequency ω_c and bandwidth BW , the measured deflection signal is given by:

$$\langle x_{deflection}^2 \rangle = \lim_{x \rightarrow \infty} \frac{1}{T} \left[\int_{-\omega_c - BW/2}^{-\omega_c + BW/2} |X(\omega)|^2 d\omega + \int_{\omega_c - BW/2}^{\omega_c + BW/2} |X(\omega)|^2 d\omega \right] \quad (2-11)$$

where $\langle x_{deflection}^2 \rangle$ is the mean square deflection value by the lock-in amplifier. On substituting (2-10) in (2-11) and on simplification we obtain:

$$\langle x_{deflection}^2 \rangle = \lim_{x \rightarrow \infty} \frac{1}{T} \left[\int_{-\omega_c - BW/2}^{-\omega_c + BW/2} \frac{|F_S(\omega)|^2 + |F_R(\omega)|^2 + F_S(\omega)F_R(\omega)^* + F_R(\omega)F_S(\omega)^*}{(k - m\omega^2)^2 + (c\omega)^2} d\omega + \int_{\omega_c - BW/2}^{\omega_c + BW/2} \frac{|F_S(\omega)|^2 + |F_R(\omega)|^2 + F_S(\omega)F_R(\omega)^* + F_R(\omega)F_S(\omega)^*}{(k - m\omega^2)^2 + (c\omega)^2} d\omega \right] \quad (2-12)$$

This can be further simplified to obtain:

$$\langle x_{deflection}^2 \rangle = \langle x_S^2 \rangle + \langle x_R^2 \rangle + \lim_{x \rightarrow \infty} \frac{1}{T} \left[\int_{-\omega_c - BW/2}^{-\omega_c + BW/2} \frac{F_S(\omega)F_R(\omega)^* + F_R(\omega)F_S(\omega)^*}{(k - m\omega^2)^2 + (c\omega)^2} d\omega + \int_{\omega_c - BW/2}^{\omega_c + BW/2} \frac{F_S(\omega)F_R(\omega)^* + F_R(\omega)F_S(\omega)^*}{(k - m\omega^2)^2 + (c\omega)^2} d\omega \right] \quad (2-13)$$

Here, $\langle x_S^2 \rangle$ and $\langle x_R^2 \rangle$ represent the mean square deflection of the sinusoidal and random forces applied independently. Using Parseval's identity:

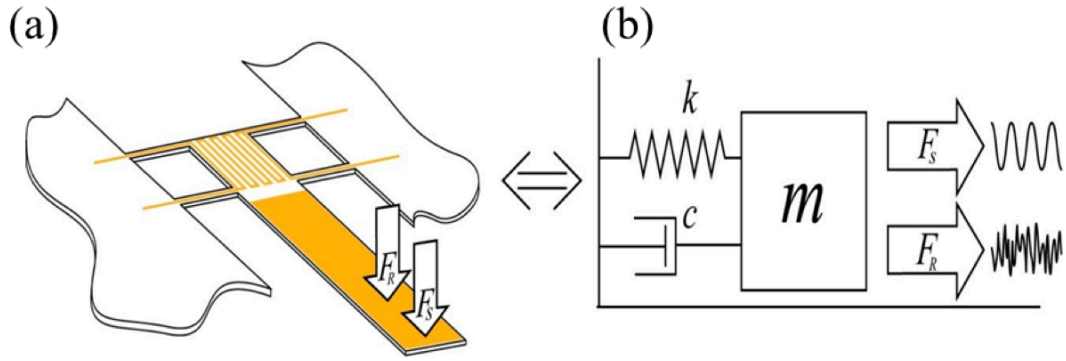


Figure 2-13- (a) Depicts a microdevice that is simultaneously excited by a sinusoidal force (FS) and a random force (FR). (b) A simplified model that captures the effect of the two forces on the bimaterial cantilever.

$$\int_{-\infty}^{+\infty} f_S(t)f_R^*(t)dt = \int_{-\infty}^{+\infty} F_S(\omega)F_R(\omega)^* d\omega \quad (2-14)$$

In conjunction with the fact that $f_S(t)$ is a sinusoidal signal of frequency ω_c and $f_R(t)$ is a random signal whose time average is zero, it can be shown that the limit of the sum of the integrals in Equation (2-13) is zero. Therefore, it can be shown that:

$$\langle x_{deflection}^2 \rangle = \langle x_S^2 \rangle + \langle x_R^2 \rangle \quad (2-15)$$

Therefore, the amplitude of the bimaterial cantilever oscillation is determined by: (1) the amplitude of sinusoidal heat inputs, which results in bimaterial cantilever oscillations with a mean square value of $\langle x_S^2 \rangle$ and (2) random forces arising from thermal noise and ambient mechanical vibrations, which in the absence of any other forces results in a displacement with a mean square value of $\langle x_R^2 \rangle$. The combined effect of these two forces is to give a total cantilever deflection whose RMS value $\langle x_{deflection}^2 \rangle^{1/2}$, which is shown by solid line in Figure 2-12 and is seen to agree well with the experimentally obtained data.

2-10- Conclusion

In this chapter, I have demonstrated a calorimetric technique capable of a resolution better than 4 pW at room temperature—an order of magnitude improvement over state-of-the-art methods. This is achieved by integrating an ultra-sensitive bimaterial cantilever based thermometer into a suspended microdevice. This device is well suited for the study of nanoscale thermal transport and is expected to be an important tool for nanoscale heat transport studies where heat flows on the order of a few picowatts are expected to occur.

CHAPTER 3

High Resolution Resistive Thermometry for Micro and Nanoscale Measurements

3-1- Abstract

High resolution thermometry plays an important role in several micro and nano scales studies. In this chapter, I present a detailed analysis of the resolution of resistance thermometry schemes that employ an electrical sensing current to monitor the temperature-dependent resistance. Specifically, I theoretically and experimentally analyze four different schemes where modulated or unmodulated temperatures in microdevices are measured using modulated or unmodulated sensing currents. This analysis and experiments suggest that measurement of unmodulated temperatures using a modulated sensing current improves the resolution in comparison to a scenario where an unmodulated sensing current is used. However, depending on the exact measurement conditions, such improvements might be modest as the overall resolution may be limited by random low frequency environmental temperature fluctuations. More importantly, I demonstrate that high-resolution thermometry can be achieved in the measurement of modulated temperatures. Specifically, we show that by using appropriate instrumentation and a 10 k Ω platinum resistance thermometer it is possible to measure modulated temperatures (0.5 – 20 Hz) with a resolution of about 20 - 100 μ K. The advances described here will enable a dramatic improvement in the heat-current resolution of resistive thermometry based microdevices that are used for probing nanoscale phonon and photon transport.

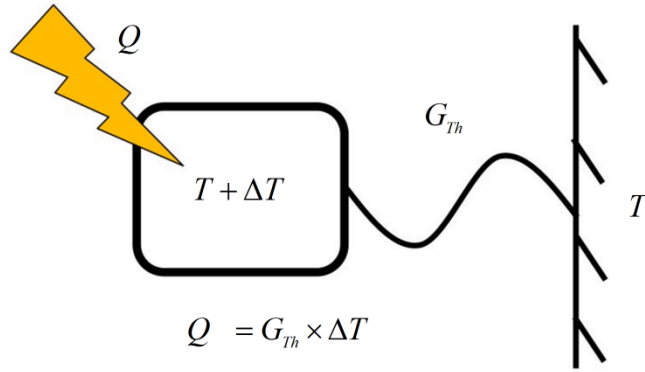


Figure 3-1- Principle of heat flow calorimetry. The sensing stage is isolated from the thermal reservoir by a finite thermal conductance (G_{th}). The magnitude of the heat output/heat current is quantified by measuring the temperature difference ΔT .

3-2- Introduction

High-resolution thermometry plays a critical role in the function of a variety of microdevices [13, 14, 24, 27] including ultra-high resolution calorimeters [28-32], scanning thermal imaging probes [33, 34], and suspended microdevices used for probing energy transport at the nanoscale [24, 35, 36]. As a concrete example, consider the role of thermometry in probing nanoscale heat transport. A majority of nanoscale heat transport studies utilize a microfabricated suspended island with an integrated thermometer that functions as a heat flow calorimeter [28] (Figure 3-1). The ultimate heat flow resolution (Q_{Res}) of such a microdevice depends on the thermal conductance between the thermally isolated region and the thermal reservoir (G_{Th}) and the resolution of the thermometer (ΔT_{Res}) and is given by $Q_{Res} = G_{Th} \cdot \Delta T_{Res}$. Therefore, performing high-resolution thermometry is critical for measuring small heat currents.

Resistance thermometry is one of the most widely used approaches to measure temperature changes at the microscale. The popularity of this approach stems from the relative ease with which it can be implemented in comparison to other approaches such as bimaterial cantilever based thermometers that offer high resolution [10, 14, 17, 18].

Microscale resistance thermometry is typically implemented using a thin film platinum resistance thermometer (PRT), whose electrical resistance increases almost linearly with temperature over a wide range of temperatures.

In this chapter, I present a detailed analysis of the noise characteristics of resistance thermometers. I analyze various contributions to noise that limit the resolution of resistance thermometry. Specifically, I analyze the resolution of PRTs in four different scenarios: 1) measurement of an unmodulated temperature using an unmodulated (DC) electrical current, 2) measurement of an unmodulated temperature using a sinusoidally modulated sensing current, 3) measurement of a modulated temperature using an unmodulated sensing current, and 4) measurement of a sinusoidally modulated temperature using a sinusoidal sensing current. This analysis and experiments identify the limits to resolution in each of these scenarios and provide the information necessary to determine when each of these schemes can be beneficially employed.

3-3- Noise sources in resistance thermometry

Resistance thermometry is based on the measurement of the electrical resistance (R) of a temperature-dependent resistive element that is in thermal equilibrium with the object whose temperature (T) is to be measured. To understand the factors that limit the resolution of a resistance thermometer it is instructive to consider the configuration shown in Figure 3-2a.

In such a configuration, the resistance ($R(T)$) is monitored by passing a known sensing current (I_s) through it and measuring the resulting potential difference (V) across it. Subsequently, the desired temperature is obtained from the calibrated relationship between electrical resistance and temperature. Although resistors made from copper, gold, platinum, and niobium are used, platinum(Pt) resistance thermometers (PRTs) are the most popular choice due to their stability in different environments[37] and the almost linear dependence of their resistance on temperature [38, 39] over a broad range of temperatures.

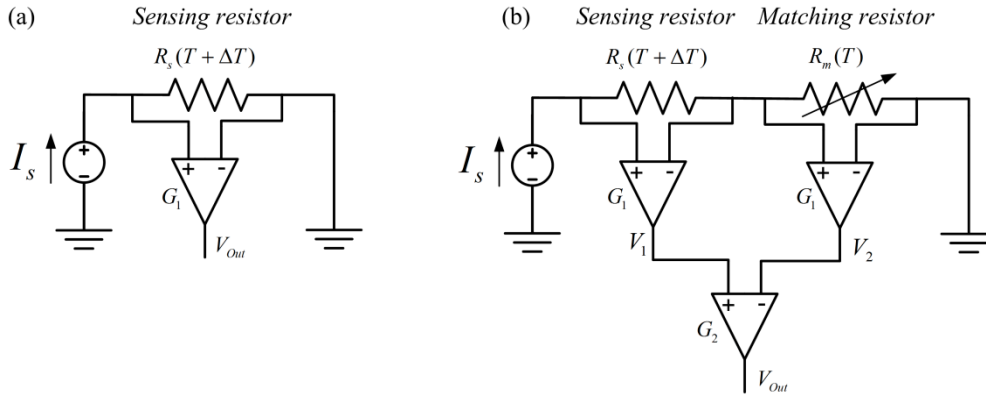


Figure 3-2- Principle of resistive thermometry. (a) The electrical resistance is monitored by passing a known current and measuring the voltage drop across the resistor. The temperature of the object of interest is obtained by calibrating the relationship between resistance and temperature. (b) Differential measurement scheme for isolating the signal of interest by rejecting the common mode voltage and the common mode noise arising from the noise in the electrical current ($I_{s,NI}$). The effect of drift in the environmental temperature is also attenuated by the differential

The measured temperature dependence of the PRTs is typically tabulated using the Callendar-Van Dusen equation [38, 39] or other polynomial relations[38, 39]. Alternatively, it is also expressed in a closed form using the Bloch-Grüneison formula[40].

In order to measure small temperature changes it is convenient to define a term called the temperature coefficient of resistance (TCR), which is conventionally denoted by the symbol α . At any temperature, TCR is defined by $\alpha(T) = (dR/dT)/R(T)$. The change in the temperature of the resistor (ΔT) can then be directly obtained from $\Delta T = \Delta V_{RTI} / [I_s R(T) \alpha]$, where ΔV_{RTI} is obtained by dividing the voltage change (ΔV_{Out}) at the output of the amplifier by the amplifier gain G_I . We note that the voltage changes are measured in a bandwidth Δf . This equation suggests that the noise equivalent temperature (NET) that represents the temperature resolution (ΔT_{Res}) of a resistance based thermometer is given by:

$$\text{NET} = \Delta T_{Res} = \frac{\Delta V_{Noise, RTI}}{[I_s R(T) \alpha]}, \quad (3-1)$$

where $\Delta V_{Noise, RTI}$ is the root mean square (RMS) value of the voltage noise (measured relative to the inputs) in the measurement bandwidth Δf . This suggests that, if the heating

power is not a constraint, employing large sensing currents (I_s) or choosing a PRT with a large R can enable very high resolution measurements. However, in certain scenarios large sensing currents result in self-heating effects that are detrimental to the measurement as well as device stability, in which case it is necessary to choose a resistance thermometer with a larger value of α to obtain a higher resolution. Specifically, the impact of self-heating on the temperature rise depends on the thermal conductance (G_{th}) between the thermally isolated region and the thermal reservoir (Figure 3-1) and must be taken into account while choosing the sensing current. Further, we note that in microdevices it is not always feasible to increase the resistance to large values due to constraints on the maximum possible footprint of the resistor. Hence, to maximize temperature resolution it is important to understand the limitations imposed by various noise sources on $\Delta V_{Noise, RTI}$. The noise in the voltage signal has multiple components, which could be broadly categorized as *intrinsic* (Johnson and shot) and *non-intrinsic* noise (e.g. $1/f$ noise, amplifier noise etc.). To perform high-resolution thermometry, it is necessary to quantify the contribution of these noise sources. We now provide a brief description of the power spectral density (PSD) of various noise sources.

Johnson noise arises due to spontaneous thermal fluctuations of charge in a resistor. For frequencies below 1 MHz and temperatures above 25 K the PSD of Johnson noise is well approximated by [41] $PSD_{V, Johnson} [V^2/Hz] = 4k_B TR$, where k_B is Boltzmann's constant, T is the equilibrium temperature of the reservoir, and R is the resistance (the units of the PSD are shown in the square brackets). Shot noise arises from the granular nature of charge, which manifests itself as fluctuations in the sensing current. The power spectral density of shot noise is well approximated by [41] $PSD_{I, Shot} [Amp^2/Hz] = 2qI_s$, where q is the charge of a proton, and I_s is the magnitude of the sensing current supplied through the resistor (Figure 3-2a). In addition to this noise, the sensing current may also have additional noise contributions due to non-idealities (NI) in the current source, which can be quantified by

directly measuring the PSD of the current source ($PSD_{I, NI}$)[Amp²/Hz]. The low frequency noise arising from ambient temperature changes and structural changes in the electronic components comprising the measurement setup is collectively called $1/f$ noise. Since an *a priori* estimation of the power spectral density of $1/f$ noise ($PSD_{1/f}$ [V²/Hz]) is usually difficult it is characterized experimentally.

Amplifier noise is the cumulative effect of non-idealities in the amplifier components, which manifest as voltage noise at the output of an amplifier. Amplifier noise has two independent components: the relative-to-input voltage noise (RTI) and input current (IC) noise[42]. The power spectral density of the RTI noise ($PSD_{V, RTI}$ [V²/Hz]) depends on both the gain of the amplifier and frequency. The IC noise of the amplifier is a frequency dependent noise at the input of the amplifier due to a finite current flow into the amplifier and is represented by $PSD_{I, IC}$ [Amp²/Hz]. The noise arising from the non-ideal characteristics of the current source is represented by $PSD_{I, NI}$ [Amp²/Hz]. The contribution of each of these sources depends on the detailed design of the amplifier/instrument under consideration and is usually characterized experimentally.

The total power spectral density of noise ($PSD_{Noise, RTI}$) relative to the input of the amplifier shown in Figure 3-1a can be obtained from (assuming that all noise are uncorrelated)[43]:

$$PSD_{Noise, RTI} = [(PSD_{V, Johnson}) + (PSD_{I, Shot} + PSD_{I, NI} + PSD_{I, IC})R^2 + PSD_{V, RTI} + PSD_{V, 1/f}]. \quad (3-2)$$

The RMS value of the voltage noise relative to the inputs ($\Delta V_{Noise, RTI}$), in the bandwidth of interest ($f_0, f_0 + \Delta f$), can then be obtained from:

$$\Delta V_{Noise, RTI} = \left[\int_{f_0}^{f_0 + \Delta f} PSD_{Noise, RTI}(f) df \right]^{1/2}. \quad (3-3)$$

Using this expression and Equation (3-1) the NET of a resistance thermometer can be estimated.

Differential scheme for measuring small temperature changes: Measurement of small temperature changes using the scheme shown in Figure 3-2a, especially when the temperature changes are unmodulated, is limited by fluctuations in ambient temperature, which leads to spurious measurements. Furthermore, since the change in the voltage signal resulting from the small temperature change, ΔT , is relatively small, an instrument with a large dynamic range is required.

The problems associated with temperature drift and the required dynamic range can be addressed by adopting the differential scheme shown in Figure 3-2b, which in fact represents one half of a Wheatstone bridge network. Full bridge configurations are frequently employed in related measurement applications (with some relatively small advantages and disadvantages), but since it is generally not feasible to fabricate multiple sensing resistors into micro- and nanoscale device structures of interest, we focus in this work on the configuration shown in Figure 3-2b. Overall, this configuration offers lower noise given the smaller overall source resistance. We note that the analysis for a full bridge is nearly identical.

In the configuration shown in Figure 3-2b, a second “matching” resistor whose resistance and TCR values are chosen to be “very” close to that of the “sensing” resistor is incorporated. The sensing resistor experiences a temperature change ΔT whereas the matching resistor does not. The voltage outputs across the sensing and matching resistors are measured using two instrumentation amplifiers (first stage) and subsequently subtracted from each other using another instrumentation amplifier (second stage). This scheme accomplishes two purposes: 1) the common mode voltage across the two resistors is eliminated (discussed in more detail below), enabling the isolation of the signal arising from the temperature change ΔT , and 2) if the matching resistor is in excellent contact with the same thermal reservoir that the sensing resistor is coupled to, then the effects of environmental temperature drift can be significantly attenuated as both the resistors will sense similar (although not identical) temperature drifts.

Table 3-1- Different schemes for resistance thermometry. The temperature is either modulated at a frequency (f_T) or is not modulated. Similarly, the electrical current for sensing resistance changes is either modulated at a frequency (f_s) or is not modulated.

<i>Scheme</i>	<i>Temperature Change</i>	<i>Sensing Current</i>	<i>Sensing Frequency</i>
1	<i>Unmodulated, $f_T=0$</i>	<i>Unmodulated, $f_s=0$</i>	0
2	<i>Unmodulated, $f_T=0$</i>	<i>Modulated, f_s</i>	f_s
3	<i>Modulated, f_T</i>	<i>Unmodulated, $f_s=0$</i>	f_T
4	<i>Modulated, f_T</i>	<i>Modulated, f_s</i>	$f_s - f_T, f_s + f_T$

As explained later, the use of such a thermally coupled matching resistor is critical for the measurement of unmodulated temperature changes—in fact, this idea is the key to the improvements reported by Wingert *et al.* [27, 35] in their recent work on probing heat transfer in nanostructures with high resolution.

3-4- Schemes to measure sinusoidally modulated and unmodulated temperature changes

In this section I present a detailed discussion of different resistance thermometry schemes summarized in Table 3-1. Specifically, I will examine the advantages and disadvantages of the four possible schemes involving the measurement of unmodulated or sinusoidally modulated temperatures using unmodulated or sinusoidally modulated sensing currents. Further, we also develop expressions to estimate the resolution achievable using each of these schemes.

A. Scheme 1: Measurement of unmodulated temperature changes (ΔT) using unmodulated sensing current (I_s)

In this *scenario*, the output signal of the second stage amplifier (Figure 3-2b) is given by:

$$V_{Out} = \underbrace{G_1 G_2 [I_s R \alpha \Delta T]}_{V_{Signal}} + \Delta V_{Noise} \quad (3-4)$$

where, G_2 is the gain of the stage 2 amplifier (Figure 3-2). Equation (3-4) shows that the signal of interest is at $f = 0$ Hz as both the sensing current and the temperature change are unmodulated. The voltage noise (ΔV_{Noise}) can be obtained by estimating the power spectral density of the noise at the output of the second stage amplifier ($PSD_{Amp\ Total}$):

$$PSD_{Amp\ Total}(f) = \left[2[PSD_{noise, RTI}(f) - PSD_{I, NI}(f)R^2]G_1^2 + PSD_{V, RTI, Amp2}(f) + PSD_{V, 1/f, Amp2}(f) + PSD_{IC, Amp2}(f) \right] G_2^2, \quad (3-5)$$

where $PSD_{Noise, RTI}$ is defined by Equation (3-2) $PSD_{I, NI}$ is the noise due to the non-ideal behavior of the current source, $PSD_{V, RTI, Amp2}$ refers to the relative to input noise of the stage 2 amplifier, and $PSD_{V, 1/f, Amp2}$ and $PSD_{IC, Amp2}$ refer to the $1/f$ and input current noise, respectively, of the stage 2 amplifier (Figure 3-2b). We note that in Eq.(3-5), $PSD_{I, NI}(f)R^2$ is subtracted from the $PSD_{Noise, RTI}$ because the effect of non-ideality of the current source is eliminated in a differential scheme. The power spectral density of the noise is usually reported relative to input as ($PSD_{Amp\ Total, RTI}$):

$$PSD_{Amp\ Total, RTI}(f) = \frac{PSD_{Amp\ Total}(f)}{[G_1 G_2]^2}. \quad (3-6)$$

Therefore, the mean square voltage noise at $f = 0$ Hz (the frequency of interest here), relative to the inputs, can now be estimated as:

$$\Delta V_{Amp\ Total, RTI, S1}^2 = \int_0^{\Delta f} PSD_{Amp\ Total, RTI}(f) df, \quad (3-7)$$

where Δf is the bandwidth of the measurement. We note that in this scheme, $\Delta V_{Amp\ Total, RTI, S1}$ is large because $PSD_{Amp\ Total, RTI}(f=0\text{Hz})$ is expected to have large contributions from $1/f$ noise.

In addition to the voltage noise described above, it is also necessary to consider the effect of the relative drift in the temperatures of the sensing and matching resistors. To elaborate, let the temperature of the sensing resistor, at time t , be $T_1(t) + \Delta T$, where ΔT is the unmodulated temperature to be measured, whereas the temperature of the matching resistor is $T_2(t)$. Ideally, $T_2(t) - T_1(t)$ should be equal to zero, in which case the temperature difference between the matching and sensing resistors would be equal to ΔT .

However, due to temperature drift the actual temperature difference (ΔT (*non-ideal*)) is given by:

$$\Delta T(\text{non ideal}) = \Delta T(\text{ideal}) + [T_1(t) - T_2(t)] = \Delta T(\text{ideal}) + \Delta T_{\text{Drift}}(t). \quad (3-8)$$

The effect of temperature related drift can be quantified from a knowledge of the power spectral density of ΔT_{Drift} , $PSD_{\Delta T, \text{Drift}}$ [K^2/Hz]. The mean square voltage noise, relative to the input, associated with temperature drift $\Delta V_{\text{Temperature Drift, RTI}}$ can then be expressed as:

$$\Delta V_{\text{Temperature Drift, RTI, S1}}^2(f = 0\text{Hz}) = (I_s R \alpha)^2 \int_0^{\Delta f} PSD_{\Delta T, \text{Drift}}(f) df, \quad (3-9)$$

In practice this effect is frequently large because the relative temperature drift at low frequencies can be substantial (quantified in section 3-6-). Therefore, the noise equivalent temperature for scheme 1 ($\text{NET}_{\text{Scheme 1}}$) can be expressed as:

$$\text{NET}_{\text{Scheme 1}} = \frac{\left[\Delta V_{\text{Amp Total, RTI, S1}}^2 + \Delta V_{\text{Temperature Drift, RTI, S1}}^2 \right]^{1/2}}{I_s R \alpha}. \quad (3-10)$$

This equation suggests that $\text{NET}_{\text{Scheme 1}}$ will be limited by $\Delta V_{\text{Amp Total, RTI, S1}}^2(f = 0\text{Hz})$ and/or $\Delta V_{\text{Temperature Drift, RTI, S1}}^2(f = 0\text{Hz})$, depending on their relative magnitude.

B. Scheme 2: Measurement of unmodulated temperature changes (ΔT) using modulated sensing current (I_s)

The large contribution of low frequency noise to the NET in scheme 1 can be significantly reduced by using a modulated sensing current ($I_s \sin(2\pi f_s t)$). The output voltage signal in this scheme is given by:

$$V_{Out} = G_1 G_2 \underbrace{[I_s \sin(2\pi f_s t) R \alpha \Delta T]}_{V_{Signal}} + \Delta V_{Noise} \quad (3-11)$$

where I_s and f_s are the amplitude and frequency of the sensing current, respectively. Equation (3-11) shows that the signal of interest is now modulated at frequency f_s , which can usually be chosen to be sufficiently large to effectively reduce voltage noise. This can be best understood by noting that the mean square voltage noise is given by:

$$\Delta V_{Amp\ Total, RTI, S2}^2 (f = f_s \text{ Hz}) = \int_{f_s - \Delta f/2}^{f_s + \Delta f/2} PSD_{Amp\ Total, RTI} (f) df \quad (3-12)$$

Therefore, if f_s is large (say >100 Hz) the voltage noise will be substantially smaller as compared to low frequencies where the contribution of the $1/f$ noise is large. With a modulated sensing current ($I_s \sin(2\pi f_s t)$), the mean square voltage noise associated with the temperature drift, at the frequency of interest (f_s), is given by (see Appendix for more details):

$$\Delta V_{Temperature\ Drift, RTI, S2}^2 (f = f_s \text{ Hz}) \sim \frac{(I_s R \alpha)^2}{2} \int_0^{\Delta f/2} PSD_{\Delta T, Drift} (f = 0 \text{ Hz}) df \quad (3-13)$$

The noise equivalent temperature for scheme 2 ($NET_{Scheme\ 2}$) is therefore given by:

$$NET_{Scheme\ 2} = \frac{\left[\Delta V_{Amp\ Total, RTI, S2}^2 + \Delta V_{Temperature\ Drift, RTI, S2}^2 \right]^{1/2}}{I_s R \alpha} \quad (3-14)$$

Equations (3-13) and (3-14) suggest that by using a modulated sensing current the effect of $1/f$ voltage noise can be substantially reduced. However, the effect of temperature drift between the *matching* and *sensing* resistors can still be large because $PSD_{\Delta T, Drift} (f = 0 \text{ Hz})$

is typically large at low frequencies (quantified in section 3-6-). Thus, minimizing $PSD_{\Delta T, Drift}$ at low frequencies is critical for further reducing the NET.

C. Scheme 3: Measurement of modulated temperature changes (ΔT) using an unmodulated sensing current (I_s)

We now consider a measurement scheme where the temperature can be modulated at a known frequency f_T . Measurement of modulated temperatures is critical for performing high-resolution calorimetry[28] and photothermal measurements[17]. In order to measure modulated temperature oscillations, we consider the situation where the sensing current (I_s) is not modulated, i.e. $f_s = 0$ Hz. In the scheme shown in Figure 3-2b, only the sensing resistor experiences periodic temperature modulations ($\Delta T \sin(2\pi f_T t)$) which results in a voltage signal at the output of the second amplifier given by:

$$V_{Out} = G_1 G_2 \underbrace{[I_s R \alpha \Delta T \sin(2\pi f_T t)]}_{V_{Signal}} + \Delta V_{Noise}, \quad (3-15)$$

where the signal of interest is at $f = f_T$ Hz. The mean square noise voltage in this scheme can be obtained from:

$$\Delta V_{Amp\ Total, RTI, S3}^2(f = f_T \text{ Hz}) = \int_{f_T - \Delta f / 2}^{f_T + \Delta f / 2} PSD_{Amp\ Total, RTI}(f) df. \quad (3-16)$$

If the frequency of the temperature modulation f_T can be chosen to be relatively large (> 100 Hz) the PSD of the voltage noise in Eq. (3-16) can be small relative to the $1/f$ noise. Further, in this scheme the voltage noise associated with temperature drift can also be minimized. To elaborate, the RMS temperature fluctuation ($\Delta T_{Drift, RMS}$) that would be measured in a small band of frequencies $f = f_T - \Delta f / 2$ to $f = f_T + \Delta f / 2$ Hz is given by:

$$\Delta T_{Drift, RMS} = \left[\int_{f_T - \Delta f / 2}^{f_T + \Delta f / 2} PSD_{\Delta T, Drift}(f) df \right]^{1/2}. \quad (3-17)$$

This temperature fluctuation is substantially smaller than that in schemes 1 and 2 as the $PSD_{\Delta T, Drift}$ is significantly smaller in the frequency range of interest ($f_T - \Delta f / 2, f_T + \Delta f / 2$). The mean square voltage noise associated with temperature drift, relative to the inputs, in a small band of frequencies ($f_T - \Delta f / 2, f_T + \Delta f / 2$) is given by:

$$\Delta V_{Temperature\ Drift, RTI, S3}^2(f = f_T Hz) = (I_s R \alpha)^2 \int_{f_T - \Delta f / 2}^{f_T + \Delta f / 2} PSD_{\Delta T, Drift}(f) df, \quad (3-18)$$

and the noise equivalent temperature for scheme 3 ($NET_{Scheme\ 3}$) is given by:

$$NET_{Scheme\ 3} = \frac{\left[\Delta V_{Amp\ Total, RTI, S3}^2 + \Delta V_{Temperature\ Drift, RTI, S3}^2 \right]^{1/2}}{I_s R \alpha}. \quad (3-19)$$

Equation (3-19) suggests that the NET of scheme 3 can be very small if the temperature is modulated at high enough frequencies. However, in certain microdevices *e.g.* those used in nanoscale heat transfer studies [24, 28], it is not possible to modulate the temperature at relatively large frequencies, as the suspended devices have thermal cut-off frequencies in the range of 1-10 Hz. The next scheme shows that low NETs can be achieved even in such scenarios by employing a modulated sensing current.

D. Scheme 4: Measurement of modulated temperature changes (ΔT) using a modulated sensing current (I_s)

We now consider the measurement of modulated temperature changes using a modulated sensing current. In this scheme, the voltage signal at the output of the second amplifier is given by:

$$V_{Out} = \underbrace{G_1 G_2 [I_s \sin(2\pi f_s t) R \alpha \Delta T \sin(2\pi f_T t)]}_{V_{Signal}} + \Delta V_{Noise}, \quad (3-20)$$

where I_s is the amplitude of the sensing current and f_T is the frequency of temperature modulation. The voltage signal of interest can now be expressed as:

$$V_{Signal} = \frac{G_1 G_2 I_s R \alpha \Delta T}{2} \left[\cos(2\pi(f_s - f_T)t) - \cos(2\pi(f_s + f_T)t) \right], \quad (3-21)$$

which shows that the voltage signal has contributions at two frequencies, $f_s - f_T$ and $f_s + f_T$, both of which can be chosen to be sufficiently large by choosing the sensing frequency f_s to be large even though the temperature modulation frequency f_T may be small.

In order to obtain the desired signal it is necessary to extract the signal components in the frequency bands centered at $(f_s - f_T)$ and $(f_s + f_T)$ in a width Δf . The mean square voltage noise corresponding to measurements in these bands of frequencies is given by:

$$\Delta V_{Amp\ Total,\ RTI,\ S3}^2 = \int_{f_s - f_T - \Delta f/2}^{f_s - f_T + \Delta f/2} PSD_{Amp\ Total,\ RTI}(f) df + \int_{f_s + f_T - \Delta f/2}^{f_s + f_T + \Delta f/2} PSD_{Amp\ Total,\ RTI}(f) df. \quad (3-22)$$

Further, the overall noise also has contributions from two frequency windows—instead of one in scheme 3. This does not necessarily increase the total noise as the frequency window can be chosen to be centered at large frequencies, even though the modulation frequency f_T is small. The contribution to the voltage noise from relative temperature drift between the *sensing* and *matching* resistance can be estimated from (see Appendix):

$$\Delta V_{Temperature\ Drift,\ Total,\ RTI,\ S4}^2 \sim \frac{(I_s R \alpha)^2}{2} \int_{f_T - \Delta f/2}^{f_T + \Delta f/2} PSD_{\Delta T,\ Drift}(f) df. \quad (3-23)$$

This suggests that the noise equivalent temperature for scheme 4 can be expressed as:

$$NET_{Scheme\ 4} = \frac{\left[\Delta V_{Amp\ Total\ RTI,\ S4}^2 + \Delta V_{Temperature\ Drift,\ RTI,\ S4}^2 \right]^{1/2}}{I_s R \alpha}. \quad (3-24)$$

The discussion presented above shows that it is beneficial to use scheme 4 when measuring temperatures that are sinusoidally modulated at low frequencies.

E. Summary and comparison of the four measurement schemes

The detailed discussion presented above lays out the limitations and requirements for achieving high-resolution resistive thermometry. The resolution of resistive thermometry is

improved significantly by (1) employing a matching resistor which helps in isolating the signal of interest and rejecting the common mode noise originating from both environmental thermal drift and noise in the sensing current, (2) adopting a modulation scheme that enables measurements at frequencies where the power spectral density of noise is small, and (3) choosing a large sensing current as well as a PRT with a large electrical resistance: parameters which cannot be increased to arbitrarily large values in most micro and nanoscale applications due to self-heating effects and limitation of the device foot print.

It was shown that the resolution of resistive thermometry in scheme 1, measurement of unmodulated temperatures using an unmodulated sensing current, is relatively poor as the large $1/f$ noise (from both voltage noise and temperature drift) results in a large noise signal. The limitations of scheme 1 are partly eliminated in scheme 2 where unmodulated temperatures are measured using modulated sensing currents. In this scheme, the NET is significantly improved as the measurements are made at a relatively high frequency where the contribution of $1/f$ voltage noise is negligible. However, this scheme is still susceptible to noise arising from low-frequency ambient temperature drift limiting the resolution. The noise associated with ambient temperature drift is eliminated if the temperature to be detected is modulated at a relatively high frequency. Specifically, our discussion highlighted the fact that modulated temperatures can be measured using unmodulated electrical current at high resolution (scheme 3). However, if the modulation frequency of the temperature is low, scheme 3 is affected by electrical $1/f$ noise. In order to overcome this challenge, we described a scenario (scheme 4) where a modulated sensing current can be used to detect low frequency temperature modulations. Such a scheme enables measurement at high frequencies attenuating the effect of both $1/f$ noise and temperature drift. However, in implementing such a scheme one has to contend with noise in two spectral windows as the signal is split into two sidebands.

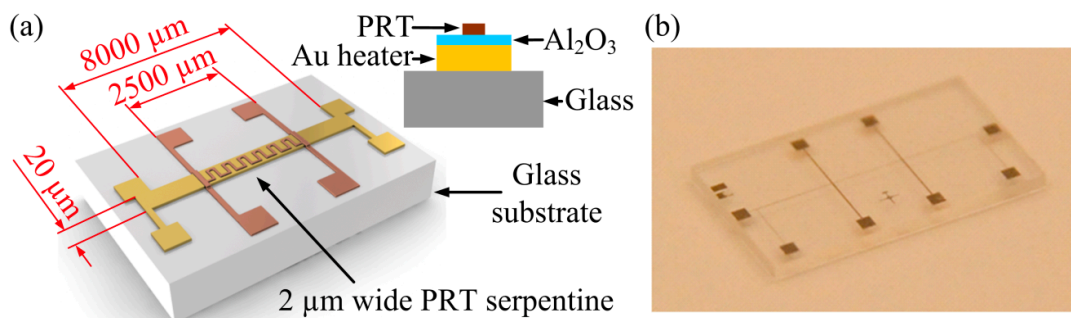


Figure 3-3- Microdevice used in this work. (a) Schematic diagram of the test device (not drawn to scale). A micro-heater line (Au heater) patterned on a glass substrate is used to generate temperature modulations. The top PRT is patterned on top of a micro-heater line and separated by a thin Al_2O_3 layer (see cross section) to electrically isolate it from the heater while maintaining it in excellent thermal contact with the heater. Note that the Al_2O_3 layer is not shown in the schematic in order to facilitate a clear view of the heater line. (b) Optical image of the microfabricated test device.

3-5- Approach for experimental characterization of the noise equivalent temperature (NET) of temperature measurement schemes

In order to experimentally test the NET of the schemes described above it is desirable to fabricate devices that have both an electrical heater and an electrical resistance thermometer in excellent thermal contact with each other. In such a device, the electrical heater can be used for generating temperature changes, while the thermometer can be used to measure the temperature oscillations. We accomplished this goal by microfabricating devices with an integrated heater and thermometer (Figure 3-3). The device, fabricated on a glass substrate, features a $8000 \mu\text{m}$ long, $20 \mu\text{m}$ wide, and 100 nm thick Au electrical heater line which is patterned in a four probe configuration using a lift-off process. Further, a 40 nm thick aluminum oxide (Al_2O_3) film is deposited using atomic layer deposition on the heater line. Finally, a serpentine shaped platinum thin film (see Figure 3-3), which is $\sim 2 \mu\text{m}$ wide and $\sim 35 \text{ nm}$ thick and shaped into a four-probe pattern, is deposited on the Al_2O_3 film using a lift-off process. We note that the thin Al_2O_3 film serves to electrically isolate the Au and Pt lines,

from each other, while maintaining them in excellent thermal contact. We choose the length of the serpentine line such that the resultant electrical resistance of the PRT is $\sim 10\text{ K}\Omega$. This choice represents a compromise between high temperature resolution and the feasibility of integrating PRTs with a resistance of 1-10 $\text{K}\Omega$ into microdevices, including suspended devices used in nanoscale heat transport studies[24]. Thus the improvements described in this work can be readily utilized for enhancing the resolution of thermometry used in nanoscale heat transfer studies.

The strategy adopted in this work to characterize the NET of the four schemes is conceptually simple. The microfabricated device is placed in a cryostat (in a vacuum of $\sim 10^{-3}$ Torr) and an electrical current (modulated or unmodulated) is supplied to the heater. When a sinusoidal electrical current with a frequency f_H is applied to the heater line it results in temperature oscillations of the heater line at $2f_H = f_T$. The serpentine PRT sensor fluctuates at exactly the same temperature as it is in excellent thermal contact with the heating line through a thermally highly conductive 40 nm thick Al_2O_3 layer. This can be understood by noting that the thermal coupling between the PRT line and the external environment, through radiation and by conduction through the air molecules, is negligible in comparison with the thermal coupling with the heater line. We now describe in detail our experimental approach.

The first step in characterizing the microfabricated heater and the PRT is to characterize the temperature coefficient of resistance (TCR) of the Au (heater) and Pt (thermometer) thin films. We measured the TCR by systematically varying the temperature of the cryostat from 80 K to 320 K while monitoring the electrical resistance of the heater and the PRT in a four probe configuration. To elaborate, a sinusoidal current of amplitude $I_{AC} = 10\ \mu\text{A}$ and frequency $f_s = 100\text{ Hz}$ was passed through the PRT and the amplitude of the resultant voltage oscillations at 100 Hz ($V_{100\text{Hz}}$), across the serpentine region, was measured using a lock-in amplifier (SR830, Stanford Research Systems) to obtain the resistance ($R = V_{100\text{Hz}} / I_{AC}$).

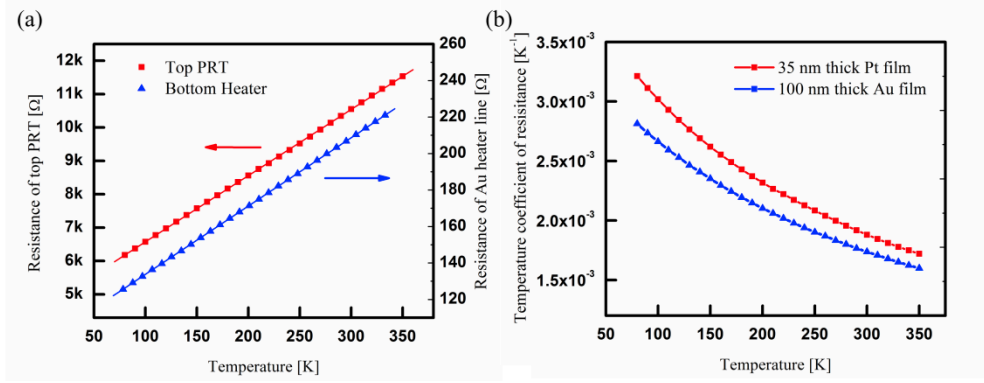


Figure 3-4- Characterization of the temperature dependence of resistance. a) The measured resistance vs. temperature for the PRT and heater lines: red arrow points to the resistance of the PRT whereas the blue arrow points to the resistance of the heater. (b) The obtained TCR values for the 35 nm thick PRT (Pt film) and 100 nm thick heater (Au film) line.

A similar approach was used to measure the temperature dependent resistance of the heater line. Figure 3-4a shows the measured resistance vs. temperature from which the temperature dependent TCRs were calculated (Figure 3-4b). The measured TCR values are in good agreement with published data for the TCR of Au and Pt thin films of comparable thickness [24, 27].

To show that the heater and thermometer are in excellent thermal contact and experience identical temperature changes, we adopt the configuration shown in Figure 3-5. When a sinusoidal heating current $I(t) = I_H \sin(2\pi f_H t)$ generated using a commercially available current source (Keithley-6221), is supplied to the heater its temperature oscillates sinusoidally at a frequency $2f_H$ due to joule heating (f_H was set to 20 Hz in this experiment). Further, the voltage across the probe electrodes (labeled 3 and 4 in Figure 3-5) also has a component at $3f_H$, which results from the interaction of the sinusoidal sensing current at f_H and the PRT whose temperature is oscillating sinusoidally at $2f_H$. The RMS value of the sinusoidal temperature oscillation at $2f_H$ (ΔT_{2f_H}) can be related to the RMS value of voltage oscillation at $3f_H$ (V_{3f_H}) by $\Delta T_{2f_H} = 2V_{3f_H} / (I_H R \alpha)$.

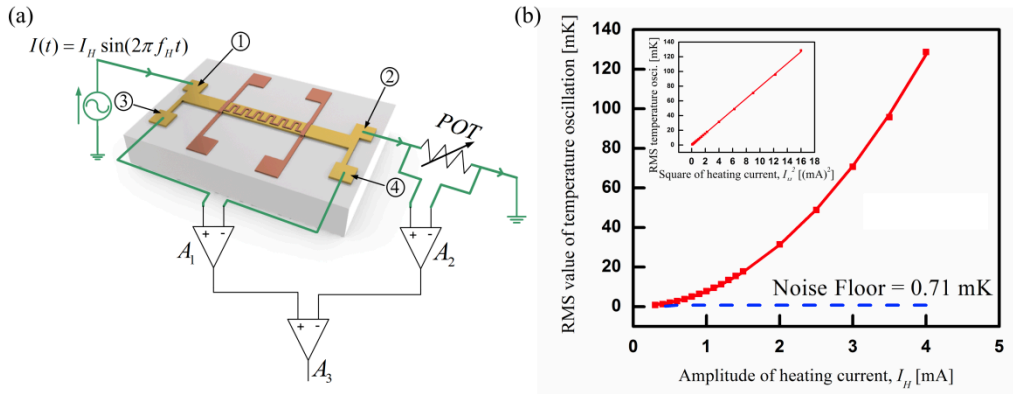


Figure 3-5- Characterization of the relationship between the RMS value of temperature oscillations and the amplitude of the heating current. (a) Schematic diagram of the measurement configuration used to measure the RMS values of temperature oscillations of the heater line. A potentiometer is placed in series to implement a differential scheme that enables the isolation of the $3f_H$ component of the voltage signal. (b) Measured RMS values of the temperature oscillation of the bottom heater line as a function of the amplitude of the heating electrical current. The frequency of the heating current is chosen to be 20 Hz. Inset shows the same data plotted as a function of square of the amplitude of the heating current, the relationship is linear as expected (the R-square measure of goodness of fit is 0.999).

In addition to the signal at $3f_H$, the voltage signal across the probe electrodes also has a large component at frequency f_H . In order to extract the voltage component of interest at $3f_H$, we placed a bulk potentiometer (see Figure 3-5a) in series with the bottom heater. Since the bulk potentiometer has a large thermal mass its amplitude of temperature oscillation at $2f_H$ is negligible. Thus the voltage drop across the potentiometer primarily has a component at the frequency f_H , which can be made identical to the component across the heater by appropriately tuning the resistance of the potentiometer. The voltage output across the bottom heater and that across the potentiometer are first measured using two precision instrumentation amplifiers (A1, A2, Analog Devices - AD524, with gain of 10). The voltage output of these amplifiers was supplied to another instrumentation amplifier (A3, Analog Devices -AD524), with unity gain. This enabled us to subtract the voltage component at a frequency f_H . The voltage output of this instrumentation amplifier was supplied to a lock-in amplifier (SRS-SR830) to measure the RMS value of voltage oscillations at $3f_H$.

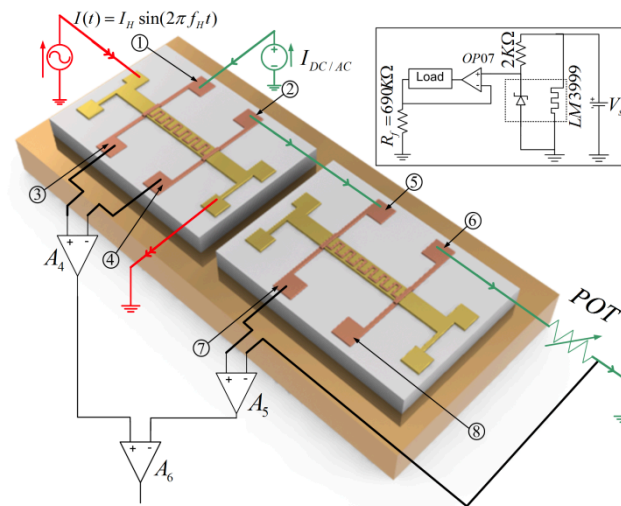


Figure 3-6- Schematic diagram of the instrumentation setup used to measure the amplitude of temperature oscillations of the PRT. A differential measurement scheme is used to reject the noise arising from the non-ideality of the current source and to eliminate the effects of thermal drift. Inset: schematic diagram of the custom-built current source.

Finally, the RMS value of the temperature oscillations is related to the RMS value of the voltage oscillations. The measured RMS values of temperature oscillations for various amplitudes of sinusoidal electrical currents ($f_H = 20$ Hz,) are shown in Figure 3-5b.

Noise floor of the $3f$ -technique: The $3f$ -measurement technique described above uses the same electrical current to both induce a temperature oscillation via heating as well as for sensing the temperature oscillations. This implies that when the amplitude of temperature oscillations is small, the amplitude of the heating (sensing) electric current is also low.

This lack of independent control on the sensing and heating currents limits the ability to measure temperature oscillations of small amplitudes because the voltage output at $3f_H$ is directly proportional to the amplitude of the sensing current. Hence, the noise floor in the measurement of temperature oscillations is relatively high. For example, the noise floor in our measurements is ~ 1 mK and is shown by the dashed line in Figure 3-5b. The measured temperature oscillation is also plotted as a function of I_H^2 in Figure 3-5b inset. Indeed, we find that the measured temperature oscillations increase linearly with I_H^2 .

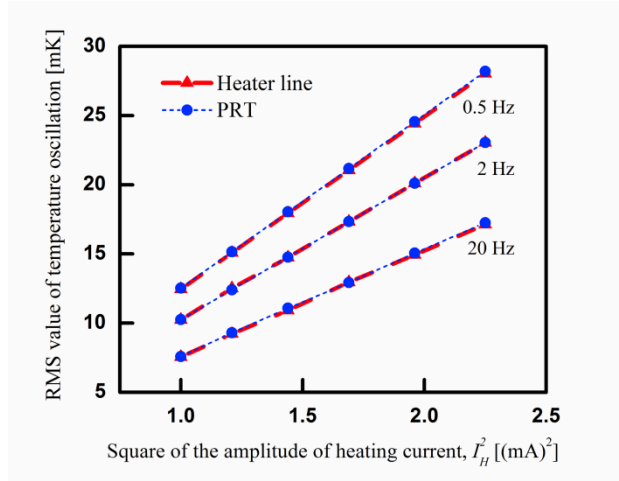


Figure 3-7- Characterization of the thermal contact between the heater line and the PRT. The measured RMS values of the temperature oscillations of the heater and the PRT, due to a sinusoidal thermal excitation of the heater line. The RMS values increase linearly with the magnitude of the square of the amplitude of the heating current. Further, the bottom and top line temperatures are identical. This provides strong support for the conclusion that the heater and PRT are in excellent thermal contact. The measurements were performed over a range of heating frequencies ($2f_H = 0.5 \text{ Hz}$, 2 Hz , and 20 Hz).

Measurement of temperature oscillations with the platinum resistance thermometer: In order to independently measure the temperature oscillations in the PRT resistor resulting from the heating of the bottom heater, we adopted the measurement configuration shown in Figure 3-6. A DC current, $I_{DC} = 10 \text{ } \mu\text{A}$, generated using a custom built current source (see Figure 3-6 inset) was supplied through the PRT.

In addition to a DC component, the voltage across the probe electrodes (3, 4 in Figure 3-6) also has a component at $2f_H$, arising from the interaction of the DC current and the temperature-dependent electrical resistance. In fact, the RMS value of the sinusoidal temperature oscillation of the PRT (ΔT_{2f_H}) can be related to the RMS value of the voltage oscillation V_{2f_H} by $\Delta T_{2f_H} = V_{2f_H} / [I_{DC} R \alpha]$.

In order to isolate the signal of interest (V_{2f_H}) from the large DC voltage across the resistor, we placed an identical thin film resistor (matching resistor) in series with the PRT

(Figure 3-6), which was also located inside the cryostat. Thus both resistors experience nearly identical ambient temperature and thermal drifts. Further, a potentiometer was used in series with the thin-film resistors (located outside the cryostat) to trim the DC voltage across the PRT and matching resistor to be equal (see Figure 3-6). The voltage signals across the PRT and across the matching thin film resistor and the potentiometer are measured with two precision instrumentation amplifiers (A4, A5, Analog Devices-AD524) operated at a gain of 100. The differential temperature signal from these outputs was obtained using a second stage monolithic low noise amplifier (A6) with a wideband, low distortion and high common mode rejection ratio (Burr-Brown-INA103). Finally, the voltage output of this instrumentation amplifier was supplied to a lock-in amplifier (SRS-SR830) to measure the RMS value of the voltage oscillations at $2f_H$. The measured RMS values were used to obtain the RMS values of the temperature oscillations. Figure 3-7 shows the measured RMS values of temperature oscillations of the PRT line along with the measured RMS values of the heater line for various frequencies and amplitudes of temperature oscillations. The data suggests that the RMS values of the temperature oscillations in the bottom and top heaters are identical for the entire range of heating currents—demonstrating that the PRT and the heater lines are in excellent thermal contact. We note that increasing frequencies of heating current lead to progressively smaller temperature oscillations, such dependence on frequency is indeed expected and well understood from basic heat transfer theory [44].

Finally, we emphasize that all the measurements of the temperature oscillations shown in Figure 3-7 were performed for a range of heating currents that produce temperature oscillations that are above the noise floor of the $3f$ technique, so as to enable a direct measurement of the temperature oscillations of both the heater and the PRT.

3-6- Power spectral density of noise

In order to enable an estimation the NET of each of the schemes described above it is necessary to experimentally determine $PSD_{Amp\ Total, RTI}$ and $PSD_{\Delta T, Drift}$. In this section, we present our experimentally measured data of these power spectral densities. Further, we also provide the estimated temperature resolution for each of the schemes described above.

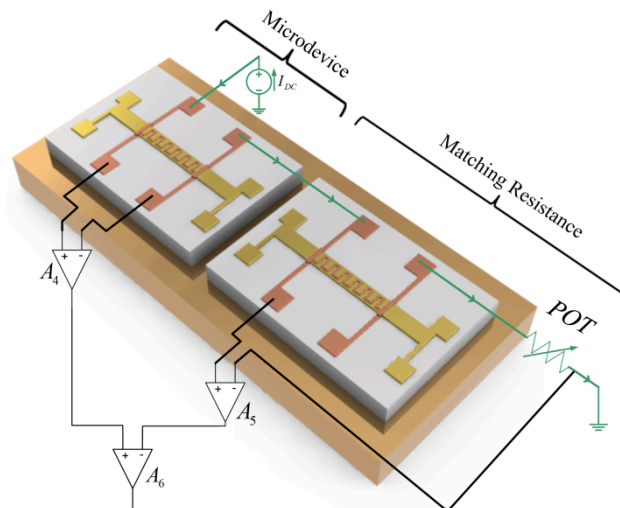


Figure 3-8- Schematic diagram of the measurement setup to obtain the power spectral densities $PSD_{Amp\ total, RTI}$ and $PSD_{\Delta T, drift}$. These PSDs are required to estimate the NET of the each of the four schemes described in this study.

A. Characterization of Power Spectral Densities ($PSD_{Amp\ Total, RTI}$ and $PSD_{\Delta T, Drift}$)

The general strategy used in this work to obtain the desired power spectral densities is as follows. We begin by configuring a setup represented by the schematic shown in Figure 3-8. First, an unmodulated current $I_s = I_{DC}$, from a custom-built current source (Figure 3-6 inset) is supplied through the PRT of the microdevice and a matching resistor (identical resistance thin film device and potentiometer, see Figure 3-8) while the heating current was turned off. The voltage output of the second stage amplifier, which measures the differential voltage between the voltage drop across the microdevice and the voltage drop across the matching resistor was monitored to characterize the noise. It is to be expected that the voltage noise has

contributions from various noise sources including shot noise and temperature drift. The contributions of various noise sources to the power spectral density of the voltage noise at the output ($PSD_{with I_s=I_{DC}}$) can be estimated using Equation (3-5) for any given magnitude of the sensing current. When the supplied current I_s is turned off, the resultant power spectral density ($PSD_{with I_s=0Amp}$) is smaller, at all frequencies, as the contributions from shot noise and temperature drift are eliminated. We note that $PSD_{with I_s=I_{DC}}$ can be related to $PSD_{Amp Total}$ (see Eq. (3-5)) and $PSD_{\Delta T, Drift}(f)$ by $PSD_{with I_s=I_{DC}}(f) = PSD_{Amp total} + \left[(I_{DC} R \alpha)^2 PSD_{\Delta T, Drift}(f) \right] G_1^2 G_2^2$

Using this equation and Eqs. (3-2) and (3-5), it can be shown that:

$$PSD_{with I_s=I_{DC}}(f) - PSD_{with I_s=0 Amp}(f) = \left[(I_{DC} R \alpha)^2 PSD_{\Delta T, Drift}(f) + 2 PSD_{I=I_{DC}, Shot}(f) R^2 \right] G_1^2 G_2^2 \quad (3-25)$$

This suggests that by measuring the power spectral densities of voltage output with and without a current, it is possible to experimentally obtain a linear combination of the power spectral densities of temperature drift and shot noise (RHS of Eq. (3-25)) We also note that the power spectral density of temperature drift ($PSD_{\Delta T, Drift}(f)$) at high frequencies (>500 Hz) is negligible, as the temperature cannot fluctuate significantly at high frequencies due to thermal inertia. Thus, at high frequencies, the right hand side of Eq. 3-25 consists primarily of contributions from shot noise, hence $PSD_{I=I_{DC}, Shot}(f)$ can be easily obtained at high frequencies. Further, since $PSD_{I=I_{DC}, Shot}(f)$ is expected to be relatively independent of frequency, the obtained high frequency $PSD_{I=I_{DC}, Shot}$ is representative of the shot noise at all frequencies. The discussion above highlights the fact that $PSD_{\Delta T, Drift}(f)$ can be experimentally determined by measuring $PSD_{with I_s=I_{DC}}$ and $PSD_{with I_s=0Amp}$. Finally, ($PSD_{Amp Total, RTI}$) can also be obtained by adding the contribution of shot noise to $PSD_{with I_s=0Amp}$. Specifically, ($PSD_{Amp Total, RTI}$) is given by:

$$PSD_{Amp\ Total, RTI}(f) = \left[(PSD_{with, I_s=0}(f)) / (G_1 G_2)^2 \right] + \left[2PSD_{I=I_{DC}, Shot}(f) R^2 \right] \quad (3-26)$$

In order to experimentally determine $PSD_{with I_s=I_{DC}}$ and $PSD_{with I_s=0Amp}$ we used the configuration shown in Figure 3-8. In this experiment, we first applied a DC sensing current of 10 μ A to the PRT, which was found to be adequate for estimating the desired power spectral densities. The voltage output of the second stage amplifier (Figure 3-8) was simultaneously monitored to obtain the power spectral density a commercial FFT analyzer (SR 770, Stanford Research Systems). Precautions were taken to eliminate extraneous sources of noise by carefully shielding all the wires and the devices from stray electromagnetic fields: the cryostat chamber used in the experiment was grounded and the low level, differential signals were collected with cables employing individually shielded and twisted pairs. Further, special care was taken to avoid ground loops [45].

Figure 3-9 (a) shows the measured power spectral densities (at 280 K) of $PSD_{with I_s=I_{DC}}$ and $PSD_{with I_s=0Amp}$ relative to the inputs (i.e. measured power spectral density divided by $G_1^2 G_2^2$). As expected, $PSD_{with I_s=I_{DC}}$ is greater than $PSD_{with I_s=0Amp}$ at high frequencies (500 Hz - 3 KHz), and the difference is relatively invariant with frequency. The measured difference suggests that $2PSD_{I=I_{DC}, Shot}(f) \cdot R^2$ is ~ 75 nV²/Hz, in the range from 500 Hz – 3 KHz, which is much smaller than the power spectral density estimated from the equation for shot noise described earlier (estimated shot noise equals $2(2eI_s R^2) \sim 6400$ nV²/Hz). We note that this smaller shot noise value is to be expected because the custom-built current source (Figure 3-6 inset) used in our experiments employs negative feedback which is well known to suppress shot noise[46]. Further, the long range electronic correlations in metallic conductors are also known to suppress shot noise [46].

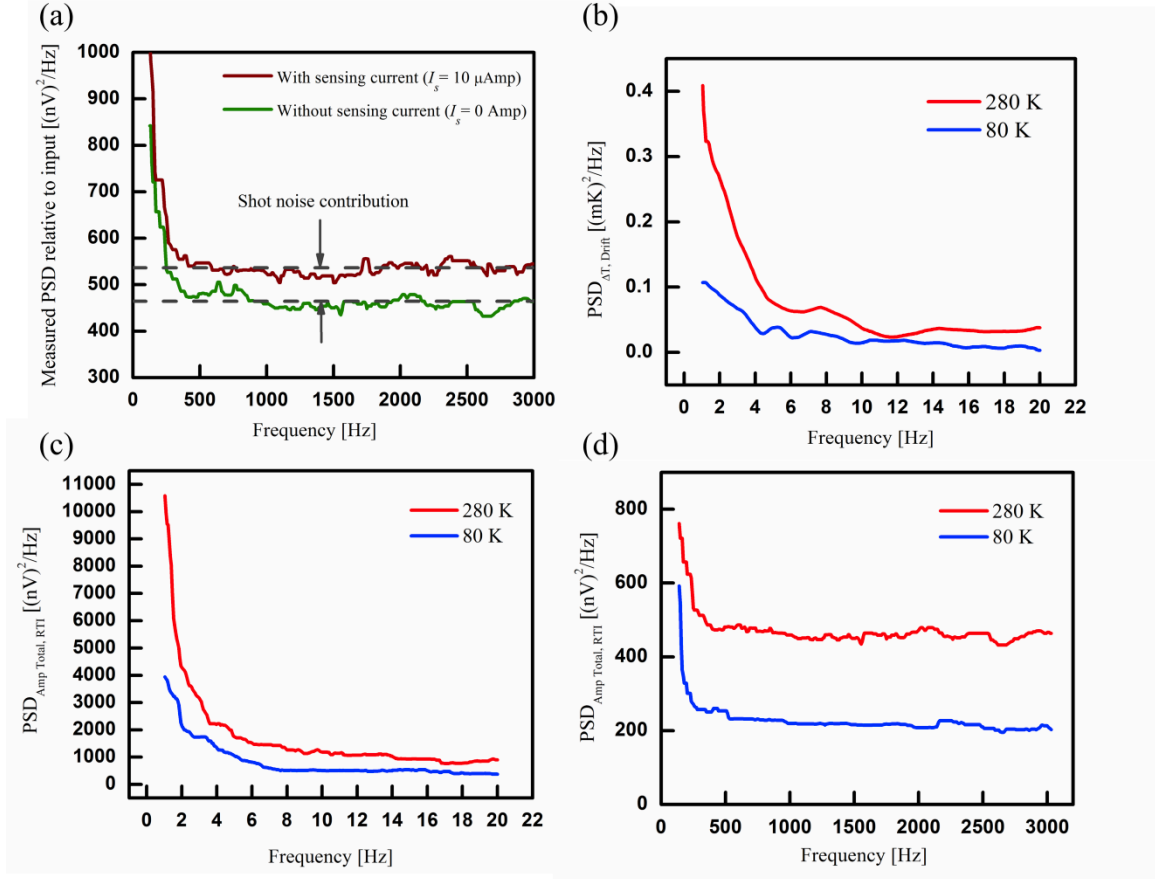


Figure 3-9- Experimental determination of $PSD_{Amp\ total, RTI}$ and $PSD_{\Delta T, Drift}$. Panel (a) shows the measured power spectral densities (at 280 K) of $PSD_{with\ I_s=I_{DC}}$ and $PSD_{with\ I_s=0\ Amp}$ relative to the inputs (i.e. measured power spectral density divided by $G_1^2 G_2^2$). The larger power spectral density of $PSD_{with\ I_s=I_{DC}}$, at high-frequencies, is attributed to shot noise as discussed in the text. The shot noise contribution is seen to be relatively independent of the frequency (b) $PSD_{\Delta T, Drift}$ for a range of frequencies (1 – 20 Hz), at two different temperatures (80 K, 280 K) was obtained by first measuring $PSD_{with\ I_s=I_{DC}}$ and $PSD_{with\ I_s=0\ Amp}$ in the frequency range of interest and using Eq. 25 described in the text. (c) Measured $PSD_{Amp\ total, RTI}$ of thermometer at 80 K and 280 K in a range of frequencies (1-20 Hz), and (d) Measured $PSD_{Amp\ total, RTI}$ of thermometer at 80 K and 280 K in a larger range of frequencies (1 Hz - 3 kHz). The data presented in the figure was obtained by first averaging the measured PSD in 200 individual experiments (Fig. 9a, d) and 20 individual experiments (Fig. 9b, c) and subsequently performing further averaging using a 20 point median averaging scheme.

Using the measured power spectral density of shot noise in conjunction with Eq. (3-25), we obtained the $(PSD_{\Delta T, Drift})$ at 280 K which is shown in Figure 3-9b for the frequency ranges 1 – 20 Hz. Following a similar procedure, we also obtained $(PSD_{\Delta T, Drift})$ at 80 K, which is also shown in Figure 3-9b. It can be seen that the low-frequency part of the spectrum is dominated by $1/f$ noise, while the high-frequency part of the spectrum shows broadband noise that is relatively independent of frequency. In addition to this, we also obtained $(PSD_{Amp Total, RTI})$ using the measured data and Eq. (3-26). The obtained power spectral densities are shown in Figure 3-9c (1 Hz -20 Hz) and Figure 3-9d (1 Hz – 3 KHz) for a range of frequencies. This data was obtained by first averaging the measured PSD from 200 individual experiments for Figure 3-9a, d and 20 individual experiments for Figure 3-9b, c and subsequently performed twenty point median averaging to obtain smooth spectral density estimates.

Finally, to estimate the NETs in scheme 1 and 2, as well as for estimating NETs for low frequency temperature modulations (0.5 Hz) in scheme 3 and 4, it is necessary to know the values of $PSD_{\Delta T, Drift}$ in a range of frequencies close to 0 Hz. Therefore, we obtained $PSD_{with I_S=I_{DC}}(f)$ and $PSD_{with I_S=0 Amp}(f)$ in a narrow band of $f = 0$ to 1 Hz in frequency intervals of $\Delta f = 0.477$ mHz (Figure 3-10a). The obtained power spectral densities of $PSD_{Amp Total, RTI}$ and $PSD_{\Delta T, Drift}$ are shown in Figure 3-10b and c, respectively. The curves shown in Figure 3-10a were obtained by averaging five individual spectral density estimates and by curve-fitting a ninth order polynomial function to the data. Further, 95% confidence intervals of the curve fits were determined to estimate the uncertainty in the measured PSD (see inset Figure 3-10a). The PSD of the total amplifier noise and temperature drift were obtained by using the data presented in Figure 3-10a and are shown in Figure 3-10b and 10c. Both the estimates shown in Figure 3-10b and 10c have a small uncertainty (not shown in the figure) that arises from the uncertainty in the fits to the data presented in Figure 3-10a.

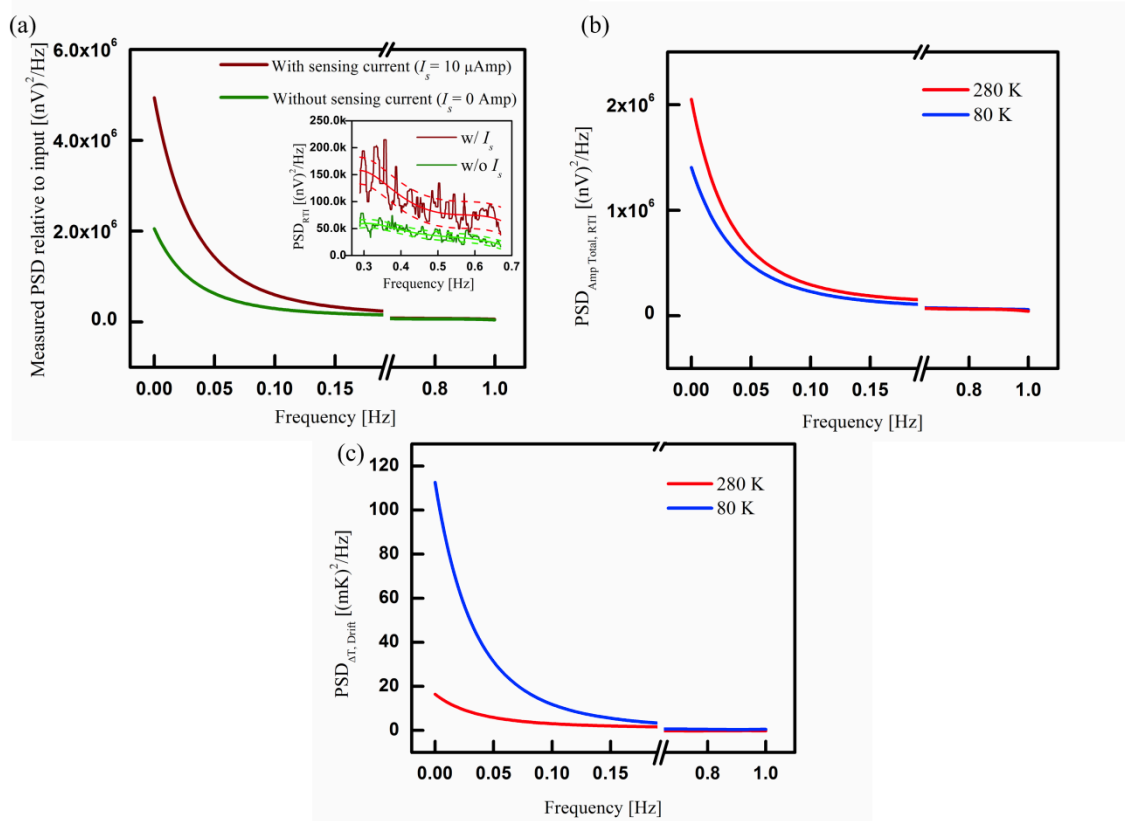


Figure 3-10- Measurement of amplifier noise and temperature drift at low frequencies. We determined the $PSD_{Amp\ total, RTI}$ (b) and $PSD_{\Delta T, Drift}$ (c) in the narrow frequency range of 0 to 1 Hz from the $PSD_{with\ I_s=I_{DC}}$ (f) and $PSD_{with\ I_s=0\ Amp}$ (f) shown in (a) by averaging five individual curves and by curve fitting the averaged data. The data shown in panels (b) and (c) were obtained by using the data presented in panel (a). As a representative example, the inset of Fig. 10a shows the measured PSD at 0.5 Hz along with the curve fits and the corresponding 95% confidence intervals.

B. Estimated NET for the Thermometry Schemes

The measured PSDs enable an estimate of the NET for each of the schemes described above by using the expressions provided in section (3-4). For all the estimates provided below we arbitrarily assume a measurement bandwidth of ~ 16 mHz. Further, we assume that the sensing current used in all the experiments is either a DC current of $10\ \mu A$ or an AC current with an amplitude of $10\ \mu A$. This choice of the magnitude of the current corresponds well to currents used in suspended-microscale devices that are employed for probing nanoscale heat transfer [24]. We note that the chosen magnitude represents a tradeoff between choosing a large magnitude of current to improve the signal to noise ratio while keeping the current small to avoid self-heating effects in suspended devices.

Table 3-2 lists the calculated NETs for the four schemes along with the uncertainty in the NETs estimated using the curve fits and confidence intervals to the measured data. These

NETs were computed at two different temperatures (80 K and 280 K) by using Eqs. (3-10), (3-14), (3-19) and (3-24) and the data presented Figure 3-9 and Figure 3-10. As expected, it can be seen that the NET for scheme 1 is relatively large, ~ 1.5 mK even at low temperatures. This large NET is associated with the large values of $PSD_{Amp\ Total, RTI}$ and $PSD_{\Delta T, Drift}$ at low frequencies. For scheme 2, the NET is found to be ~ 0.7 mK at 280 K and ~ 0.3 mK at 80 K and is relatively independent of the sensing frequency. This lack of dependence on sensing frequency—in this case—can be understood by noting that the NET has large contributions from $PSD_{\Delta T, Drift}$ which is independent of the sensing frequency (20 Hz, 500 Hz, 1000 Hz) as can be seen from Eqs. (3-13) and (3-14). This NET can potentially be improved if the sensing and matching resistors are integrated into a substrate with a high thermal conductivity. For comparison, Wingert *et al.* [27, 35] have recently shown that for samples made on a silicon substrate, with a thermal conductivity ~ 100 times larger than that of the glass substrates used in this study, it was possible to achieve a resolution of ~ 0.6 mK in a bandwidth of ~ 260 mHz (as opposed to the ~ 16 mHz bandwidth used in this study).

This improved resolution can potentially be attributed to smaller $PSD_{\Delta T, Drift}$ in their devices. However, it is not always possible to use such highly thermally conducting substrates, therefore, it is important to quantify the effect of $PSD_{\Delta T, Drift}$. Additional improvements in the NET could potentially be obtained, for both scheme 1 and 2, by carefully attenuating the temperature drift of the electronics to small values (\sim mK): this would enable a reduction in the low frequency voltage noise.

Table 3-2- The estimated resolution of the four different schemes of resistance thermometry. The resistance of the PRT is assumed to be 10 k Ω while the bandwidth of measurement is set to 16 mHz.

	Global temperature (K)	Thermometry resolution (μK)		
<i>Scheme 1</i>	280	2463 ± 316		
$f_s = 0$ $f_T = 0$	80	1573 ± 172		
<i>Scheme 2</i>		$f_s = 20$ Hz	$f_s = 500$ Hz	$f_s = 1000$ Hz
$f_s \neq 0$ $f_T = 0$	280	702 ± 15	702 ± 15	702 ± 15
	80	271 ± 14	270 ± 14	270 ± 14
<i>Scheme 3</i>		$f_T = 0.5$ Hz	$f_T = 2$ Hz	$f_T = 20$ Hz
$f_s = 0$ $f_T \neq 0$	280	212 ± 31	78 ± 21	34 ± 17
	80	181 ± 11	53 ± 20	27 ± 18
<i>Scheme 4</i>		$f_T = 0.5$ Hz	$f_T = 2$ Hz	$f_T = 20$ Hz
$f_s = 500$ Hz $f_T \neq 0$	280	81 ± 43	48 ± 12	30 ± 8
	80	43 ± 27	32 ± 12	23 ± 9

For scheme 3, where the temperature changes to be measured are modulated, the NET is found to be substantially smaller ($<100 \mu\text{K}$) for large modulation frequencies (2 Hz, 20 Hz). This improvement in NET arises primarily from a reduction in both $PSD_{Amp\ Total, RTI}$, and $PSD_{\Delta T, Drift}$ at high frequencies. Finally, for scheme 4, we estimated the resolution for a sensing current frequency of 500 Hz and for various temperature modulation frequencies. It can be seen that, as expected, at low modulation frequencies the NET can be improved by approximately a factor of three in comparison to scheme 3. On the other hand, at higher frequencies (2 Hz, 20 Hz) the estimated NET of scheme 4 is comparable to that of scheme 3.

A final question to be addressed is if the predicted NETs can actually be achieved with a commercial lock-in amplifier (SRS-SR830) which enables convenient, continuous monitoring of temperature signals. To answer this question we experimentally implemented schemes 3 and 4. We focused on these schemes because of their superior resolution and the fact that a variation of scheme 2 has been recently discussed in the literature [27, 35].

3-7- Experimental verification of the NET for Schemes 3 and 4

In order to experimentally measure the NET of the PRT in schemes 3 and 4 we supplied sinusoidal electrical currents with relatively small amplitudes to the PRT, which resulted in temperature oscillations of the PRT with small RMS values. We note that based on the data shown in Figure 3-7 (data obtained at 280 K) and similar data obtained at 80 K it is possible to estimate the expected RMS values of temperature oscillations for currents of small amplitudes. In fact, the dashed lines in Figure 3-11 and 3-12 show estimated temperature raises at 280 K and 80 K, for sinusoidal excitation by currents of small amplitudes at various frequencies. We now describe the experiments performed by us to experimentally establish the resolution of schemes 3 and 4.

A. Measured RMS values of temperature modulations in scheme 3:

Temperature oscillations of the PRT, resulting from sinusoidal heating currents of small amplitudes, were measured by supplying a DC sensing current ($I_{DC} = 10^{-5}$ amp) and monitoring the $2f_H$ component of the voltage (V_{2f_H}) using a commercial lock-in amplifier, in a bandwidth of ~ 16 mHz, following the configuration shown in Figure 3-6. The RMS values of the resultant temperature oscillations (ΔT_{2f_H}), arising from heating currents of varying amplitudes and frequencies (0.5 Hz, 2 Hz, and 20 Hz), were obtained from the measured voltage oscillations using the relationship $\Delta T_{2f_H} = V_{2f_H} / (I_{DC} R \alpha)$ and are shown in Figure 3-11a. Further, the expected values of temperature oscillations from the data shown in Figure 3-7 are also plotted (dashed lines) along with the expected NETs and their corresponding uncertainties (from Table 3-2), which are represented by solid lines and solid bands respectively. It can be seen that the measured temperature oscillations are in good agreement with the expected values (dashed lines).

Further, it can also be seen that the smallest temperature that could be measured is in good agreement with the expected NET values. Figure 3-11b shows otherwise identical data obtained at a temperature of 80 K. Again, it can be seen that the smallest temperature that could be resolved at various frequencies is in good agreement with estimated values of NET. Experiments performed at other temperatures (130 K, 180 K, 230 K) are also found to be in good agreement with estimated NETs and are not presented here in the interest of space. Finally, we note that, as expected, the NET at low frequencies (0.5 Hz) is significantly larger than that at high frequencies due to contributions from $1/f$ voltage noise. Next, we show that the temperature resolution of low frequency measurements can be improved substantially using a modulated sensing current.

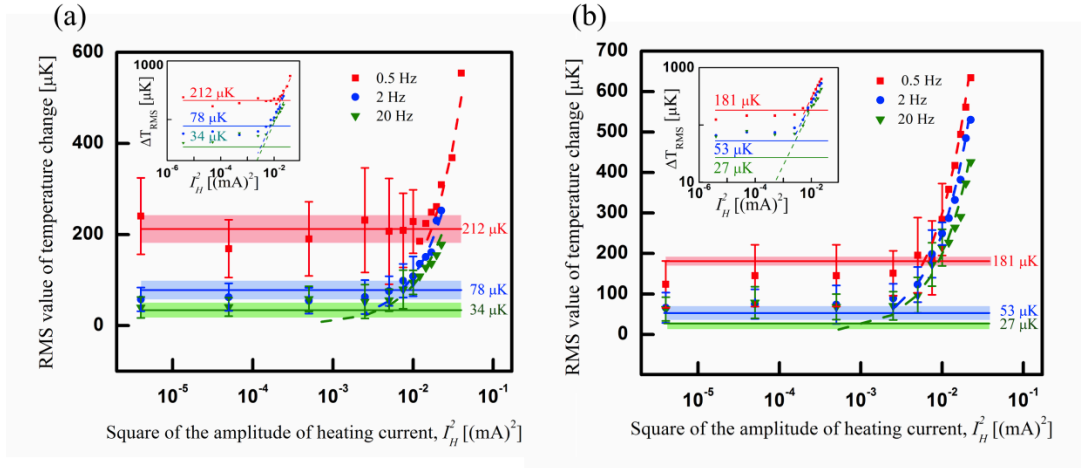


Figure 3-11- Experimental demonstration of the resolution of scheme 3. In this scheme modulated temperature changes are detected using an unmodulated sensing current. Part (a) shows the measured RMS values of the temperature oscillations of the PRT, at an ambient temperature of 280 K, when the heater line is excited using sinusoidal heating currents (0.5, 2.0, and 20 Hz). The dashed lines in the figure, represent the expected RMS temperature values based on data shown in Fig. 7. The error bars above reflect the standard deviation in the RMS value reported by the lock-in amplifier. The solid lines show the estimated noise floor for NET measurements performed at each of the frequencies, while the bands represent the uncertainty of the NET estimates. The inset presents the same data in a log-log plot. Figure (b) shows data otherwise identical to those in (a) for measurements performed at 80 K.

B. Measured RMS values of temperature modulations in scheme 4:

We performed an experiment (at 280 K) where temperature oscillations of the PRT at f_T (0.5 Hz) were measured using an AC sensing current with an amplitude $I_{AC} = 10^{-5}$ amp and a sensing frequency $f_S = 500$ Hz. The measurement configuration used for accomplishing this goal is shown in Figure 3-6. As described in section 3-5-, the voltage output of the second stage amplifier has information regarding the temperature oscillation of the PRT at two frequencies: $f_S + f_T$ and $f_S - f_T$. In order to extract these signals, we monitored the voltage output of the second stage amplifier using two lock-in amplifiers, set to a bandwidth of ~ 16 mHz, to independently measure the components of the signal at $f_S + f_T$ and $f_S - f_T$. In order to provide the appropriate reference signal to the lock-in amplifiers we used four function generators (Agilent 33521A) that were synchronized using a master clock.

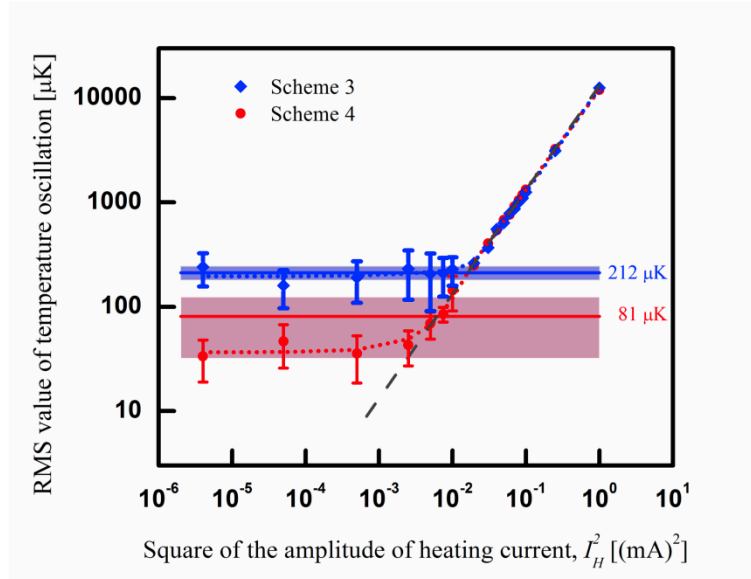


Figure 3-12- Experimental demonstration of the resolution of scheme 4 at low modulation frequencies (0.5 Hz). Modulated temperature changes were measured using a modulated sensing current at 500 Hz. All measurements were performed at 280K. The dashed line represents the expected temperature RMS values based on the data shown in Fig. 7. The dotted lines show curve fits to the measured data. The error bars above reflect the standard deviation in the RMS value reported by the lock-in amplifier. The solid lines and bands show the estimated NETs and the uncertainty in the estimated NETs respectively.

Two of these function generators in conjunction with the custom built current source (a modified version of the circuit shown in the inset of Figure 3-6) were used to generate the desired heating and sensing sinusoidal currents at the appropriate frequencies, f_T and f_S respectively. The remaining two function generators provided the reference signals required by the lock-in amplifiers to extract the voltage signals of interest at $f_S - f_T$ and $f_S + f_T$. The RMS values of the voltages measured by two lock-in amplifiers ($V_{f_S+f_T}$, $V_{f_S-f_T}$) were added to obtain the resultant voltage $V_R = V_{f_S+f_T} + V_{f_S-f_T}$. Finally, the RMS value of the temperature oscillation of the PRT was obtained from $\Delta T_{RMS, f_T} = V_R / [I_{AC} R \alpha]$.

The measured amplitude of temperature oscillations using scheme 4, at 280 K, for a range of heating currents are shown in Figure 3-12. Further, the results obtained for the same heating currents using scheme 3 are also shown for comparison. It can be clearly seen—as

predicted by our analysis—that the temperature resolution of scheme 4 ($\sim 40 \mu\text{K}$) is much better than the temperature resolution of scheme 3 ($\sim 250 \mu\text{K}$). The measured NET is also in good agreement with the predicted values, which are shown as a band to represent the uncertainty in the predicted NETs (Table 3-2). Similar experiments performed at 80 K also show good agreement with the estimated NETs and not shown here in the interest of space.

3-8- Conclusion

In this chapter, I have presented a broad analysis of the different scenarios of electrical resistance-based thermometry that are suitable for nanoscale heat transport studies. This detailed analysis delineates the contributions of both the voltage noise resulting from intrinsic and extrinsic sources and the voltage noise arising from temperature drift. Further, this analysis quantifies the noise equivalent temperature that is in principle achievable using different thermometry schemes. Presented experiments and analysis demonstrate that it is beneficial to use a scheme where the temperature can be modulated as this enables the measurement of temperature changes with high resolution due to its immunity to low temperature drift. Our work also points out that if the temperature cannot be modulated, high resolution thermometry can still be accomplished by using a modulated sensing current and a matching thin film resistor which has a temperature drift that corresponds to that of the sensing resistor. Finally, this work shows that it is readily possible to resolve temperature changes with electrical resistance-based thermometry well below $100 \mu\text{K}$ which we believe will enable a dramatic improvement in the heat-current resolution of microdevices used for probing nanoscale phonon and photon transport.

CHAPTER 4

Resistance Thermometry-based Picowatt-Resolution Heat-Flow Calorimeter

4-1- Abstract

In this chapter, I demonstrate how the high-resolution resistance thermometry techniques described in previous chapter can be used to develop an all-electrical heat-flow calorimeter capable of measuring modulated heat currents with ~ 5 pW resolution. This is achieved by combining the excellent thermal isolation of a microdevice suspended by thin and long beams ($G_{Th} = \sim 150$ nW/K) with a high-resolution resistance thermometer that enables temperature measurements with $10 - 50$ μ K resolution. The calorimeter described here has a resolution comparable to state-of-the-art bimaterial cantilever-based calorimeters, described in the chapter 2 of this thesis, but requires a significantly less demanding instrumentation setup and surpass previous designs by dissipating an order of magnitude lower power in the measurement process.

4-2- Introduction

Resistance thermometer-based micro-calorimeters with a heat current resolution of ~ 1 nW have been widely used in phonon transport studies [15, 47, 48]. Such calorimeters are attractive due to both their good resolution and the relative ease with which resistance

thermometry can be performed. In addition to these, micro-calorimeters based on bimaterial cantilever thermometers, with heat current resolutions of ~ 40 pW, have been used as optomechanical sensors[17] and employed for photothermal spectroscopy[49] and near-field radiative heat transport studies[18]. Although calorimeters based on bimaterial cantilever thermometers have demonstrated superior heat-flow resolutions [50], as small as 4 pW and even sub-picowatt resolutions [51], their application in phonon and photon transport studies is limited by their susceptibility to mechanical vibrations, imposing stringent constraints on ambient vibration isolation. Further, bimaterial cantilever-based calorimeters require additional instrumentation for detection of cantilever deflections, typically an optical scheme, which imposes significant additional requirements on the instrument used for the transport studies. Therefore, achieving high-resolution (\sim pW) calorimetry with resistance thermometers could significantly facilitate the exploration of conductive thermal transport in a wider range of low thermal conductance nanostructures, down to the single molecule level as well as radiative thermal transport in nanoscale gaps that are of fundamental scientific and technological interest [22, 52, 53].

In this chapter, I demonstrate that high-resolution heat flow calorimetry measurements can be performed with resolutions comparable to or better than bimaterial cantilever-based micro-calorimeters using an all-electrical scheme. This is accomplished by leveraging high-resolution temperature measurements (~ 20 μ K resolution) that are possible when an unmodulated sensing current is used to measure modulated temperature changes as described in detail in chapter 3. Next, I introduce this resistance thermometry-based, picowatt-resolution heat-flow calorimeter by first presenting its design and estimating the thermal properties and resolution.

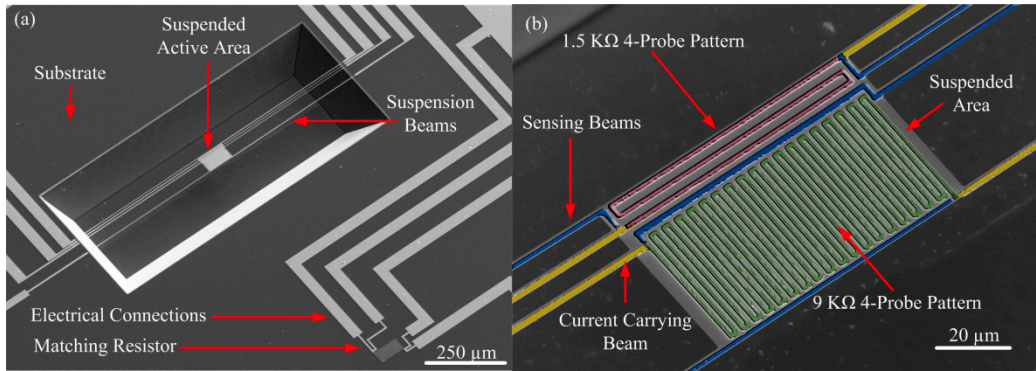


Figure 4-1- scanning electron microscope (SEM) images of the fabricated devices. (a) SEM image of microfabricated device which consists of the suspended device and a matching resistor. The central area of the device is suspended by eight $2\ \mu\text{m}$ wide, $500\ \text{nm}$ thick and $400\ \mu\text{m}$ long beams. (b) Magnified image of the suspended region. Two platinum (Pt) 4-probe thermometers are integrated into the suspended region. The first sensor consists of a long serpentine line (shown in green), which has a resistance of $\sim 9\ \text{k}\Omega$ between the voltage measuring probes (false-colored in blue) and serves as a Pt resistance thermometer (PRT). The second 4-probe (shown in red) has a resistance of $\sim 1.5\ \text{k}\Omega$ between the voltage measuring probes that are false-colored in blue and is used as a micro-heater to input known amounts of heat via Joule heating. The Pt lines of both the 4-probes are $\sim 800\ \text{nm}$ wide and $\sim 30\ \text{nm}$ thick.

4-3- Design of micro-calorimeter

The microfabricated low-stress silicon nitride (SiN) devices employed in this study (Figure 4-1) feature an $80\ \mu\text{m} \times 50\ \mu\text{m}$ suspended region that is thermally isolated from the device substrate by eight $400\ \mu\text{m}$ long suspension beams that have a width of $\sim 2\ \mu\text{m}$ and a thickness of $\sim 500\ \text{nm}$. Further, two 4-probe, platinum (Pt) serpentine lines are integrated into the device.

The first 4-probe consists of a long serpentine line (shown in green in Figure 4-1b) with a resistance of $\sim 9\ \text{k}\Omega$ between the voltage measuring probes (false-colored in blue) and serves as a Pt resistance thermometer (PRT). The second 4-probe (shown in red in Figure 4-1b) is designed to have a resistance of $\sim 1.5\ \text{k}\Omega$ between the voltage measuring probes (false-colored in blue) and is used as a micro-heater to input known amounts of heat via Joule heating. Both serpentine lines are $\sim 1\ \mu\text{m}$ wide and $\sim 30\ \text{nm}$ thick. One electrical lead is integrated into each

of the eight suspension beams enabling the incorporation of a total of eight leads that are required to electrically address the two 4-probe Pt lines. In order to reduce heat dissipation in the current-carrying beams (shown in yellow in Figure 4-1b), a 100 nm thick layer of Au is deposited on them. Further, to reject the deleterious effects of ambient temperature fluctuations on the temperature resolution of the PRT, a second PRT (matching resistor), with the same resistance as the sensing PRT, is integrated into the substrate in close proximity of the suspended device (Figure 4-1a).

4-4- Device fabrication process



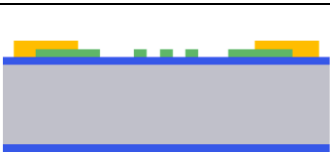


The fabrication process starts by depositing low-stress low-pressure chemical vapor deposition (LP-CVD) of silicon nitride (SiN_x) on both sides of a 500 μm thick, p-type Si wafer (step 1, Table 4-1). Patterns of sensing, matching, and heater lines are transferred onto the photoresist by a combination of high-resolution lithography and electron beam evaporation of 30 nm thick Pt film on the wafers, followed by the lift-off process (step 2, Table 4-1). All Pt lines are 0.8 μm wide in the serpentine region and 1 μm wide on the suspension beams. Subsequently, using a lift-off process 100 nm of Au is deposited on current carrying beams as well as to pattern the electrical leads and wire-bond pads (step 3, Table 4-1). Next, the suspension beam pattern is transferred to nitride layer by patterning photoresist to create a soft mask and plasma etching of the nitride film (step 4, Table 4-1). All devices are released at the wafer level, by wet etching using 40% KOH solution in DI water (step 5, Table 4-1). Finally, all the devices are dried using critical point drying.

4-5- Estimation of the device thermal conductance and thermal time constant

The microdevice has a central region that is suspended by thin and long beams. Given this geometry it is reasonable to expect that the resistance to heat flow within the island is very

small compared to the resistance to heat flow in the SiN_x beams. In order to validate this hypothesis, which was found to be true in similar suspended devices [15, 50], we performed finite element method (FEM) simulations. In these simulations, heat was input into the suspended region of the device in the serpentine heater, which results in joule heating. The amount of current supplied was adjusted to produce a maximum temperature increase of ~1 K in the suspended micro-device. The resultant temperature distribution, presented in Figure 4-2a and b, clearly shows that most of the temperature drop occurs in the suspending beams.

Table 4-1- Fabrication process of the picowatt resolution calorimeter based on resistive thermometer

	Process	Detail	Schematic
	LP-CVD Low-stress silicon nitride deposition on both sides.	Nitride: 500nm	
	Heater line pattern transfer.	Cr/Pt: 3/30 nm, lift-off	
	Electrical leads and wire-bond pads.	Cr/Au: 3/100 nm, lift-off	
	Patterning the suspended active area on nitride layer.	Plasma etch	
	Releasing the devices using KOH wet etch process.	40% KOH at 85°C	

Silicon: ■, Low-stress Silicon nitride: ■, Platinum thermometer: ■, Electrical connection Au Line: ■.

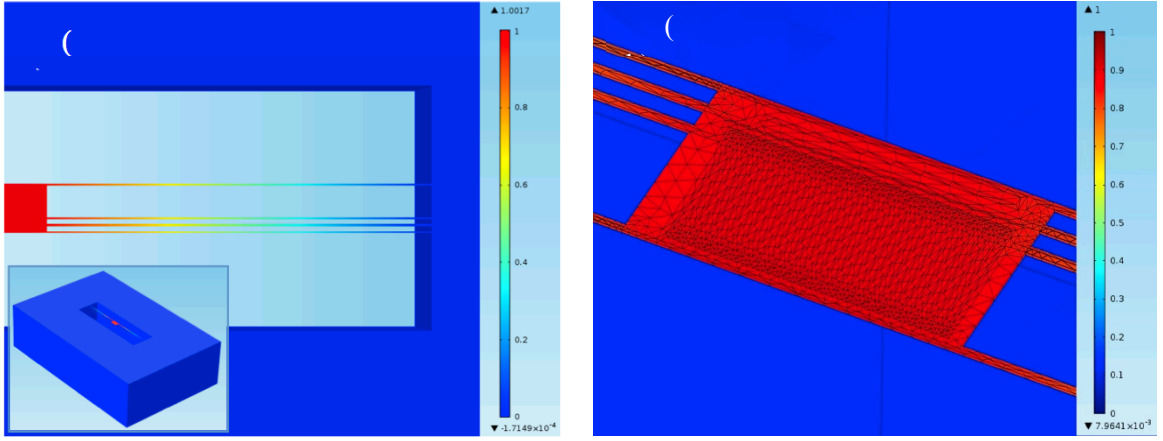


Figure 4-2- Results of FEM analysis predicting temperature distribution on device. (a) All boundaries except the top surface were held at 300 K, whereas an insulating boundary condition is used for the top surface. Inset shows overall view of the simulated device. (b) Meshed model overlaid on computed temperature distribution from FEM analysis. The thermal gradients within the suspended region of the device are seen to be negligible.

Further, the suspended region of the device has very small thermal gradients that are negligible (Figure 4-2b). These simulations clearly confirm the validity of the above stated hypothesis. Figure 4-2a-inset, shows the overall view of the model used in simulation.

Since the temperature differentials inside the island are very small, it is legitimate to use the lumped capacitance approach as it was discussed in chapter 3. Therefore, the total thermal conductance (G_{Th}) of the suspension beams including the Pt film and the extra Au layer on the current carrying beams is estimated using Fourier's law [54] ($G_{Th} = [8(k_{SiN_x} A_{SiN_x} + k_{Pt} A_{Pt}) + 4(k_{Au} A_{Au})] / L_b$), to be ~ 150 nW/K, where k_{SiN_x} (~ 2.3 W/m.K) [25], k_{Pt} (~ 32 W/m.K) [55] and k_{Au} (~ 82 W/m.K) [26] are the thermal conductivities of thin silicon nitride, Pt and Au films respectively, whereas A_{SiN_x} , A_{Pt} , and A_{Au} are the cross sectional areas of the silicon nitride beams, and the Pt and Au films respectively, and L_b is the length of the beams.

Further, we estimated the thermal conductivities of deposited Pt and Au thin films, using Wiedemann-Franz law to be $k_{Pt} = 25.9$ W/m.K and $k_{Au} = 75.7$ W/m.K showing a good

agreement with above mentioned values from literature. The thermal time constant (τ) of the device limits the temporal response of the microdevices and plays an important role in determining the smallest heat-current that can be detected (explained in detail below). The thermal time constant can be estimated from $\tau = C/G_{Th}$ using the lumped capacitance model[56], where c is the heat capacity of the suspended area. Using this simple model, we estimate the thermal time constant for the micro-device under consideration to be ~ 33 ms. This estimate suggests that sinusoidal heat currents at a frequency much smaller than the cut-off frequency ($f_c = 1/(2\pi\tau) \sim 5$ Hz) result in a full thermal response whereas heat currents modulated at higher frequencies result in an attenuated response.

4-6- Estimation of the heat current resolution

The resolution of the calorimeter device (Q_{Res}) is directly proportional to the resolution of the thermometry technique, ΔT_{Res} , ($Q_{Res} = G_{Th} \times \Delta T_{Res}$). Our recent analysis [57] shows that high resolution measurements of modulated temperature changes can be performed using an unmodulated DC current. Specifically, our analysis suggests that by employing a DC sensing current of ~ 10 μ A and a PRT of ~ 9 K Ω it is possible to detect modulated temperature changes with resolutions in the range of 10 – 50 μ K in a bandwidth of ~ 1.5 mHz. This temperature resolution, taken together with the estimated thermal conductance G_{Th} of ~ 150 nW/K, implies that heat currents well below 10 pW ($Q_{Res} = G_{Th} \times \Delta T_{Res}$) can be resolved.

4-7- Experimental determination of the optimal heat current modulation frequency

To achieve the highest possible heat current resolution, it is necessary to establish the optimum frequency of modulation of the heat current at which the signal (amplitude of temperature oscillations) to noise (voltage noise-limited temperature resolution ΔT_{Res}) ratio

reaches a maximum. First, we determined the frequency dependence of the amplitude of temperature oscillations of the device by performing an experiment where the PRT (Figure 4-1c) was used as both a heater and thermometer. In this experiment, a modulated electrical current $I = I_0 \cos(2\pi ft)$ was supplied through the PRT, which results in joule heating. The total power dissipated in the suspended region of the device is given by

$$P_{Suspended} = \frac{I_0^2 R_s}{2} (1 + \cos(2\pi \times 2f \times t)),$$

where R_s ($\sim 9 \text{ k}\Omega$) is the resistance of the sensing part of the PRT. Similarly, the total heat dissipated in the leads supplying the electric current is given by

$$P_{Lead} = 2 \times \left[\frac{I_0^2 R_l}{2} (1 + \cos(2\pi \times 2f \times t)) \right],$$

where R_l ($\sim 450 \text{ }\Omega$) is the resistance of each of the leads located on top of each of the suspension beams (Figure 4-1c).

Joule heating is present not only in the suspended region of the microdevice but also in two of the suspension beams. This additional heat generation occurs in the current carrying leads of each 4-probe serpentine line (Figure 4-3). In order to account for the effect of heat generation in the suspension beams we modeled heat transfer using a 1-dimensional heat transfer model (with heat generation in the beams). In this model, we assume that the all the thermal gradients are present in the beams and the temperature gradients in the cross-section of the beam are negligible. Further, we assume that the entire suspended region is at an elevated temperature ($T + \Delta T$) whereas the rest of substrate to which the beams are anchored is at the ambient temperature T (Figure 4-3).

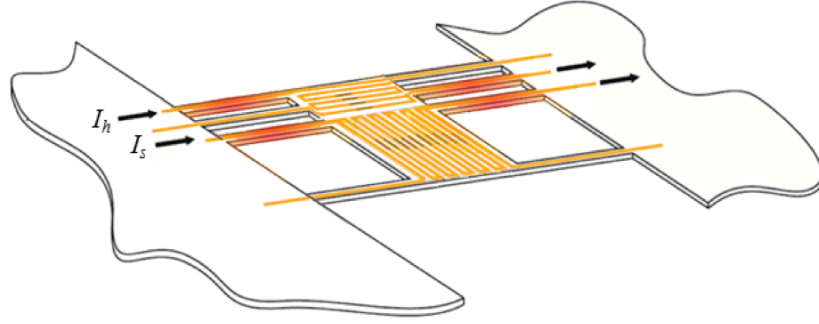


Figure 4-3- Schematic of the suspended device. Out of the eight suspending beams, heat is generated only in four beams in which an electrical current is supplied.

We also note that since the experiments were performed in a vacuum, therefore the effect of conduction through air is negligible. Further, the effect of radiative heat transfer was also estimated and found to be negligible. The results of this modeling are summarized in the equation below, which suggests that the conductance of the beams (G) is related to the temperature rise (ΔT) of the suspended region of the island by the following equation:

$$G_{Th} = \frac{Q_{serpentine} + Q_{beams} / 2}{\Delta T} \quad (4-1)$$

where $Q_{serpentine}$ is the power dissipated in the suspended region of the microdevice due to joule heating and Q_{beams} is the total power dissipation ($Q_{beams} = Q_{beam1} + Q_{beam2}$) in the current carrying beams (Figure 4-3). It can be seen from Equation (4-1) that only half of the heat generated in the beams is “effectively” transferred to the island. Therefore, it is necessary to consider the heat power when it is comparable to heat generation in the serpentine area. To decrease this ratio, we deposited an additional Au layer on current carrying beam to decrease the resistance of wires on each beam to $\sim 450 \Omega$. Since the electrical resistance of the serpentine line used for heating is $\sim 2 \text{ k}\Omega$, heat generation on the suspension beams, $Q_{beams}/2$ which equals $I^2 R_{beams}/2$ is approximately 20% of the joule heating in the serpentine region ($Q_{serpentine} = I^2 R_{serpentine}$).

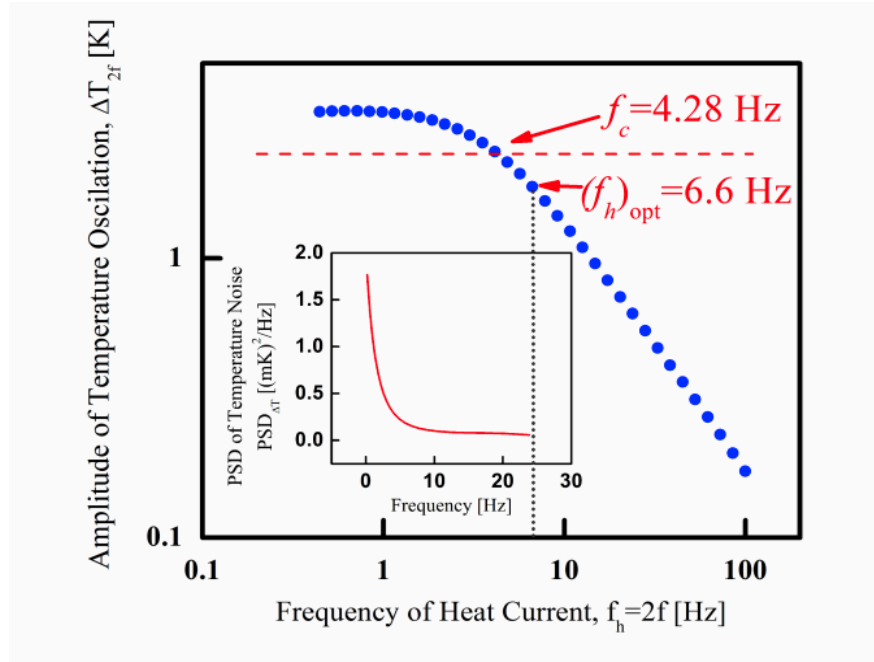


Figure 4-4- Temperature response as a function of frequency of heat currents (500 nW) of constant amplitude. The inset shows the power spectral density of the noise associated with temperature measurements.

Therefore, the effect of Joule heating in the beams is not negligible and is accounted for using Equation (4-1).

Therefore the modulated heat current induces sinusoidal temperature oscillations in the suspended region whose amplitude ΔT_{2f} is given by:

$$\Delta T_{2f} = [I_0^2 (R_s + R_l)] / 2G_{Th}. \quad (4-2)$$

These temperature oscillations in turn result in a sinusoidal voltage output at $3f$ across the sensing leads[58] whose amplitude ΔV_{3f} is given by $\Delta V_{3f} = \frac{I_0 \alpha R_s}{2} \times \Delta T_{2f}$, where α is the temperature coefficient of resistance. Thus, from knowledge of ΔV_{3f} , α , and R_s it is possible to directly obtain ΔT_{2f} .

To accomplish this goal, we first measured [59] the temperature coefficient of resistance (α) for Pt thin films. The measured value of α at 280 K was found to be $1.7 \times 10^{-3} \text{ K}^{-1}$, which is in good agreement with reported values for films with comparable thicknesses [47].

The voltage of interest, ΔV_{3f} , was obtained by employing a differential scheme that takes advantage of the matching resistor integrated into the chip (as explained in chapter 3) and used to extract ΔT_{2f} . Figure 4-4 shows the measured ΔT_{2f} as a function of the frequency of thermal excitation ($f_h = 2f$). It can be seen that, at low frequencies, the amplitude of temperature oscillations remains unchanged as the heating frequency (f_h) is increased; however, at higher frequencies the response is monotonically attenuated. The experimentally measured cut-off frequency (f_c) of the heat current is ~ 4.28 Hz and is in good agreement with the value estimated based on the lumped parameter model (~ 5 Hz).

The resolution of the calorimeter depends on the temperature response of the device to the modulated heat current as well as on the resolution of the resistance thermometer, which is also dependent on the frequency [59]. Therefore, to identify the frequency of heat-current modulation at which the resolution of the calorimeter is a maximum it is necessary to characterize the frequency dependence of the temperature resolution.

4-8- Estimation of the noise of the thermometry scheme

The thermometry scheme adopted in this study, employs an unmodulated sensing current (I_s) to detect temperature changes modulated at a known frequency f_h . In this scheme, the sensing resistor is subject to a periodic temperature modulation ($\Delta T \sin(2\pi f_h t)$), which when excited by an unmodulated sensing current (I_s), results in a voltage signal across the sensing resistor given by:

$$V_{Out} = \underbrace{I_s R \alpha \Delta T \sin(2\pi f_h t)}_{Signal} + V_{Noise} \quad (4-3)$$

where V_{Out} is the measured voltage at the output of the differential measurement configuration, shown in Figure 4-2, V_{Noise} is the voltage noise of the measurement and R and α are resistance of the PRT and TCR of the sensing resistor, correspondingly. The Noise Equivalent Temperature (NET) of the measurement is defined as:

$$NET = \frac{V_{Noise}}{I_s R \alpha} \quad (4-4)$$

The mean square of voltage noise (V_{Noise}^2) can be estimated from:

$$V_{Noise}^2 = \Delta V_{Amp Total}^2 + \Delta V_{Temperature Drift}^2 \quad (4-5)$$

where $\Delta V_{Temperature Drift}^2$ is the mean square voltage noise associated with temperature drift of the sensing PRT, and $\Delta V_{Amp Total}^2$ is the mean square electrical noise due to intrinsic noises of the measurement and amplifier non-idealities. Given the bandwidth of the measurement (Δf), both these components can be estimated from:

$$\Delta V_{Temperature Drift}^2 (f = f_h) = (I_s R \alpha)^2 \int_{f_h - \Delta f/2}^{f_h + \Delta f/2} PSD_{\Delta T, Drift}(f) df \quad (4-6)$$

and

$$\Delta V_{Amp Total}^2 (f = f_h) = \int_{f_h - \Delta f/2}^{f_h + \Delta f/2} PSD_{Amp Total}(f) df \quad (4-7)$$

where $PSD_{\Delta T, Drift}$ is the power spectral density of the temperature drift of the sensing PRT and $PSD_{Amp Total}$ is the power spectral density of the electrical noise.

Both power spectral densities were characterized following the procedures described in chapter 4 and are shown in Figure 4-5.

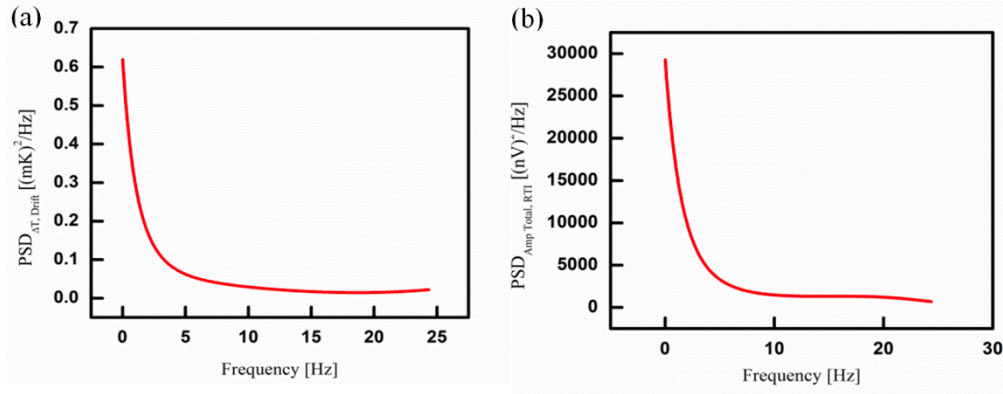


Figure 4-5- Obtained power spectral densities of (a) temperature drift of the sensing PRT and (b) relative-to-input electrical noise.

4-9- Characterization of the optimum frequency of heat current modulation

In order to characterize the optimum frequency of heat current modulation, we used the experimentally obtained the power spectral density of noise associated with temperature measurements ($PSD_{\Delta T}(f)[K/Hz^2]$). The observed $PSD_{\Delta T}(f)$ (shown as inset of Figure 4-4) decreases rapidly with increasing frequency up to ~ 5 Hz.

Thus, it is intuitive that increasing the measurement frequency to above 5 Hz will minimize noise contributions. We note that the temperature resolution at a frequency f_h and in

a bandwidth of Δf is given by $\Delta T_{Res}(f_h) = \int_{f_h - \Delta f/2}^{f_h + \Delta f/2} PSD_{\Delta T}(\tilde{f}) d\tilde{f}$ and can be used to estimate the

signal to noise ratio (SNR) of the calorimeter as a function of the modulation frequency of the heating current:

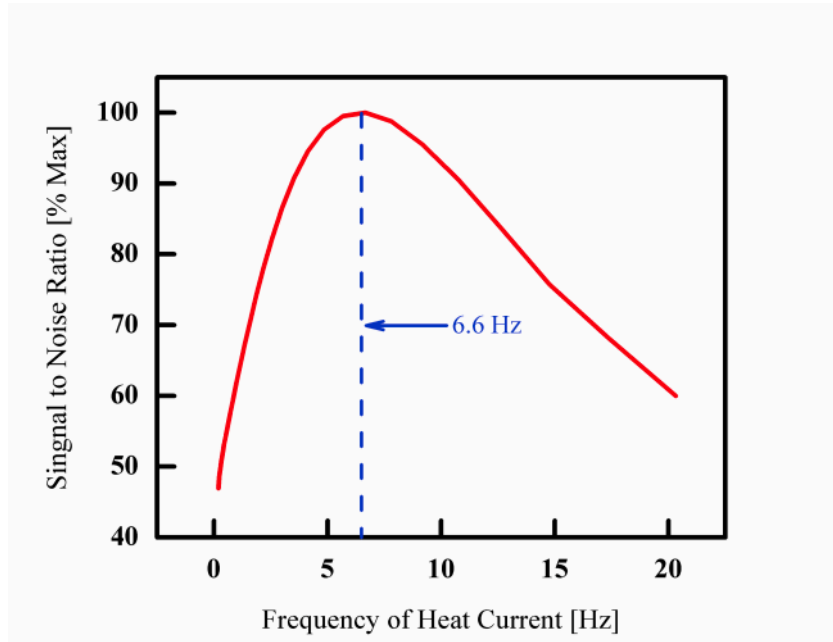


Figure 4-6- Estimated signal to noise ratio computed from the data shown in Fig. 2a. The signal to noise ratio reaches a maximum when the heating current is modulated at 6.6. Hz.

$$SNR(f_h) = \frac{\Delta T_{2f}(f_h)}{\Delta T_{Res}(f_h)} \quad (4-8)$$

The estimated SNR (estimated for a bandwidth of 1.5 mHz) is shown in Figure 4-6 and has a maximum at a heating frequency of 6.6 Hz. Thus, the optimum frequency of heat current modulation $f_{h, opt} = 6.6$ Hz.

4-10- Characterization of the thermal conductance of the device

To experimentally characterize the thermal conductance of the suspended device, we performed a series of experiments where a sinusoidal electric current at 1 Hz, was supplied through the PRT while systematically incrementing the amplitude of the current (I_0) and monitoring the amplitude of temperature oscillations of the suspended region at 2 Hz ($\Delta T_{2f=2 \text{ Hz}}$). We note that the chosen frequency of heat flow modulation (2 Hz) is well below the roll-off frequency of the device ensuring the full temperature response.

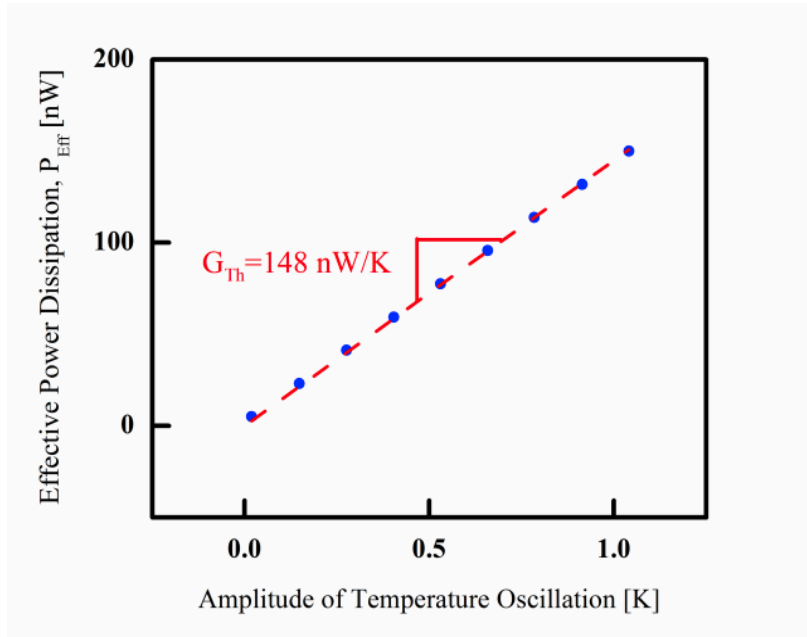


Figure 4-7- The thermal conductance of the beams, G_{th} is determined from a linear regression between the effective power dissipation, P_{Eff} , at 2 Hz and the resultant amplitude of the temperature oscillations. The coefficient of determination (R^2) for the linear regression model is found to be 0.9994.

In this scenario, the temperature rise in the suspended region is given by Equation (4-2). This suggests that G_{Th} can be determined by measuring the amplitude of temperature oscillations while the effective power dissipation (P_{Eff}) in the suspended region[59], ($P_{Eff} = I_0^2(R_s + R_l)/2$), is increased in well-defined steps. Figure 4-7 shows P_{Eff} as a function of the measured amplitude of the temperature oscillations. From this data, the thermal conductance of the device is estimated to be $\sim 148 \pm 4$ nW/K and is in good agreement with the modeled results (150 nW/K). We note that all the experiments described above were performed inside a vacuum chamber ($\sim 10^{-3}$ Tor) to eliminate parasitic heat conduction through air molecules. Further, to minimize the effects of ambient temperature drift the temperature of the setup was controlled to be $280 \text{ K} \pm 5 \text{ mK}$.

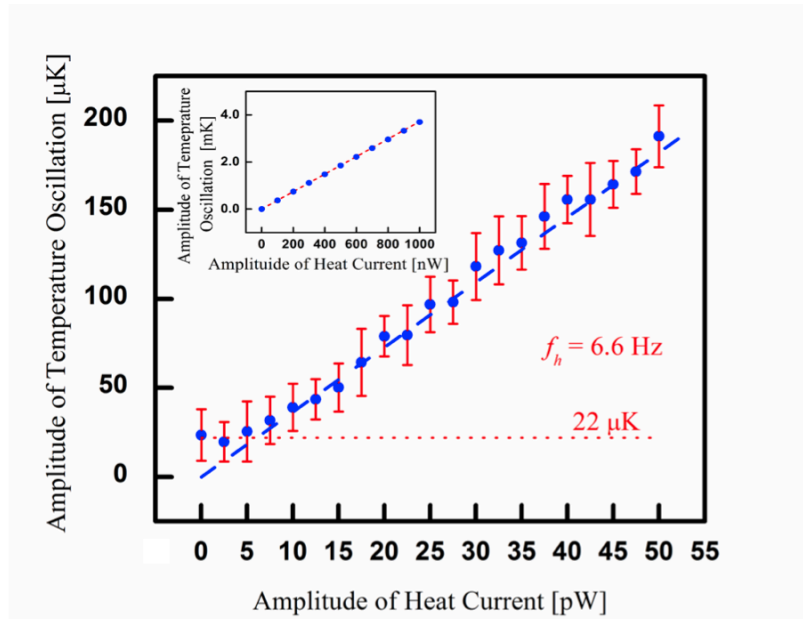


Figure 4-8- The measured amplitude of the temperature oscillations for heat currents of various amplitudes that are modulated at f_h , Opt = 6.6 Hz. The experimentally measured noise floor (20 μK) agrees well with calculated thermometry noise floor of $\sim 22 \mu\text{K}$ (red dashed line). We note that the modulation frequency of 6.6 Hz is beyond the thermal bandwidth of the device ($f_c \sim 4.3 \text{ Hz}$), therefore, the amplitude of temperature oscillations is attenuated (by a factor of 1.9, see Fig. 2a). The dashed line (blue) accounts for this effect and predicts the amplitude of temperature oscillations from $\Delta T = (\text{amplitude of heat current}) / (1.9G_{Th})$. The inset shows that the response of the device to heat inputs of up to 1 μW is linear, demonstrating a dynamic range of more than 100 dB.

4-11- Experimental determination of the resolution of the heat flow calorimeter

To experimentally demonstrate the heat-flow resolution of the device, we input known sinusoidal heat currents modulated at a frequency of 6.6 Hz (the optimal frequency) into the suspended micro-device via the micro-heater (resistance 1.5 $\text{k}\Omega$) integrated into suspended region of the device. The resultant temperature oscillations of the suspended region are measured by supplying a DC sensing current ($I_s = 10 \mu\text{A}$) through the PRT and recording the voltage oscillations at 6.6 Hz using a lock-in amplifier in a measurement bandwidth of $\sim 1.5 \text{ mHz}$. Figure 4-8 shows the measured temperature changes when the amplitude of the heat

currents is increased in steps of 2.5 pW from 0 to 50 pW. The mean value and uncertainty of each of the data points shown in Figure 4-8 represent the mean and standard-deviation of the signal obtained from the lock-in amplifier when the voltage output of the lock-in amplifier is continuously monitored for ~50 minutes.

The measured data unambiguously shows that, heat currents as small as 6 pW, as well as changes in heat currents as small as 5 pW, are readily detectable using the developed calorimeter. The dotted line (red) represents the calculated noise floor of the PRT (~22 μ K) which is in good agreement with the experimentally obtained noise floor (~19 μ K) of the platinum resistance thermometer. The dashed line (blue) in Figure 4-8 shows the predicted amplitude of temperature oscillations $\Delta T = (\text{amplitude of heat current}) / (1.9G_{Th})$ based on the known frequency response of the device (Fig. 2a) and the measured thermal conductance of the device. Here, the factor of 1.9 accounts for the attenuation in the thermal response of the device due to operation at $f_{h, Opt} = 6.6$ Hz. Finally, in the inset of Figure 4-8 we show the excellent linear response of the device (the R-square measure of goodness of fit is 1) to modulated ($f_{h, Opt} = 6.6$ Hz) heat currents whose amplitude ranges from 10 pW – 1 μ W, clearly demonstrating a dynamic range of greater than ~100 dB.

4-12- Comparison to bimaterial cantilever (BMC) based micro calorimeter

It is instructive to compare the heat-flow resolution of this PRT-based micro-calorimeter with that of a (BMC) based micro-calorimeter described by us recently[50], which has a resolution of ~4 pW in a measurement bandwidth of ~1.5 mHz. In order to provide a fair comparison we first note that the power dissipated ($P_{Sensing}$) by the DC sensing current in the current micro-device is $I_s^2 R_s \sim 1$ μ W. Whereas, in the BMC based device sensing was accomplished using an optical approach where ~1 mW of light was incident on the device which resulted in an absorption of ~30 μ W of power. Employing a larger sensing current ($I_s =$

40 μA) in our experiments, increases the sensing heat overhead of the measurement to ~ 16 μW and enables a direct improvement of the heat-flow resolution to ~ 1.6 pW[59]. However, this increased heat dissipation leads to a large DC temperature rise (~ 100 K) of the suspended region (this is also true for BMC based devices[50]) which poses significant challenges to performing low temperature transport measurements.

4-13- Conclusion

In summary, I have presented an all-electrical heat flow calorimeter capable of resolving heat currents with ~ 5 pW resolution in a bandwidth of 1.5 MHz. This improvement is due to high-resolution resistance thermometry measurements achieved by employing a matching resistance to reject ambient temperature fluctuations and adopting a thermometry scheme where an unmodulated sensing current is used to detect modulated temperature changes. The enhanced heat-flow calorimetric resolution demonstrated here will enable and simplify fundamental studies of phonon transport at the molecular scale and near-field radiative heat transfer in nanoscale gaps.

CHAPTER 5

High Resolution Heat Flow Calorimeters for Studying Radiative Energy Transfer in Near-Field Regime

5-1- Abstract

In this chapter, I will describe how I leveraged the experience gained in the development of high-resolution heat flow calorimeters, presented in previous chapters, to study Near-Field Radiative Heat Transfer (NF-RHT). I present the results of our study of the effect of film thickness on near-field thermal transport. This study was conducted using calorimeter devices, specifically tailored to meet the stringent requirements of this study, in conjunction with a novel six degree of freedom nano-positioning stage developed in our group. Specifically, I show—for the first time—that heat transfer between a very thin (~50 nm) dielectric film of silicon dioxide (SiO_2) and bulk SiO_2 is dramatically enhanced due to NF-RHT and reaches values similar to that of heat transfer between two bulk SiO_2 films when the gap size is comparable to the film thickness. This interesting observation is understood on the basis of detailed computational analysis which shows that the near-field heat transfer is completely dominated by the excitation of surface phonon-polaritons whose effective skin depth scales with the gap size. These results have important implications for the development of thermo photovoltaic devices based on NF-RHT.

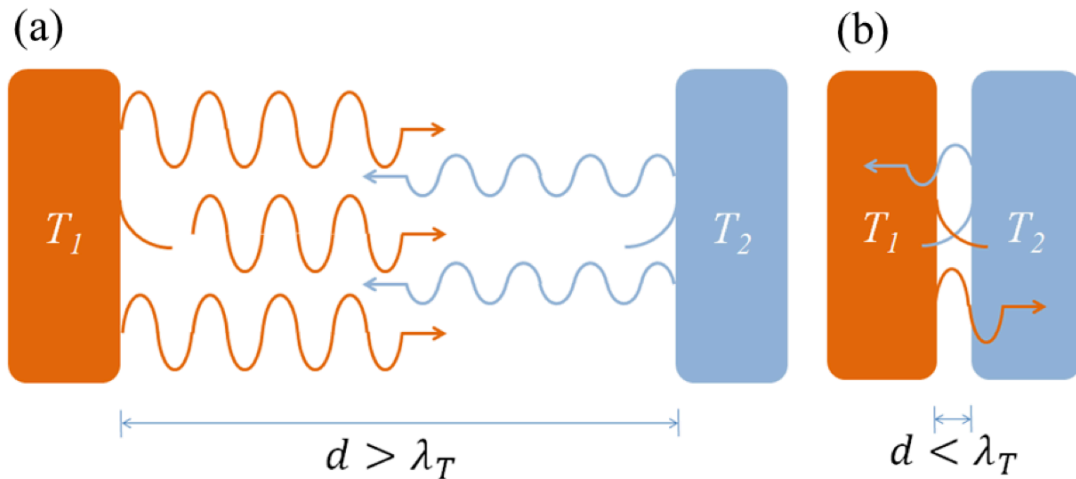


Figure 5-1- Radiative energy transfer phenomena. (a) far-field energy transfer is dominated by propagating electromagnetic waves and independent of distance; (b) near-field energy transfer is dominated by evanescent waves and shows strong distance dependence.

5-2- Introduction

Studying radiative energy transfer between bodies at finite temperatures has attracted attention of many scientists. Describing the magnitude and spectral contents of radiated energy from a black body at the turn of the 20th century, has played an important role in formulating quantum mechanics and developing modern physics. The maximum possible radiative heat flux (q) between two “infinite” parallel surfaces at finite temperatures is described by the Stefan-Boltzmann Law [60]:

$$q = \sigma(T_1^4 - T_2^4) \quad (5-1)$$

where σ is Stefan-Boltzmann constant and $T_{1,2}$ are the temperatures of the interacting bodies. This energy exchange is independent on the distance between the surfaces as long as the separation is greater than the distance predicted by Wein’s wavelength (Figure 5-1a). However, when the surfaces are in sub-wavelength distances or the so-called near-field region (Figure 5-1b), the Stefan-Boltzmann Law fails to describe the radiative heat transfer. In fact, theoretical studies predict a dramatically enhanced heat flux between the two surfaces due to an increased density of electromagnetic states in close proximity of the interfaces,

which in turn leads to increased heat transfer due to photon tunneling [61]. In material systems that support surface waves, the enhanced density of states is attributed to surface plasmons or surface phonon polaritons, which are predicted to have high spatial and temporal coherence on the emitting surfaces[62]. In addition, a number of theoretical studies [63] have reported interesting calculations on how thin films and hetero-structured materials may influence NF-RHT, but none of these predictions have been experimentally tested and explored in any detail. The goal of this work is to advance the experimental analysis of this important question.

Several researchers have made significant efforts to experimentally probe near-field radiative heat transport using a range of techniques. Figure 5-2 categorizes these studies based on the geometry of the interacting surfaces into: tip-plane, sphere-plane and plane-plane configurations. In one of the earliest attempts a Scanning Thermal Microscope (SThM), which has a thermometer incorporated at the tip of a scanning tunneling probe, was used to study NF-RHT between the sharp tip and a planar surface (tip-plane) [64-66]. SThM offers precise control over sub-wavelength gaps down to single nanometers, but the miniscule surface area of the probe makes resolving heat transfer signals challenging. In a second type of study the heat transfer between a spherical sample and planar substrate (sphere-plane) was investigated to gain useful insights into NF-RHT phenomenon [18, 67]. This configuration is experimentally most readily realized, but interpretation of the results is confounded by the spherical shape of the emitter. Finally, there have been efforts to actually study NF-RHT between two planar surfaces (plane-plane). While this is the most desirable of all three configurations in terms of approximations that are required to interpret the data and potential for real applications, aligning and controlling the separation of two planar surfaces with nanometer resolution is extremely demanding [68, 69].

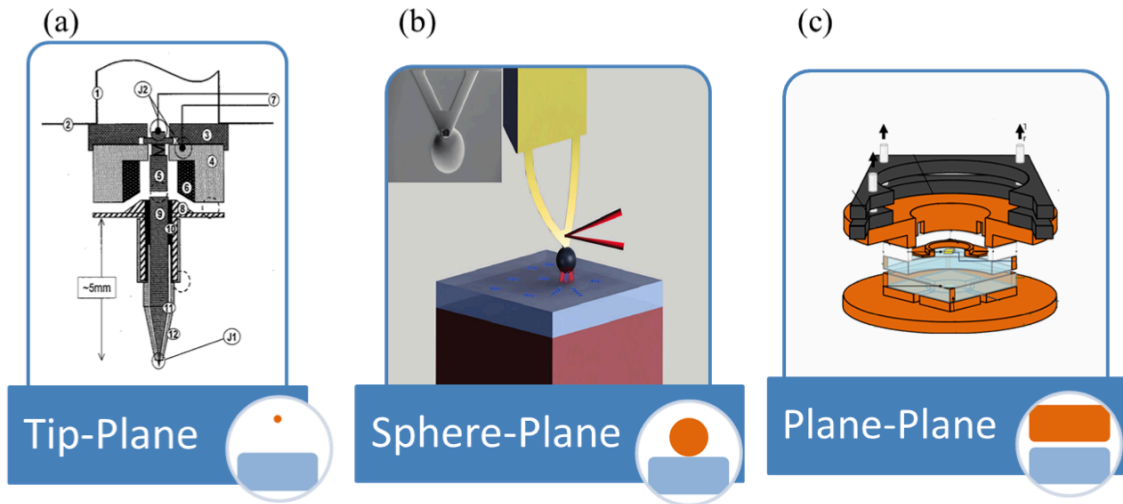


Figure 5-2- Three category of reported experimental studies on near-field radiative heat transfer, based on the geometry of the interacting surfaces.

In this chapter, I will describe our experimental effort to study the effect of film thickness in NF-RHT by quantifying the heat transfer between a bulk emitter and thin-film receivers with different thicknesses in the sphere-plane configuration. *These results provide for the first time experimental evidence of a gap-dependent penetration depth in near-field transport.* Dependence of the penetration depth on the separation between emitter and receiver is unique to near-field and has important implications for improving the performance of future energy conversion devices such as Near-Field Thermo Photo Voltaic (NF-TPV) devices [53, 70].

In the next section, I will briefly describe the theoretical framework used for computing radiative energy transport in the near-field. A more detailed description can be found in several review articles [62, 71] and text books [72]. Subsequently, I will introduce the experimental methodology that we adopted to probe thin film NF-RHT. Finally, I will present the experimental results of our study along with computational modeling of our collaborator, which provides useful insights into our experimental observations.

5-3- Fluctuational electrodynamics

Radiative energy transfer between two bodies in thermal equilibrium can be modeled by analyzing the thermal fluctuation of charges inside the bodies; these charges could be either electrons in metals or ions in polar materials. The theoretical framework, known as fluctuational electrodynamics and first introduced by Rytov [73] provides a statistical picture of random electrical currents using fluctuation-dissipation theorem [74]. Subsequently, the radiative properties of surfaces are calculated by introducing these fluctuating currents as the source term in Maxwell's equations and solving for the resulting electric (\vec{E}) and magnetic (\vec{H}) fields using *Green's functions* consistent with the geometry of the problem.

Polder and van Hove [61], showed that the emitted energy flux from one infinite half-space, can be obtained based on this solution of electrical and magnetic fields, by computing the ensemble time average of the Poynting vector:

$$\langle \vec{S}(\vec{x}, t) \rangle = \frac{c}{4\pi} \langle \vec{E}(\vec{x}, t) \times \vec{H}(\vec{x}, t) \rangle \quad (5-2)$$

where, \vec{x} is the coordinate and c is the speed of light in vacuum. It can be shown that radiative heat transport per unit area between two parallel and infinite half-spaces is given by [62, 71]:

$$q = \frac{1}{\pi^2} \int_0^\infty [\Theta(\omega, T_h) - \Theta(\omega, T_c)] d\omega \int_0^\infty k T(\omega, k) dk . \quad (5-3)$$

This equation describes the heat transfer across two interacting objects as the sum of the contributions from all frequencies. The first term represents the difference in the mean energies ($\Theta(\omega, T)$) of Planck oscillators in the hot and cold bodies:

$$\Theta(\omega, T) = \frac{\hbar\omega}{e^{\frac{\hbar\omega}{k_B T}} - 1} \quad (5-4)$$

where, \hbar is Planck's constant divided by 2π and k_B is the Boltzmann constant.

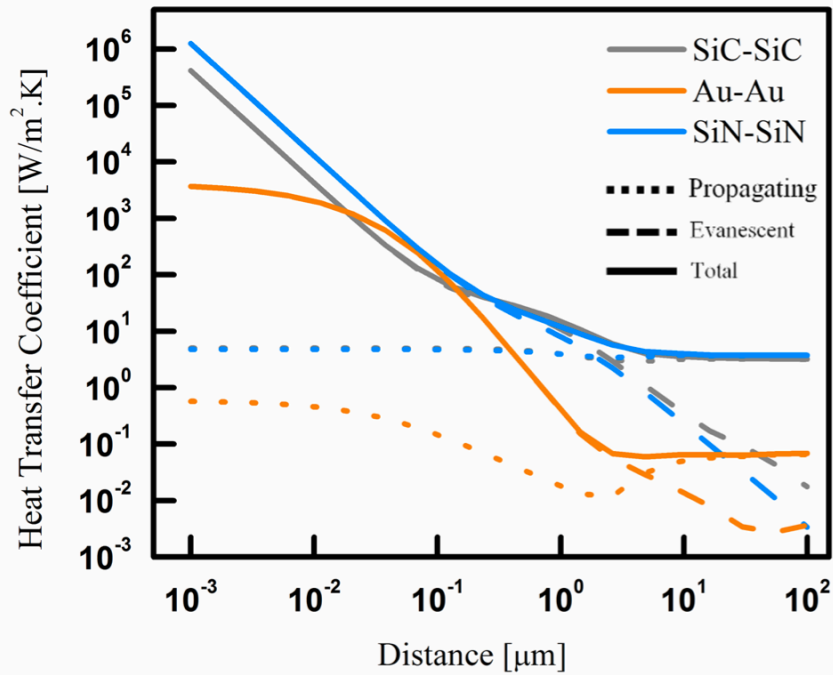


Figure 5-3- Gap-dependent heat transfer coefficient between different emitter-receiver material pairs in the plane-plane configuration, calculated using the fluctuational electrodynamics formalism.

The second term in Equation (5-3) is analogous to a transmission function (in Landauer theory) corresponding to various wave vectors contributing to the transport and is a function of material properties (frequency dependent dielectric function) and the geometrical configuration of the interacting bodies. Following this framework, I computed the heat transfer coefficient between various metal and dielectric half-spaces as a function of spatial separation between the surfaces of the half-spaces (Figure 5-3). From these results it can be seen that the radiative heat fluxes are indeed dramatically enhanced in the near-field for both metallic and dielectric surfaces.

The radiative energy exchange between the hot and cold bodies comprises of two components: The far-field and near-field. It can be seen in Figure 5-3 that at distances larger than the dominant wavelength computed from Wien's law ($\sim 10 \mu\text{m}$ at room temperature), the

interaction is dominated by far-field interaction and is independent of the distance between surfaces. However, as we bring the two surfaces closer than the Wien's wavelength at room temperature, the heat transfer is dominated by near-field component and is increased dramatically. In order to experimentally confirm these theoretical predictions, several groups have employed a sphere-plane configuration that has proved to be very fruitful [18, 67]. In these studies, a silica sphere was brought into close proximity to dielectric and metallic surfaces and it was shown that the thermal conductance increased dramatically at sub-wavelength distances due to contributions from NF-RHT.

The focus of my work is to understand the effect of film thickness dependence on NF-RHT. In other words, we have tried to answer the following questions: How thin can a surface coating be while still having dramatically different near-field properties? What is the mechanism by which thin films support NF-RHT? In the following section, I will describe the methodology that we adopted to address these important questions.

5-4- Methodology

In order to understand the effect of film thickness on near-field thermal transport, we experimentally studied the dependence of NF-RHT on the separation between a spherical emitter and thin film receivers with different thicknesses. In this study both the emitter and receiver material is chosen to be silicon dioxide (SiO_2). However, the design of the experimental platform allows in principle the study of different combinations of materials. This section presents both the novel calorimetric platform employed for studying NF-RHT and the custom-built mechanical platform used for placing and maintaining the relative position between the emitter and receiver surfaces.

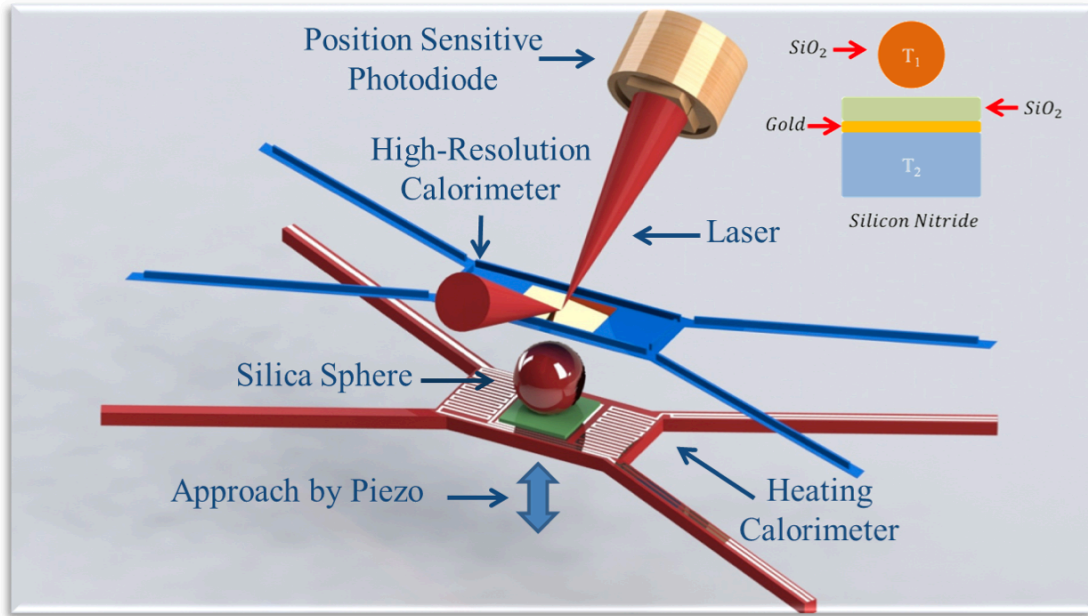


Figure 5-4- Experimental illustration of the experimental setup for studying NFRHT. The temperature of the silica sphere mounted on the heating calorimeter is modulated sinusoidally and the corresponding radiative power coupled to the high-resolution receiver calorimeter is measured by recording the resultant temperature fluctuations of the receiver. The surface of the receiver is coated with different thicknesses of thin film SiO₂. The whole setup is mounted on a 6 DOF nano-positioner inside vacuum chamber.

A. Experimental method

To study NF-RHT one must be able to precisely position the two interacting surfaces, maintain them in desired position throughout the entire length of experiment and precisely quantify heat transfer between the surfaces. Figure 5-4 illustrates the experimental method that we have designed. Here, a silica sphere is brought into close proximity of planar surfaces that were coated with silicon oxide films of different thicknesses.

In order to quantify heat transfer between the two interacting surfaces, they were integrated into two calorimeter devices. The silica sphere was placed on heating calorimeter, and it was made sure that the sphere is in excellent thermal contact with the heating calorimeter. Opposite to the free bead surface site, we incorporated the planar surface into a second calorimeter device, named receiver calorimeter (labeled high-resolution calorimeter in

Figure 5-4). The surface of the receiver calorimeter is coated with a Au film on which oxide films with different thicknesses are deposited (see Figure 5-4, inset). Modulating the temperature on the heating calorimeter by passing a sinusoidal heating current through the resistive heater/thermometer on the heater calorimeter, enables us to modulate the temperature of the silica sphere. We note that we carefully characterized the thermal bandwidth of the system to ensure that the temperature of the active area of the heating calorimeter plus the silica sphere is modulated quasi-statically. This enables us to choose the right modulation frequency according to the procedure described in chapter two and four. This sinusoidally modulating temperature results in a modulated heat current between the silica sphere and the thin-film-coated receiver calorimeter. Finally, the total heat current, which is the sum of far-field and near-field contributions, is quantified at different gap sizes using the techniques described in chapter 4.

In order to precisely control the gap-size, we employed a simple and elegant procedure. Briefly, the micro-sphere mounted on the heating calorimeter was moved towards the receiving calorimeter in small steps ($\sim 5\text{nm}$) using a piezoelectric actuator with an integrated strain gauge sensor (SGS) capable of resolving position changes with a resolution of a few nanometers until a contact was detected via an optical scheme as shown in Figure 5-4. The sensitivity of the strain gauge sensor as calibrated with a capacitive sensor (Lion Precision-CPL290) was measured to be 46 nm/mV . The piezoelectric actuator was operated under PID feedback control to reduce gap uncertainties caused by piezo non-linearity to below of $\sim 2.5\text{ nm}$. The optical contact detection scheme uses a split photodiode to monitor the beam reflected off the backside of the receiver calorimeter.

To step the silica micro-sphere towards the receiver calorimeter and before conducting calorimetric measurements, the z-position of the silica sphere was modulated $\sim 8\text{ nm}$ at a frequency of 4 kHz by applying a sinusoidally modulated voltage of $\sim 4\text{ mV}$ to the

piezoelectric actuator on which the heater calorimeter was mounted. In order to detect contact, the output of the photodiode was monitored using a lock-in amplifier. This procedure was repeated until a photodiode signal at the modulation frequency was detected, which established contact formation. Finally, the contact point was assigned a gap-size of zero and displacement data from the SGS was used to back-calculate gap-size from contact.

B. Mechanical stage

Precise knowledge and control of the distance between the two interacting surfaces is critical for drawing meaningful conclusions on the gap dependence of NF-RHT. Therefore, in addition to the contact detection scheme described previously, it is crucial to have excellent control on the stability of the gap size throughout the entire interval of the experiment. To address the platform requirements, I collaborated with my colleagues in the lab to design a 6 DOF nano-positioner (Figure 5-5) on which we mount the emitter and receiver surfaces, and align them parallel to each other using the procedure explained in our published work [75]. To perform heat transfer measurements the entire set up was placed in a high vacuum chamber ($<10^{-6}$ torr) at room temperature.

Mechanical drift due to thermal fluctuations in the system is attenuated to negligible levels (few nanometers over hours) by employing a 2-stage temperature control system that allows ~ 1 mK temperature stability. Using this system in combination with our piezo feedback loop and stiff microdevices, as explained below, we can achieve gap-sizes as small as 20 nm and larger than ~ 10 μm with a minimum step size of ~ 2.5 nm. The minimum gap-size is limited by the inherent roughness of the spherical emitters.

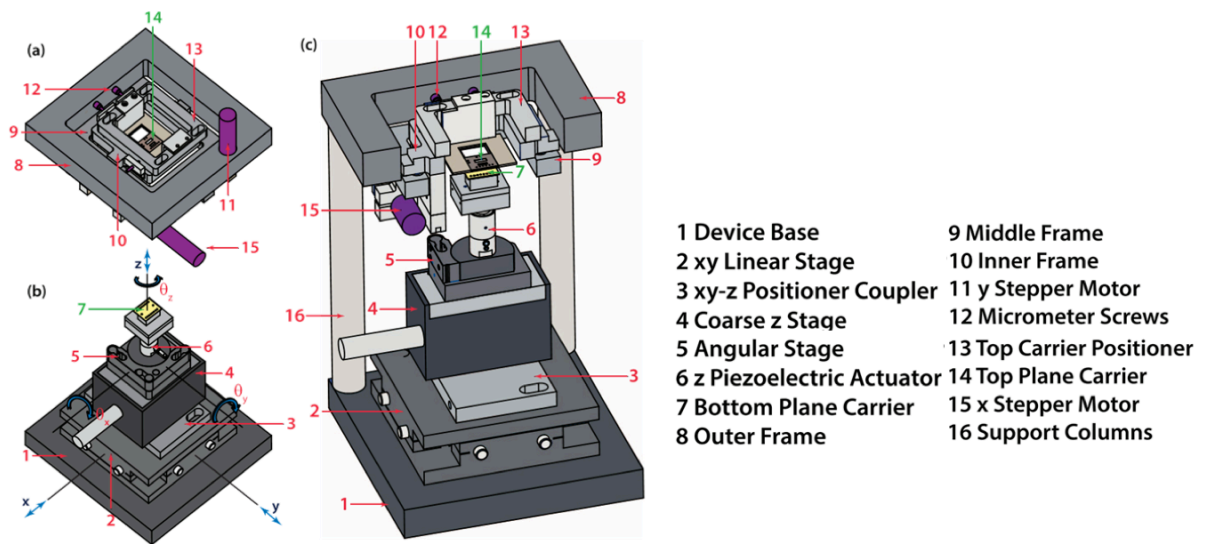


Figure 5-5- Nano-positioning stage with 6 degrees of freedom with required mechanical and thermal stability for parallelizing, placing in sub-wavelength distances and maintaining the surfaces throughout the entire length of experiment.

C. High-resolution calorimeter devices

Calorimeter devices used for studying NF-RHT require specific qualities unique to these experiments. In addition to cleanliness, flatness and roughness requirements, it is necessary to employ calorimeters with high heat flow resolution as well as to adopt designs with high mechanical stiffness.

While the high-resolution of the calorimeter device enables precise quantification of far-field heat transfer at large gap sizes, the mechanical stiffness of the device, enables us to decrease the minimum attainable gap between the two surfaces by decreasing the snap-in distance arising from residual electrostatic interactions. To address these requirements, I developed two new types of devices, which feature both high-resolution, exceptional stiffness ($> 10 \text{ N/m}$) with flatness of $< 20 \text{ nm}$ over a $50 \mu\text{m} \times 50 \mu\text{m}$ region (Figure 5-6).

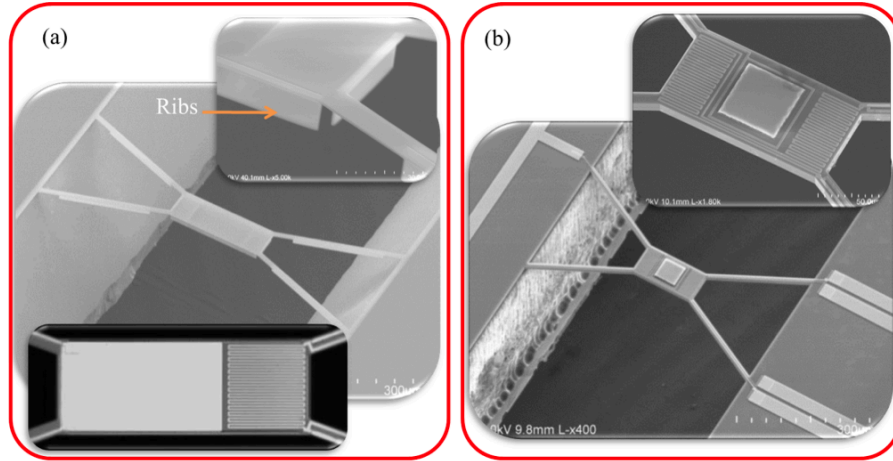


Figure 5-6- Two novel calorimeter devices developed for studying NFRHT in sphere-plane and plane-plane configurations. (a) Calorimeter device with rib structure on the active area and suspension beams; (b) Calorimeter devices based on Silicon On Insulator chips with ultimate stiffness required for studying various material structures.

We note that given the excellent stiffness of the top device, snap-in to the sphere due to electrostatic forces arising from residual charges does not happen until the separation between the sphere and the device is a few nanometers (<5 nm). Figure 5-7 and Figure 5-8 summarizes the fabrication process of both devices. We characterized these devices following the same procedures explained in chapters 2 and 4. Table 5-1 summarizes their performance specifications.

Table 5-1- Performance specifications of calorimeter devices developed for studying NFRHT.

<i>Measurement Conditions</i>	<i>Ribbed Device</i>	<i>SOI Device</i>
Thermal bandwidth	2 Hz	> 10 Hz
Thermal Conductance	$2 \mu\text{W/K}$	300 uW/K
Thermometry resolution	$20 \mu\text{K}$	$20 \mu\text{K}$
Calorimetry resolution	$< 40 \text{ pW}$	$< 6 \text{ nW}$
Flatness of the active area	$< 20 \text{ nm}$	$< 10 \text{ nm}$
Stiffness of the beam	10 N/m	$> 100 \text{ N/m}$

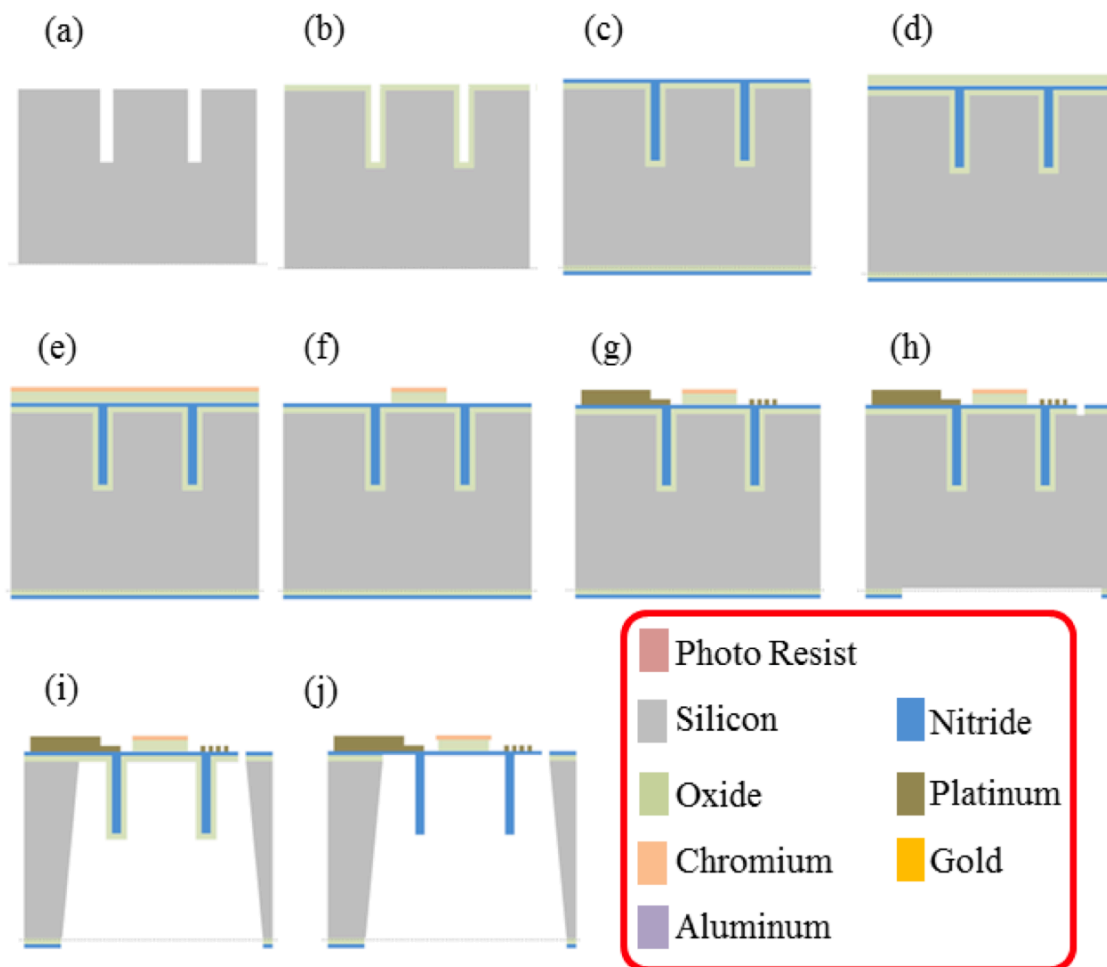


Figure 5-7- Fabrication process flow for calorimeter devices with rib structure. (a) starting with 500 μm silicon wafer 0.8 μm trenches with 10 μm depth are etched using RIE tool; (b) trench width is further reduced by thermal oxidizing of Si to grow 0.5 μm Oxide; (c) trenches are capped by depositing 0.6 μm low-stress nitride using LP-CVD furnace; (d) target active layer deposition-2 μm of low temperature oxide; (e) thermal evaporations of 100 nm Au film as the cap layer; (f) Au cap layer and oxide etch using plasma etch to form active area; (g) heater/thermometer and electrical connection patterns using lift-off process; (h) front and backside patterning of nitride film to form device contour; (i) wet release of the device using KOH etch; (j) removal of support oxide using BHF etch.

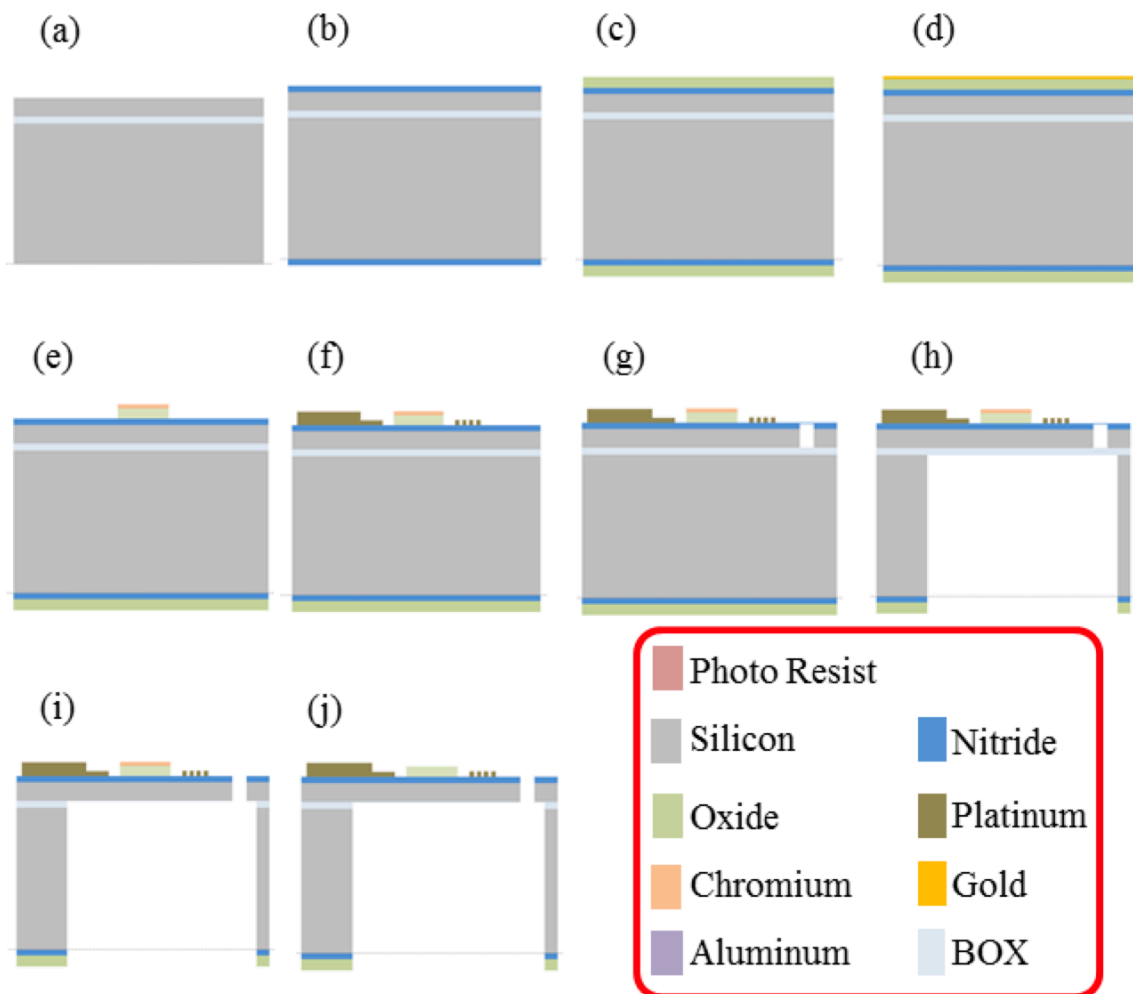


Figure 5-8- Fabrication process flow for calorimeter devices based on Silicon On Insulator (SOI) devices. (a) starting with 500 μm thick SOI wafer with 1 μm thick Buried Oxide (BOX) layer and 10 μm device layer; (b) 500 nm thick insulating nitride layer deposition as using LP-CVD tool; (c) target active layer deposition-2 μm of low temperature oxide; (d) thermal evaporations of 100 nm Au film as the cap layer; (e) Au cap layer and oxide etch using plasma etch to form active area; (f) heater/thermometer and electrical connection patterns using lift-off process; (g) front and backside patterning of nitride film to form device contour; (h) through-wafer etch using RIE tool and stopping on BOX layer; (i) removal of BOX using BHF etch; (j) removing cap layer using Au etchant.

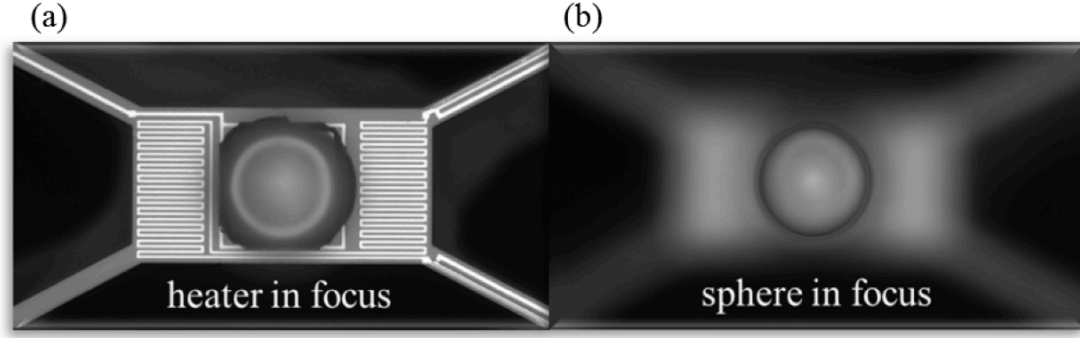


Figure 5-9- Optical images of the heating calorimeter with a 53 μm micro-sphere mounted on it. (a) image focused on the device surface; (b) image focused on the micro-sphere.

5-5- Experiments performed to understand the effect of film-thickness on NF-RHT

In order to systematically study effect of the film thickness on NFRHT, we used the experimental method described in section (5-4) and illustrated in Figure 5-4. The SiO_2 micro-sphere with diameter of 53 μm is glued using Crystalbond 509 onto the heating calorimeter, which enables us to modulate its temperature by passing a sinusoidal current through the heating coil integrated into the heating calorimeter.

Figure 5-9 shows the heating calorimeter with SiO_2 micro-sphere mounted on top of it. Then, we used the nano-positioner stage to parallelize the two macro-scale chips and bring them controllably in close proximity of each other. Subsequently, the temperature of the bottom heating calorimeter was modulated by $\Delta T_{H, 2\text{Hz}} = 10 \text{ K}$ at a frequency of 2 Hz, which resulted in radiative heat current ($Q_{\text{Rad}, 2\text{Hz}}$) from the micro-sphere to the receiver calorimeter. The temperature modulations in the receiver calorimeter ($\Delta T_{R, 2\text{Hz}}$) arising from this heat current was measured using the integrated resistance thermometer and were used to quantify the radiative heat transfer:

$$Q_{\text{Rad}, 2 \text{ Hz}}(\text{gap}) = G_{\text{Beams}} \times \Delta T_{R, 2 \text{ Hz}} \quad (5-5)$$

where G_{Beams} is the thermal conductance of the receiver calorimeter, respectively.

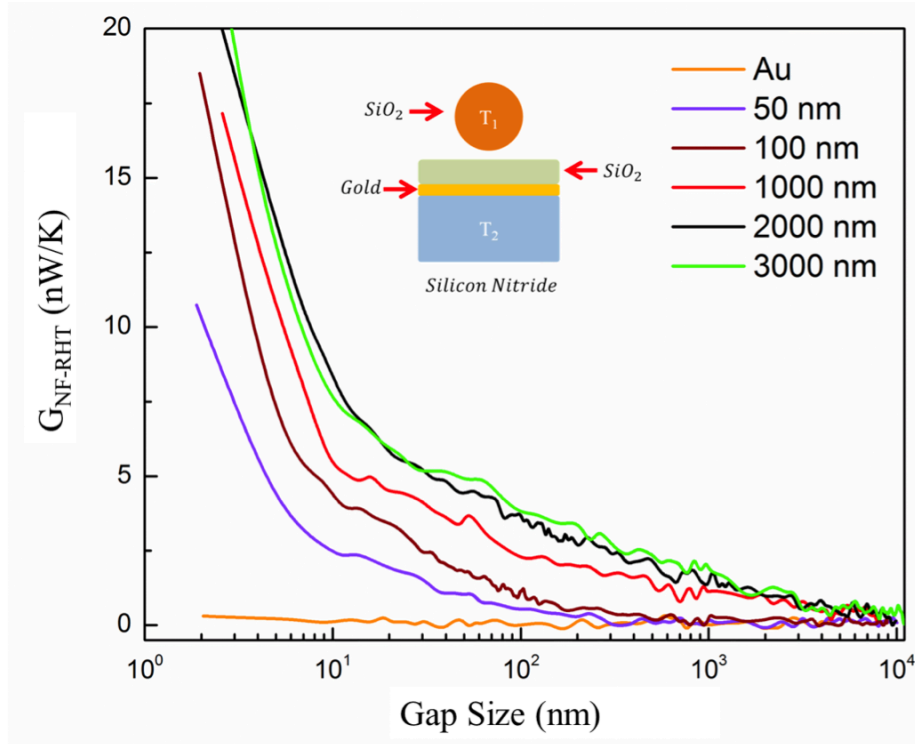


Figure 5-10- Measured near-field contribution to the radiative thermal conductance. The effect of far-field radiation and change in view factor has been subtracted out from the measured data. It can be seen that the thickness of the films dramatically influence the gap-size at which NF-RHT effects become appreciable.

The measured gap dependent heat current was used to estimate the thermal conductance of the gap $G(gap)$ as follows, by simultaneous measurement of amplitude of the temperature change on the heating calorimeter ($\Delta T_{H, 2Hz}$):

$$G(gap) = \frac{Q_{Rad, 2Hz}(gap)}{\Delta T_{H, 2Hz} - \Delta T_{R, 2Hz}} \quad (5-6)$$

Figure 5-10 shows the measured near-field thermal conductance (G_{NF-RHT}) vs. the distance between the emitter and receiver surfaces for different receiver film thicknesses of 50 and 100 nm and 1, 2 and 3 μm . Note that in obtaining G_{NF-RHT} , both the far-field contribution and small increases in the far-field contributions due to a change in the view factor have been subtracted out. This was done by measuring the far-field thermal conductance at large gap-sizes and by computing the effect of view factors from the known geometry of the problem.

As a control experiment we also studied NF-RHT between the silica sphere and a receiver calorimeter which had only a thin Au film and no SiO₂ layer. The obtained data, shown in Figure 5-10 shows no significant increase in thermal conductance as the gap decreases. This experiment shows that the measured enhancements are only present when the top devices are coated with an SiO₂ thin film suggesting that the surface-phonon polaritons on the SiO₂ surface may be responsible for the observed gap dependent behavior.

The results shown above for the 3 μm thick SiO₂ film feature an enhancement in conductance, which starts at distances as large as 3-4 μm . This is clearly in contrast with our observations on a 50 nm thick film where no significant enhancement was detected when the gap size is greater than a few hundred nanometers. Interestingly, we observe that when the gap size becomes comparable to film thickness the thermal conductance between the two surfaces begins to increase significantly. We also did experiments with 1 and 2 μm thick films and observed results, which are very similar to those seen in the 3 μm thick films except that the enhancements in conductance began at smaller gap sizes for the 1 μm thick film. Our results show a strong dependence of NF-RHT on both the coating thickness as well as the gap-size at which NF-RHT conductance becomes measurable. These results can be well explained within the formalism of fluctuational electrodynamics as is described in the next section.

5-6- Theoretical modeling

Ongoing computational modeling in collaboration with Professor Juan Carlos Cuevas's group [Universidad Autonoma de Madrid, Spain], has helped us in better understanding our experimental results. The modeling of NF-RHT between the SiO₂ sphere and SiO₂-coated substrate was performed in two steps. We first computed the heat flux between a semi-infinite SiO₂ surface and SiO₂ films of various thicknesses (50 nm -3 μm) deposited on a Au substrate, as shown in the inset of Figure 5-11a. Subsequently, we used the results of this

model along with the Derjagun approximation [76][77] to compute the thermal conductance between a sphere and Au surfaces coated with silicon oxide coatings of various thicknesses to compute the thermal conductance of the gap $G(gap)$. In this approach we compute the heat transfer between a sphere and planar surface by approximating the surface of the sphere as a series of steps and computing the heat transfer between corresponding parallel faces using the results computed for parallel surfaces.

We calculated NF-RHT between the SiO₂ sphere and SiO₂ coated surfaces within the framework of fluctuational electrodynamics, in combination with a scattering matrix formalism [78] which is well suited for describing the propagation of electromagnetic waves in multi-layer systems. Within this approach, the heat transfer is given by Equation 5-3, where the transmission function takes the following form:

$$T = T_{\parallel} + T_{\perp}, \text{ where } T_{\alpha=\parallel,\perp}(\omega, k_{\parallel}) = \begin{cases} \frac{(1-|r_{\alpha}^{21}|^2)(1-|R_{\alpha}|^2)}{|D_{\alpha}|^2}, & \text{if } k_{\parallel} < \omega/c \\ \frac{4\text{Im}\{r_{\alpha}^{21}\}\text{Im}\{R_{\alpha}\}e^{-2\text{Im}\{k_{\perp,2}\}d}}{|D_{\alpha}|^2}, & \text{if } k_{\parallel} > \omega/c \end{cases} \quad (5-7)$$

where

$$R_{\alpha} = \frac{r_{\alpha}^{23} + r_{\alpha}^{34} e^{2ik_{\perp,3}\tau}}{1 - r_{\alpha}^{34} r_{\alpha}^{32} e^{2ik_{\perp,3}\tau}} \quad (5-8)$$

and

$$D_{\alpha} = 1 - r_{\alpha}^{21} R_{\alpha} e^{2ik_{\perp,2}d}. \quad (5-9)$$

Here r_{\perp}^{ij} and r_{\parallel}^{ij} are Fresnel coefficients defined as:

$$r_{\perp}^{ij} = \frac{k_{\perp,i} - k_{\perp,j}}{k_{\perp,i} + k_{\perp,j}} \quad (5-10)$$

and

$$r_{\parallel}^{ij} = \frac{\varepsilon_j k_{\perp,i} / \varepsilon_i - k_{\perp,j}}{\varepsilon_j k_{\perp,i} / \varepsilon_i + k_{\perp,j}} \quad k_{\perp,i} = \sqrt{\varepsilon_i \omega^2 / c^2 - k_{\parallel}^2} \text{ with } \text{Im}\{k_{\perp,i}\} > 0. \quad (5-11)$$

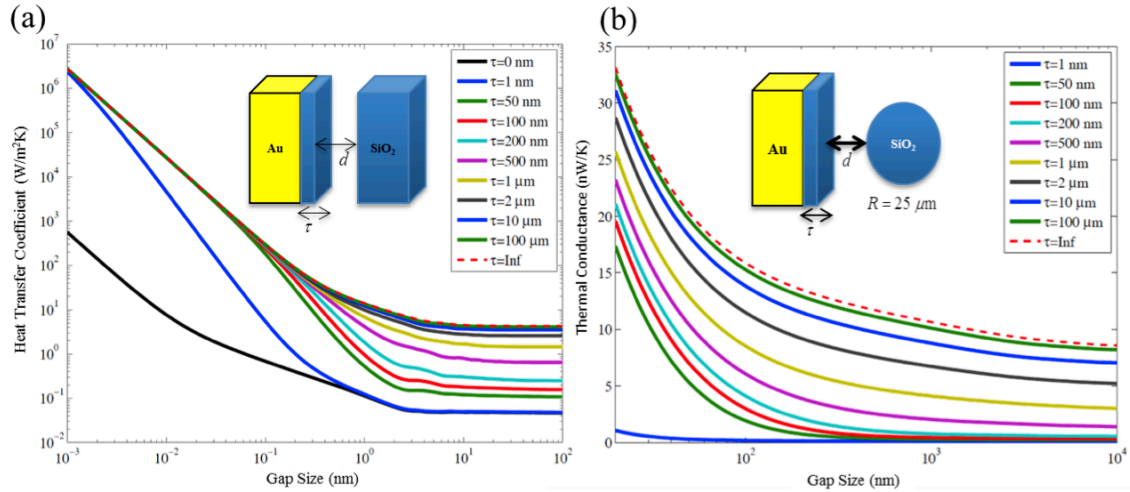


Figure 5-11- Results of the near-field heat transfer modeling within the framework of fluctuational electrodynamics and using scattering matrix formalism between SiO₂ sphere and Au surfaces coated with SiO₂ film with different thicknesses. (a) Heat transfer between semi-infinite SiO₂ surface and semi-infinite Au surface coated with SiO₂ film. (b) Transfer conductance between SiO₂ sphere and semi-infinite Au surface coated with SiO₂ film calculated using Derjagun approximation.

In the previous formulas, the superscript 1 corresponds to the semi-infinite SiO₂ surface, 2 to the air gap, 3 to the SiO₂ coating and 4 to the Au substrate. Using these expressions, we compute the heat transfer in this multi-layer system for various thicknesses of SiO₂ film (50 nm -3 μm) and the results are shown in Figure 5-11a.

Figure 5-11b shows the computed thermal conductance between a sphere with a diameter of 50 μm and Au surfaces coated with silicon oxide coatings of various thicknesses. As it can be seen in this figure, computational results agree reasonably well with our experimental observations.

In order to understand the physics behind the observed film-thickness dependence, we analyzed the penetration depth of the surface-phonon polaritons that contribute to heat transfer. The penetration depth or skin depth (δ_λ) of electromagnetic waves in a material is defined as the distance from the surface at which the intensity of the wave attenuates to 1/e of its value at the surface.

This distance is a measure of the length scale over which the wave is effectively absorbed. A material with a thickness that is five to ten times the penetration depth can be considered to be opaque. The penetration depth for a propagating wave is traditionally defined as [79]:

$$\delta_{\lambda, Propagating}(\omega) = \frac{\lambda_0}{4\pi\kappa(\omega)} \quad (5-12)$$

where λ_0 is the wavelength of the light in vacuum and $\kappa(\omega)$ is the extinction coefficient or the imaginary part of the complex refractive index ($n(\omega) + i\kappa(\omega)$). It can be seen from Equation (5-12), that the penetration depth depends on the frequency of the photon as well as the optical properties of the material at this frequency. The skin depth for an evanescent wave is defined as [63, 70]:

$$\delta_{\lambda, Evanescent} = \frac{1}{2\text{Im}(k_{\perp})}, \quad (5-13)$$

where k_{\perp} is the wave vector component perpendicular to the surface. In order to elucidate the gap dependence of the penetration depth in near-field, we computed the spectral contribution of different wavelengths to the NF-RHT in the multi-layer system for absorber films with two different thicknesses of 2 μm and 100 nm (Figure 5-12) at a gap size equal to 10 nm. Figure 5-12b, clearly illustrates the interesting fact that the energy transport is completely dominated two narrow frequency regions where the real part of the dielectric constant of SiO_2 is negative (Figure 5-12a). These are precisely the regions where the surface phonon-polaritons (SPP) which are transverse magnetic (TM) modes, can be excited.

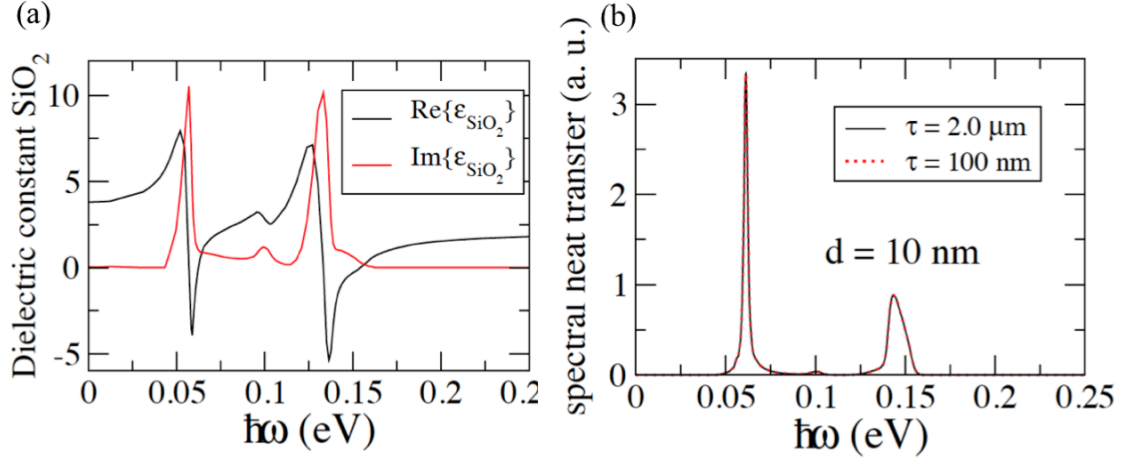


Figure 5-12- (a) Frequency dependent dielectric constant of SiO₂ film. (b) Computed spectral composition of the NF-RHT between bulk SiO₂ surface and bulk Au surface coated 2μm and 100 nm SiO₂ films separated by 10 nm.

This strongly suggests that these surface electromagnetic modes dominated the heat transfer for small gaps. In order to elucidate the gap dependence of the penetration depth in the near-field, we looked at the magnitude of the transmission function for TM waves (T_{\parallel}) at the frequency of the SPP as a function of the gap size. Figure 5-13 shows the value of the T_{\parallel} for the multi-layer system as a function of the product of k_{\parallel} (component of wave vector parallel to the surface) and d (gap size) for absorbing films with two different thicknesses of 2μm and 100 nm. It can be seen from the figure that upon decreasing the gap size the magnitude of the dominant contributing wave vector increases and becomes very large and is inversely proportional to d .

Therefore, for small gaps, where the relevant parallel wave vector satisfies $k_{\parallel} \gg \sqrt{\epsilon_j} \omega/c$, the resulting $k_{\perp} = ik_{\parallel}$ is an imaginary number with a large magnitude that is also inversely proportional to the gap size (d) as can be seen in Figure 5-13.

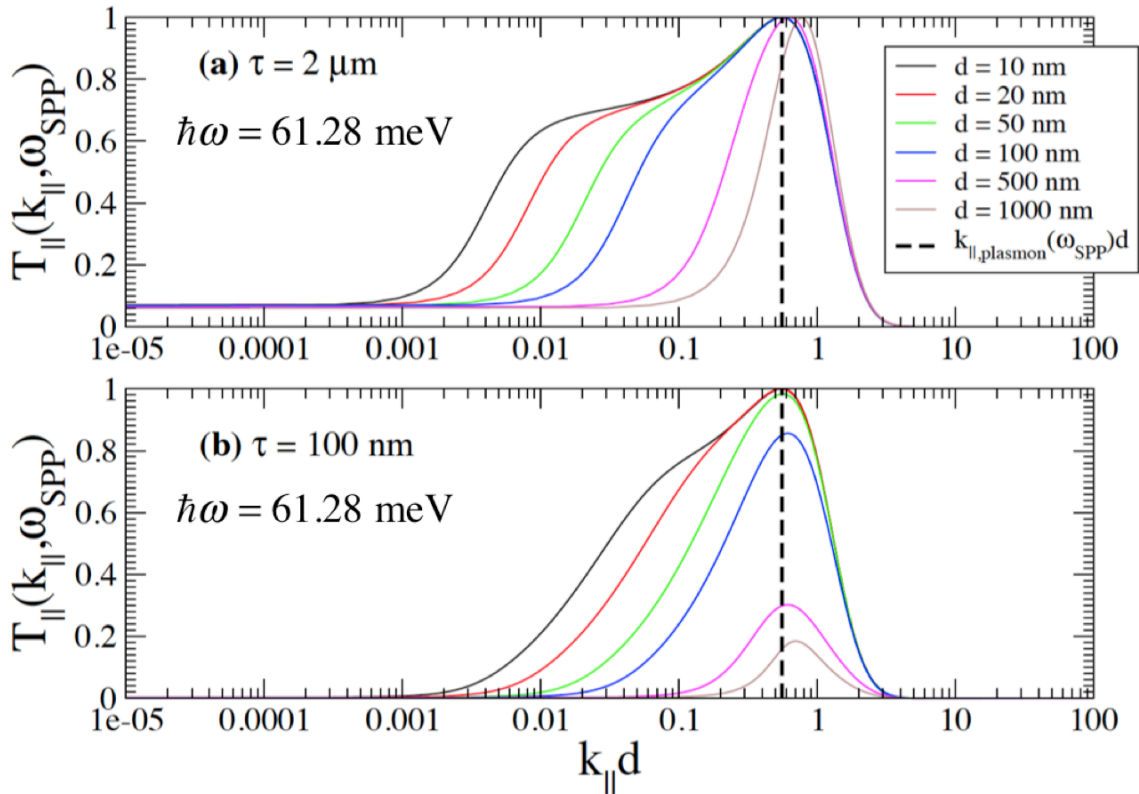


Figure 5-13- Magnitude of the transmission function ($T_{||}$) as a function of the product of $k_{||}$ and d for absorbing films with two different thicknesses of $2\mu\text{m}$ and 100 nm at different gap sizes computed at SPP frequency.

Hence, from Equation (5-13) it is apparent that the penetration depth is directly proportional to gap size (d). This analysis clearly shows that the observed film thickness dependence can be traced to the gap-dependent penetration depth of SPPs that dominate heat transfer in nanoscale gaps between SiO_2 films. This analysis is also in agreement with other theoretical works [63], which have predicted existence of a gap dependent penetration depth in NF-RHT.

To further illustrate this point, it is insightful to look at the magnitude of the square of electric field associated with SPP in the absorbing film. Figure 5-14, shows the results for the multi-layer system of this calculation for two film thicknesses of $2\mu\text{m}$ and 100 nm at different gap sizes of 10, 20, 50 and 100 nm. It can be seen that the penetration depth of SPP scales proportional to the gap size between the two surfaces and at small gaps majority of the

energy is absorbed at distances as small as the gap size. The insights gained from this work suggest that NF-RHT is completely dominated by the excitation of surface phonon polaritons, and in this regime the effective skin depth scales with gap size. Therefore, for small gaps, even a very thin film is optically opaque and very thin films with thickness comparable to the gap size are sufficient to get dramatic enhancements in NF-RHT.

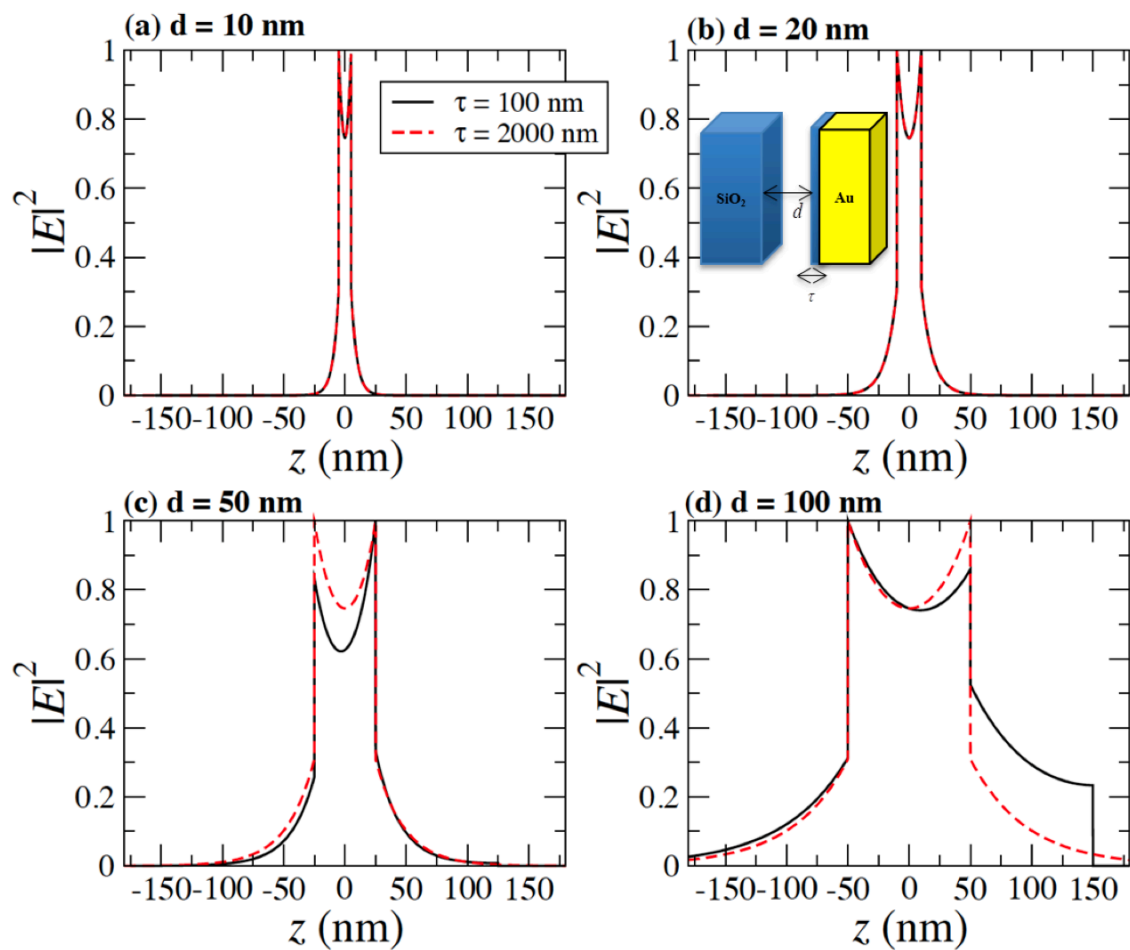


Figure 5-14- Magnitude square of electric field ($|E|^2$) at the excitation frequency of SPP for two different coating thicknesses and gap sizes of 10, 20, 50 and 100 nm. The Au layer is placed on the right side and results illustrate the gap-dependence of the penetration depth of SPPs.

5-7- Conclusion

In summary, here we presented the very first experimental demonstration of gap-size dependence of penetration depth in NF-RHT. The computational modeling of this phenomenon suggests that the major contribution to NF-RHT at each gap size stems from excitation of surface phonon-polaritons whose effective skin depth scales with the gap size. These findings highlight important thin-film effects that will be critical in designing future thermophotovoltaic devices [80-82], heat assisted magnetic recording devices and nanogap thermionic devices where NF-RHT effects will play an important role.

CHAPTER 6

Summary and Outlook

6-1- Summary

The work presented in this dissertation, has focused on developing novel metrology tools and techniques for quantification of energy transport at the micro- and nanoscale, and employing these tools to obtain insights into Near-Field Radiative Heat Transport (NF-RHT) phenomena. This work pioneered the development of the first picowatt resolution calorimeter capable of resolving single digit picowatt heat flows at room temperature [83]. This resolution was achieved by employing a novel calorimeter design, which featured excellent thermal isolation via suspension of its active area and employed a high-resolution bimaterial cantilever thermometer. While these calorimeter design successfully advanced the resolution over existing methods by more than an order of magnitude, its application is restricted to studies where the calorimeter can be mechanically decoupled from the environment and other instrumentations, such that the inherent thermo-mechanical cross-coupling of the bimaterial cantilever thermometer does not limit its performance. To overcome this shortcoming, I considered the possibility of finding an alternative thermometry method to the bimaterial cantilever thermometer. Towards this goal, I performed a detailed noise analysis on resistance thermometers. The results of this study [57] allowed me to devise novel thermometry schemes, which made it possible to perform thermometry measurements with a resolution comparable to that of a bimaterial cantilever thermometer when measuring modulated

temperature changes. Using the insights gained from this study, I developed an all-electrical calorimeter [84], which featured a very low thermal conductance via suspension of the active area and employed a high-resolution resistance thermometry technique.

Finally, I used these calorimeters to study NF-RHT. Specifically, we studied—for the first time—the effect of film thickness on the NF-RHT between two dielectric surfaces [Chapter 5]. We find that the resulting heat fluxes are similar to those between two bulk silicon dioxide surfaces when the gap size is reduced to be comparable to that of the film thickness. This interesting effect, which is expected to hold true for various dielectric surfaces where heat transport is dominated by surface phonon-polaritons has important implications for near-field based thermo photovoltaic devices.

6-2- Possible future directions

The advancements in picowatt resolution heat flow calorimetry, described in this work, pave the way towards development of calorimeters with even better heat flow calorimetry resolutions. However, the logical question that needs to be answered is: What is the fundamental limit to the resolution of a calorimeter device? Our initial promising studies indicate that there is still room for improving the resolution of calorimeter devices at room temperature and further pursue of this subject seems a fruitful direction.

Further, the novel experimental platforms developed in this work for studying NF-RHT can be extended to study NF-RHT phenomena in the *plane-plane configuration* and in *sub-micron gap sizes* for the first time. This is possible due to two technical capabilities developed in our group: 1) Our novel six degree of freedom nano-positioning platform, which is capable of parallelizing, positioning and maintain planar surface in sub-micron separations and with nanometer resolutions[75] and 2) the new calorimeter devices, which are specifically designed for studying radiative energy transport in the near-field regime [Chapter 5]. These capabilities, which enable transport phenomenon between planar surfaces and in

sub-micron separations—for the first time—have enormous potential for studying a wide range of interesting and important scientific and technological problems, which include novel thermal to electrical energy conversion devices and studying near-field based thermal management systems.

Appendix

To justify the use of Equations (3-13) and (3-23), we first define the voltage noise associated with temperature drift is given by:

$$V_{\text{temperature drift}}(t) = V(t) = (I_S R \alpha) \sin(2\pi f_S t) \cdot \Delta T(t), \quad (\text{A1})$$

which can be represented as the sum of the two signals:

$$V(t) = \underbrace{\left(\frac{I_S R \alpha}{2i}\right) e^{i2\pi f_S t} \cdot \Delta T(t)}_{y_1(t)} + \underbrace{\left(-\frac{I_S R \alpha}{2i}\right) e^{-i2\pi f_S t} \cdot \Delta T(t)}_{y_2(t)}. \quad (\text{A2})$$

The power spectral density of $V(t)$, $PSD_V(f)$ can be related to the autocorrelation function of $V(t)$. The autocorrelation function $R_{VV}(\tau)$ is given by:

$$R_{VV}(\tau) = \langle V^*(t) V(t + \tau) \rangle = \lim_{T \rightarrow \infty} \frac{1}{T} \int_{-\infty}^{+\infty} V^*(t) V(t + \tau) dt, \quad (\text{A3})$$

and is related to the one-sided power spectral density by:

$$PSD_V(f) = G_V(f) = \int_0^{+\infty} 2R_{VV}(\tau) e^{-i2\pi f \tau} d\tau. \quad (\text{A4})$$

From equation A2

$$R_{VV}(\tau) = \langle [y_1^*(t) + y_2^*(t)] \times [y_1(t + \tau) + y_2(t + \tau)] \rangle, \quad (\text{A5})$$

this implies that

$$R_{VV}(\tau) = R_{y_1 y_1}(\tau) + R_{y_2 y_2}(\tau) + R_{y_1 y_2}(\tau) + R_{y_2 y_1}(\tau), \quad (\text{A6})$$

where $R_{y_1 y_2}(\tau)$ and $R_{y_2 y_1}(\tau)$ are the cross-correlation functions between $y_1(t)$ and $y_2(t)$.

Using equations A2, A3, A4 and A6 it can be show that:

$$G_V(f) = \frac{(I_s R \alpha)^2}{4} \left[G_{\Delta T}(f - f_s) + G_{\Delta T}(f + f_s) - \lim_{T \rightarrow \infty} \frac{2}{T} [\Delta T^*(f - f_s) \Delta T(f + f_s)] + \Delta T^*(f + f_s) \Delta T(f - f_s) \right], \quad (\text{A7})$$

where $G_{\Delta T} = PSD_{\Delta T, \text{Drift}}$ is the power spectral density of temperature drift as defined in section (3-3) and $\Delta T(f)$ represents the Fourier components of the temperature drift signal. When $(f - f_s) \rightarrow 0$, $PSD_{\Delta T, \text{Drift}}(f - f_s)$ dominates over all other terms suggesting that when $f \rightarrow f_s$:

$$PSD_V(f) = G_V(f) \sim \frac{(I_s R \alpha)^2}{2} PSD_{\Delta T, \text{Drift}}(f - f_s) \quad (\text{A8})$$

which can be used to obtain Eq. (13) of the manuscript. Similarly, Eq. (23) of the manuscript can also be obtained using Eq. (A7) and the approximations described above.

References

1. James, A., *Thermal and energetic studies of cellular biological systems*. 1987, Bristol, UK: Wright.
2. Kleiber, M., *The fire of life; an introduction to animal energetics*. 1961, New York: Wiley. 454 p.
3. Richards, P.L., *Bolometers for infrared and millimeter waves*. Journal of Applied Physics, 1994. **76**(1): p. 1-24.
4. Siringo, G., et al., *The Large APEX BOLometer CAmera LABOCA*. A&A, 2009. **497**(3): p. 945-962.
5. Keskin, S. and T. Akin. *The first fabricated dual-band uncooled infrared microbolometer detector with a tunable micro-mirror structure*. 2012.
6. Cahill, D.G., et al., *Nanoscale thermal transport*. Journal of Applied Physics, 2003. **93**(2): p. 793-818.
7. Lee, W., et al., *High-sensitivity microfluidic calorimeters for biological and chemical applications*. Proceedings of the National Academy of Sciences, 2009.
8. Xuming, Z., et al., *Plasmonic photocatalysis*. Reports on Progress in Physics, 2013. **76**(4): p. 046401.
9. Gust, D., T.A. Moore, and A.L. Moore, *Molecular mimicry of photosynthetic energy and electron transfer*. Accounts of Chemical Research, 1993. **26**(4): p. 198-205.
10. Barnes, J.R., et al., *Photothermal Spectroscopy with Femtojoule Sensitivity Using a Micromechanical Device*. Nature, 1994. **372**(6501): p. 79-81.
11. Coppens, Z.J., et al., *Probing and Controlling Photothermal Heat Generation in Plasmonic Nanostructures*. Nano Letters, 2013. **13**(3): p. 1023-1028.
12. Baffou, G. and R. Quidant, *Thermo-plasmonics: using metallic nanostructures as nano-sources of heat*. Laser & Photonics Reviews, 2013. **7**(2): p. 171-187.
13. Schwab, K., et al., *Measurement of the quantum of thermal conductance*. Nature, 2000. **404**(6781): p. 974-977.
14. Shen, S., et al., *Polyethylene nanofibres with very high thermal conductivities*. Nature Nanotechnology, 2010. **5**(4): p. 251-255.
15. Shi, L., et al., *Measuring Thermal and Thermoelectric Properties of One-Dimensional Nanostructures Using a Microfabricated Device*. J. H. Trans., 2003. **125**(5): p. 881.
16. Zink, B.L., R. Pietri, and F. Hellman, *Thermal conductivity and specific heat of thin-film amorphous silicon*. Physical Review Letters, 2006. **96**(5): p. 055902.
17. Varesi, J., et al., *Photothermal measurements at picowatt resolution using uncooled micro-optomechanical sensors*. Applied Physics Letters, 1997. **71**(3): p. 306-308.
18. Shen, S., A. Narayanaswamy, and G. Chen, *Surface Phonon Polaritons Mediated Energy Transfer between Nanoscale Gaps*. Nano Letters, 2009. **9**(8): p. 2909-2913.
19. Seol, J.H., et al., *Two-Dimensional Phonon Transport in Supported Graphene*. Science, 2010. **328**(5975): p. 213-216.
20. Yang, J.K., et al., *Enhanced and switchable nanoscale thermal conduction due to van der Waals interfaces*. Nature Nanotechnology, 2012. **7**(2): p. 91-95.

21. Liu, S., et al., *Anomalous heat conduction and anomalous diffusion in low dimensional nanoscale systems*. The European Physical Journal B, 2012. **85**(10): p. 1-20.
22. Li, N.B., et al., *Colloquium: Phononics: Manipulating heat flow with electronic analogs and beyond*. Reviews of Modern Physics, 2012. **84**(3): p. 1045-1066.
23. Lai, J., et al., *Optimization and performance of high-resolution micro-optomechanical thermal sensors*. Sensors and Actuators A: Physical, 1997. **58**(2): p. 113-119.
24. Shi, L., et al., *Measuring thermal and thermoelectric properties of one-dimensional nanostructures using a microfabricated device (vol 125, pg 881, 2003)*. Journal of Heat Transfer-Transactions of the ASME, 2003. **125**(6): p. 1209-1209.
25. von Arx, M., O. Paul, and H. Baltes, *Process-dependent thin-film thermal conductivities for thermal CMOS MEMS*. Microelectromechanical Systems, Journal of, 2000. **9**(1): p. 136-145.
26. Bourgoïn, J., G. Allogho, and A. Hache, *Thermal conduction in thin films measured by optical surface thermal lensing*. Journal of Applied Physics, 2010. **108**(7): p. 073520-6.
27. Wingert, M.C., et al., *Thermal Conductivity of Ge and Ge-Si Core-Shell Nanowires in the Phonon Confinement Regime*. Nano Letters, 2011. **11**(12): p. 5507-5513.
28. Sadat, S., et al., *Room temperature picowatt-resolution calorimetry*. Applied Physics Letters, 2011. **99**(4).
29. Bourgeois, O., et al., *Attojoule calorimetry of mesoscopic superconducting loops*. Physical Review Letters, 2005. **94**(5).
30. Fon, W.C., et al., *Nanoscale, phonon-coupled calorimetry with sub-attojoule/Kelvin resolution*. Nano Letters, 2005. **5**(10): p. 1968-1971.
31. Lopeandia, A.F., et al., *Sensitive power compensated scanning calorimeter for analysis of phase transformations in small samples*. Review of Scientific Instruments, 2005. **76**(6).
32. Zink, B.L., R. Pietri, and F. Hellman, *Thermal conductivity and specific heat of thin-film amorphous silicon*. Physical Review Letters, 2006. **96**(5).
33. Kim, K., et al., *Ultra-High Vacuum Scanning Thermal Microscopy for Nanometer Resolution Quantitative Thermometry*. ACS Nano, 2012. **6**(5): p. 4248-4257.
34. Shi, L., et al., *Scanning thermal microscopy of carbon nanotubes using batch-fabricated probes*. Applied Physics Letters, 2000. **77**(26): p. 4295-4297.
35. Wingert, M.C., et al., *Ultra-sensitive thermal conductance measurement of one-dimensional nanostructures enhanced by differential bridge*. Review of Scientific Instruments, 2012. **83**(2).
36. Sikora, A., et al., *Highly sensitive thermal conductivity measurements of suspended membranes (SiN and diamond) using a 3 omega-Volklein method*. Review of Scientific Instruments, 2012. **83**(5).
37. Mangum, B.W., *STABILITY OF SMALL INDUSTRIAL PLATINUM RESISTANCE THERMOMETERS*. Journal of Research of the National Bureau of Standards (United States), 1984. **89**(4): p. 305-316.
38. Childs, P.R.N., *Advances in temperature measurement*, in *Advances in Heat Transfer*, T.F.I.Y.I.C. James P. Hartnett and A.G. George, Editors. 2003, Elsevier. p. 111-181.
39. Childs, P.R.N., J.R. Greenwood, and C.A. Long, *Review of temperature measurement*. Review of Scientific Instruments, 2000. **71**(8): p. 2959-2978.
40. Ziman, J.M., *Electrons and Phonons : The theory of Transport Phenomena in Solids*. Oxford classic texts in the physical sciences. 2001, New York: Oxford University Press. xiv, 554 p.

41. Heer, C.V., *Statistical mechanics, kinetic theory, and stochastic processes*. 1972, New York,: Academic Press. xvi, 602 p.
42. Razavi, B., *Design of Analog CMOS Integrated Circuits*. 2001, Boston, MA: McGraw-Hill. xx, 684 p.
43. Papoulis, A. and S.U. Pillai, *Probability, random variables, and stochastic processes*. 4th ed. 2002, Boston: McGraw-Hill. x, 852 p.
44. Carslaw, H.S. and J.C. Jaeger, *Conduction of Heat in Solids*. 2nd ed. 1986, New York: Oxford University Press. viii, 510 p.
45. Ott, H.W., *Noise reduction techniques in electronic systems*. 2nd ed. 1988, New York: Wiley. xx, 426 p.
46. Horowitz, P. and W. Hill, *The Art of Electronics*. 2nd ed. 1989, Cambridge England ; New York: Cambridge University Press. xxiii, 1125 p.
47. Wingert, M.C., et al., *Thermal conductivity of ge and ge-si core-shell nanowires in the phonon confinement regime*. *Nano Lett*, 2011. **11**(12): p. 5507-13.
48. Wingert, M.C., et al., *Ultra-sensitive thermal conductance measurement of one-dimensional nanostructures enhanced by differential bridge*. *Review of Scientific Instruments*, 2012. **83**(2): p. 024901.
49. Barnes, J.R., et al., *A femtojoule calorimeter using micromechanical sensors*. *Review of Scientific Instruments*, 1994. **65**(12): p. 3793.
50. Sadat, S., et al., *Room temperature picowatt-resolution calorimetry*. *Applied Physics Letters*, 2011. **99**(4): p. 043106.
51. Canetta, C. and A. Narayanaswamy, *Sub-picowatt resolution calorimetry with a bi-material microcantilever sensor*. *Applied Physics Letters*, 2013. **102**(10): p. 103112-4.
52. Lepri, S., R. Livi, and A. Politi, *Thermal conduction in classical low-dimensional lattices*. *Physics Reports-Review Section of Physics Letters*, 2003. **377**(1): p. 1-80.
53. Basu, S., Z. Zhang, and C. Fu, *Review of near-field thermal radiation and its application to energy conversion*. *International Journal of Energy Research*, 2009. **33**(13): p. 1203-1232.
54. Carslaw, H.S. and J.C. Jaeger, *Conduction of Heat in Solids*. 2nd ed. 1986, New York: Oxford University Press.
55. Zhang, X., et al., *Thermal and Electrical Properties of a Suspended Nanoscale Thin Film*. *International Journal of Thermophysics*, 2007. **28**(1): p. 33-43.
56. Incropera, F.P., *Fundamentals of heat and mass transfer*. 6th ed. 2007, Hoboken, NJ: John Wiley.
57. Sadat, S., E. Meyhofer, and P. Reddy, *High resolution resistive thermometry for micro/nanoscale measurements*. *Review of Scientific Instruments*, 2012. **83**(8).
58. Cahill, D.G., *Thermal-Conductivity Measurement from 30-K to 750-K - the 3-Omega Method*. *Review of Scientific Instruments*, 1990. **61**(2): p. 802-808.
59. information., S.s.m.a.f.
60. Planck, M., *The theory of heat radiation*. *Vorlesungen über die Theorie der Wärmestrahlung*. English. 1959, New York: Dover Publications. 224 p.
61. Polder, D. and M.A.V. Hove, *Theory of Radiative Heat Transfer between Closely Spaced Bodies*. *Physical Review B*, 1971. **4**(10): p. 3303-&.
62. Joulain, K., et al., *Surface electromagnetic waves thermally excited: Radiative heat transfer, coherence properties and Casimir forces revisited in the near field*. *Surface Science Reports*, 2005. **57**(3-4): p. 59-112.
63. Basu, S. and Z. Zhang, *Ultrasmall penetration depth in nanoscale thermal radiation*. *Applied Physics Letters*, 2009. **95**(13).

64. Muller-Hirsch, W., et al., *Heat transfer in ultrahigh vacuum scanning thermal microscopy*. Journal of Vacuum Science & Technology A: Vacuum, Surfaces, and Films, 1999. **17**(4): p. 1205-1210.
65. Wischnath, U.F., et al., *The near-field scanning thermal microscope*. Review of Scientific Instruments, 2008. **79**(7): p. -.
66. Kittel, A., et al., *Near-field thermal imaging of nanostructured surfaces*. Applied Physics Letters, 2008. **93**(19): p. -.
67. Rousseau, E., et al., *Radiative heat transfer at the nanoscale*. Nature Photonics, 2009. **3**(9): p. 514-517.
68. Kralik, T., et al., *Cryogenic apparatus for study of near-field heat transfer*. Review of Scientific Instruments, 2011. **82**(5): p. -.
69. Hargreaves, C.M., *Anomalous radiative transfer between closely-spaced bodies*. Physics Letters A, 1969. **30**(9): p. 491-492.
70. Park, K., et al., *Performance analysis of near-field thermophotovoltaic devices considering absorption distribution*. Journal of Quantitative Spectroscopy & Radiative Transfer, 2008. **109**(2): p. 305-316.
71. Volokitin, A.I. and B.N.J. Persson, *Near-field radiative heat transfer and noncontact friction*. Reviews of Modern Physics, 2007. **79**(4): p. 1291-1329.
72. Zhang, Z., *Nano/microscale heat transfer*. 2007, New York, NY: McGraw-Hill. xxi, 479 p.
73. Rytov, S.M., I.U.A. Kravtsov, and V.I. Tatarskiĭ, *Principles of statistical radiophysics. I: elements of random process theory*. Vvedenie v statisticheskuĭ radiofiziku.I.English. 1987, Berlin ; New York: Springer-Verlag. v.
74. Landau, L.D. and E.M. Lifshits, *Statistical physics*. Statisticheskaĭa fizika.English. 1969, Oxford, New York: Pergamon Press. xii, 484 p.
75. Ganjeh, Y., et al., *A platform to parallelize planar surfaces and control their spatial separation with nanometer resolution*. Review of Scientific Instruments, 2012. **83**(10): p. 9.
76. B. V. Derjaguin and I. I. Abrikosova, Sov. Phys. JETP **3**, 819 (1957).
77. Israelachvili, J.N., *Intermolecular and surface forces*. 2011, Burlington, MA: Academic Press. xxx, 674 p.
78. Whittaker, D.M. and I.S. Culshaw, *Scattering-matrix treatment of patterned multilayer photonic structures*. Physical Review B, 1999. **60**(4): p. 2610-2618.
79. Bhatia, M.B.E.W.A.B., *Principles of Optics, Seventh Edition*. 1999, [S.l.]: Cambridge University Press.
80. Narayanaswamy, A. and G. Chen, *Surface modes for near field thermophotovoltaics*. Applied Physics Letters, 2003. **82**(20): p. 3544-3546.
81. Laroche, M., R. Carminati, and J.-J. Greffet, *Near-field thermophotovoltaic energy conversion*. Journal of Applied Physics, 2006. **100**(6).
82. Francoeur, M., R. Vaillon, and M.P. Mengüç, *Thermal Impacts on the Performance of Nanoscale-Gap Thermophotovoltaic Power Generators*. Ieee Transactions on Energy Conversion, 2011. **26**(2): p. 686-698.
83. Sadat, S., et al., *Room temperature picowatt-resolution calorimetry*. Applied Physics Letters, 2011. **99**(4).
84. Sadat, S., E. Meyhofer, and P. Reddy, *Resistance thermometry-based picowatt-resolution heat-flow calorimeter*. Applied Physics Letters, 2013. **102**(16): p. 5.